

Spectroscopic Characterization and Oxidation on Catalytic Surfaces of Amino Acids Present in Viral Proteins

By

Saabiq Sharief Mohammad

Submitted to the Graduate Degree Program in the Department of Chemical and
Petroleum Engineering and the Graduate Faculty of the University of Kansas in
partial fulfillment of the requirements for the degree of Master of Science

Dr. Juan J. Bravo Suárez

Dr. Mark B. Shiflett

Dr. Kevin C. Leonard

Date Defended: May 11, 2022

The thesis committee for Saabiq Sharief Mohammad certifies that this is the approved version of
the following thesis:

Spectroscopic Characterization and Oxidation on Catalytic Surfaces of Amino Acids Present in Viral Proteins

Dr. Juan J. Bravo Suárez

Date Approved: July 29, 2022

Abstract

The outbreak of COVID-19 and its widespread transmission across the world has reasserted the need for understanding viruses and, consequently, the interactions of large biomolecules and ways to characterize them. This work studies the interactions of amino acids present in virus proteins with surfaces from a catalysis point of view. A review of inventions and patents in the field shows the use of metal and metal oxide catalysts in deactivating viruses; however, the mechanism of this process and tools to characterize biomolecules chemistry changes on surfaces are lacking. Towards the goal of devising an effective and simple method to achieve and monitor biomolecules chemical changes on catalytic surfaces, in situ FTIR combined with 2D-COS and online MS was employed to study the temperature programmed oxidation (TPO) of structurally related amino acids on α -alumina (α -Al₂O₃) and α -Al₂O₃ supported silver catalyst (Ag/ α -Al₂O₃) surfaces. The samples were analyzed by TGA to study their decomposition temperature profiles and to ascertain kinetic parameters such as apparent activation energies. Bond dissociation energy values of the amino acids along with 2D-COS and gas product formation as monitored by online MS during TPO were studied to determine possible reaction pathways and products. The amino acids were shown to oxidize more effectively on Ag(30%)/ α -Al₂O₃ catalyst, with reactions occurring at lower temperatures than those observed on α -Al₂O₃ and with primarily formation of CO_x, H₂O, and NH₃ in the gas phase. TGA kinetic studies showed a reduction of activation energy on the catalyst for all studied amino acids, suggesting catalytic activity on silver, but thermal decomposition on α -Al₂O₃. FTIR/2D-COS/MS provided a quick, qualitative means of tracking and understanding changes in real time and determining functional group reactivity. These results provide the basis for in situ and real time characterization of larger biomolecules and encourage future studies on the use of metal and metal oxide surfaces for virus deactivation.

Acknowledgements

I would like to express my profound gratitude to Dr. Juan J. Bravo-Suárez, whose constant encouragement, advice and support helped me immensely throughout my research and were instrumental in my growth.

I am extremely grateful to Dr. Mark B. Shiflett and Dr. Kevin C. Leonard for being on my thesis committee; their insightful advice was essential for improving my thesis and helped me gain further knowledge in the field.

I would like to extend my gratitude to Dr. Prajna Dhar and Ms. Martha Kehr for their immense help throughout my time here.

I would like to thank my friends and colleagues at the CEBC for their continuous friendship and support. I would like to convey my thanks to Hashim Alzahrani, Bhagysha Patil, Samir Castilla-Acevedo and Anoop Uchagawkar for their continuous advice and support throughout my research; I would like to acknowledge their immense help in the lab, from catalyst synthesis to instrument training, and for sharing their knowledge with me. I would also like to thank Melvin Santoso and Edy Bareda for all their help with Covid-19, viruses and more.

I would also like to thank my parents and my brother, without whose love and encouragement I would not be here today.

Finally, I would like to acknowledge the University of Kansas for all their help and support.

Table of Contents

Abstract.....	iii
Acknowledgements.....	iv
Table of Contents.....	v
List of Schemes.....	viii
List of Figures.....	ix
List of Tables.....	xii
Chapter 1. Introduction and Review	1
1.1.COVID-19 and Possible Methods of Virus Deactivation.....	1
1.2. Patents Review	3
1.3. News Releases and Developments Review.....	6
1.4. Hypothesis.....	9
1.5. Characterization	14
1.5.1. Thermogravimetric Analysis (TGA).....	15
1.5.2. Fourier Transform Infrared Spectroscopy (FTIR)	16
1.5.3. Two-Dimensional Correlation Spectroscopy (2D-COS).....	17
1.6. References	21

Chapter 2. Experimental	38
2.1. Introduction.....	38
2.2. Preparation	38
2.2.1. Catalyst Preparation.....	38
2.2.2. Amino Acid Samples Preparation	40
2.3. Characterization	41
2.3.1. Thermogravimetric Analysis (TGA).....	41
2.3.2. Ex Situ Fourier Transform Infrared Spectroscopy (FTIR)	42
2.4. In Situ FTIR Spectroscopy Experiment.....	42
2.5. References.....	44
Chapter 3. Thermogravimetric Analysis and Kinetic Study of Amino Acids on α -Alumina and α -Alumina supported Silver Catalyst in Oxygen Atmosphere.....	46
3.1. Introduction	46
3.2. Kinetic Theory.....	46
3.3. Methods.....	47
3.4. Results and Discussion.....	48
3.4.1. TGA.....	48
3.5. References	59
Chapter 4. In situ DRIFTS During TPO of Amino Acids on α -Alumina and α -Alumina supported Silver Catalyst Analyzed by 2D-COS and MS	63

4.1. Introduction	63
4.2. Bond Dissociation Energies	64
4.3. Results and Discussion.....	68
4.4. References	75
Chapter 5. Conclusions and Future Work	78
Appendices	81
1. Preliminary Calculations for Catalysts Preparation.....	81
2. Amino Acid Sample Preparation Calculations	83
3. Amino Acid IR Peak Assignments.....	84
4. Amino Acid Mass Spectrometry	86
5. TGA Results	87
6. TPO 2D-COS, Time Domain in Situ FTIR, and MS Results	96
7. Example for How to Analyze 2D-COS Spectra.....	108
8. References	110

List of Schemes

Scheme 1.1. Possible route and mechanism of virus deactivation.....	13
Scheme 1.2. Simplified mechanism of amino acid decomposition in oxygen atmosphere and on a catalyst surface.....	13
Scheme 1.3. General scheme for obtaining 2D Correlation spectra.....	18
Scheme 4.1. Amino alkyl radical formation in presence of Ag catalyst	75

List of Figures

Figure 1.1. Coronavirus structure.....	2
Figure 1.2. Schematics of COVID-19 transmission.....	2
Figure 1.3. Coronavirus spike protein showing long chains of cross-linked aminoacids.....	10
Figure 1.4. Spike protein aminoacid sequence.....	10
Figure 1.5. Layout of a typical Thermogravimetric Analysis (TGA) setup.....	15
Figure 1.6. Schematic representation of a Michelson interferometer	17
Figure 1.7. Example of 2D COS synchronous spectra (top) and asynchronous plots (bottom)...	19
Figure 1.8. Examples of synchronous and asynchronous 2D-COS plots.....	20
Figure 2.1. In situ FTIR experiment setup (MFC: Mass Flow Controller, 6WV: 6 Way Valve, IR: Infrared radiation).....	42
Figure 3.1. Results for Glycine/Al ₂ O ₃ TGA (top-left) and DTG (top-right), structure (middle), and Glycine/Ag/Al ₂ O ₃ TGA (bottom-left) and DTG (bottom-right).....	49
Figure 3.2. Results for Alanine/Al ₂ O ₃ TGA (top-left) and DTG (top-right), structure (middle), and Alanine/Ag/Al ₂ O ₃ TGA (bottom-left) and DTG (bottom-right).....	50
Figure 3.3. Results for Valine/Al ₂ O ₃ TGA (top-left) and DTG (top-right), structure (middle), and Valine/Ag/Al ₂ O ₃ TGA (bottom-left) and DTG (bottom-right).....	51
Figure 3.4. Results for Leucine/Al ₂ O ₃ TGA (top-left) and DTG (top-right), structure (middle), and Leucine/Ag/Al ₂ O ₃ TGA (bottom-left) and DTG (bottom-right).....	52
Figure 3.5. TGA kinetic analysis for Glycine/Al ₂ O ₃ (top) and Glycine/Ag/Al ₂ O ₃ (bottom): FWO method.....	55
Figure 3.6. TGA kinetic analysis for Glycine/Al ₂ O ₃ (top) and Glycine/Ag/Al ₂ O ₃ (bottom): FWO method	56
Figure 4.1. Glycine/Al ₂ O ₃ synchronous (top-left) and asynchronous 2D-COS plots (top-right) and time domain in situ FTIR spectra at different temperatures (bottom) during TPO.....	69
Figure 4.2. Glycine/Al ₂ O ₃ oxidation products from MS corresponding fragments for NH ₃ , H ₂ O, CO ₂ (left); NO, NO ₂ , CO, HCN (right) ⁶⁻¹² Uncalibrated MS traces were displaced vertically to facilitate reading.....	69

Figure 4.3. Glycine/Ag/Al ₂ O ₃ synchronous (top-left) and asynchronous 2D-COS plots (top-right) and time domain in situ FTIR spectra at different temperatures (bottom) during TPO.....	72
Figure 4.4. Glycine/Ag/Al ₂ O ₃ oxidation products from MS corresponding fragments for NH ₃ , H ₂ O, HCN, CO, CO ₂ (left); NO, NO ₂ (right) ⁶⁻¹² Uncalibrated MS traces were displaced vertically to facilitate reading.....	73
Figure A1. TGA kinetic analysis for Alanine/Al ₂ O ₃ (top) and Alanine/Ag/Al ₂ O ₃ (bottom): FWO method.....	87
Figure A2. TGA kinetic analysis for Valine/Al ₂ O ₃ (top) and Valine/Ag/Al ₂ O ₃ (bottom): FWO method.....	88
Figure A3. TGA kinetic analysis for Leucine/Al ₂ O ₃ (top) and Leucine/Ag/Al ₂ O ₃ (bottom): FWO method.....	89
Figure A4. TGA kinetic analysis for Alanine/Al ₂ O ₃ (top) and Alanine/Ag/Al ₂ O ₃ (bottom): KAS method.....	90
Figure A5. TGA kinetic analysis for Valine/Al ₂ O ₃ (top) and Valine/Ag/Al ₂ O ₃ (bottom): KAS method.....	91
Figure A6. TGA kinetic analysis for Leucine/Al ₂ O ₃ (top) and Leucine/Ag/Al ₂ O ₃ (bottom): KAS method.....	92
Figure A7. Alanine/Al ₂ O ₃ synchronous 2D-COS spectra (top-left), asynchronous 2D-COS spectra (top-right) and FTIR spectra at different temperatures (bottom).....	96
Figure A8. Alanine/Al ₂ O ₃ oxidation products mass spectra: NH ₃ , H ₂ O, CO, CO ₂ (left); NO, NO ₂ , (CH ₃) ₂ CO (right). Uncalibrated MS traces were displaced vertically to facilitate reading.....	97
Figure A9. Alanine/Ag/Al ₂ O ₃ synchronous 2D-COS spectra (top-left), asynchronous 2D-COS spectra (top-right) and FTIR spectra at different temperatures (bottom).....	98
Figure A10. Alanine/Ag/Al ₂ O ₃ oxidation products mass spectra: NH ₃ , H ₂ O, CO, NO, CO ₂ (left); NO ₂ , (CH ₃) ₂ CO (right). Uncalibrated MS traces were displaced vertically to facilitate reading.....	99
Figure A11. Valine/Al ₂ O ₃ synchronous 2D-COS spectra (top-left), asynchronous 2D-COS spectra (top-right) and FTIR spectra at different temperatures (bottom).....	100
Figure A12. Valine/Al ₂ O ₃ oxidation products mass spectra: NH ₃ , H ₂ O, CO, CO ₂ (left); NO, (CH ₃) ₂ CO, NO ₂ (right). Uncalibrated MS traces were displaced vertically to facilitate reading.....	101

Figure A13. Valine/Ag/Al₂O₃ synchronous 2D-COS spectra (top-left), asynchronous 2D-COS spectra (top-right) and FTIR spectra at different temperatures (bottom).....102

Figure A14. . Valine/Ag/Al₂O₃ oxidation products mass spectra: NH₃, H₂O, CO, CO₂ (left); NO, (CH₃)₂CO, NO₂ (right). Uncalibrated MS traces were displaced vertically to facilitate reading.....103

Figure A15. Leucine/Al₂O₃ synchronous 2D-COS spectra (top-left), asynchronous 2D-COS spectra (top-right) and FTIR spectra at different temperatures (bottom).....104

Figure A16. Leucine/Al₂O₃ oxidation products mass spectra: NH₃, H₂O, CO, (CH₃)₂CO, CO₂ (left); NO, NO₂ (right). Uncalibrated MS traces were displaced vertically to facilitate reading.....105

Figure A17. Leucine/Ag/Al₂O₃ synchronous 2D-COS spectra (top-left), asynchronous 2D-COS spectra (top-right) and FTIR spectra at different temperatures (bottom).....106

Figure A18. Leucine/Ag/Al₂O₃ oxidation products mass spectra: NH₃, H₂O, CO, (CH₃)₂CO, CO₂ (left); NO, NO₂ (right). Uncalibrated MS traces were displaced vertically to facilitate reading.....107

Figure A19. Glycine/ α -Al₂O₃ synchronous (left) and asynchronous (right) 2D-COS spectra....108

Figure A20. Correlation values of the asynchronous spectra for the wavenumber 3160 cm⁻¹...109

List of Tables

Table 1.1. Review of Patents involving use of metal/metal oxides in virus deactivation.....	4
Table 1.2. Review of press releases involving inventions and innovations related to Covid-19....	6
Table 1.3. Amino acids present in coronavirus spike protein.....	11
Table 1.4. Regions of Infrared Radiation.....	16
Table 3.1. Summary of calculated activation energy and pre-exponential factors during thermal decomposition of AA/ α -Al ₂ O ₃ in oxygen	58
Table 3.2. Summary of calculated activation energy and pre-exponential factors during thermal decomposition of AA/Ag/ α -Al ₂ O ₃ in oxygen.....	58
Table 4.1. Glycine and Alanine Bond Dissociation Energies (E: Enthalpy and FE: Free Energy in kcal/mol) as Determined from NREL's ALFABET Machine Learning Approach.....	65
Table 4.2. Valine and Leucine Bond Dissociation Energies (E: Enthalpy and FE: Free Energy in kcal/mol) as Determined from NREL's ALFABET Machine Learning Approach.....	67
Table 4.3. Comparison of functional groups reaction order.....	74
Table A1. Physical properties of the used materials.....	81
Table A2. Silver catalyst preparation target values and calculations required for the impregnation solution and number of impregnations.....	82
Table A3. Amino acid water solubilities.....	83
Table A4. Amino acid/Alumina.....	83
Table A5. Amino acid/Ag/Alumina.....	83
Table A6. Reported peak assignments for glycine, alanine, valine and leucine.....	84
Table A7. Possible amino acid decomposition products reported in literature.....	86
Table A8. Example of mass spectrometry products m/z values vs % intensity.....	86
Table A9. Glycine/ α -Al ₂ O ₃ calculated activation energy and pre-exponential factors.....	93
Table A10. Glycine/Ag/ α -Al ₂ O ₃ calculated activation energy and pre-exponential factors.....	93
Table A11. Alanine/ α -Al ₂ O ₃ calculated activation energy and pre-exponential factors.....	93

Table A12. Alanine/Ag/ α -Al₂O₃ calculated activation energy and pre-exponential factors.....94

Table A13. Valine/ α -Al₂O₃ calculated activation energy and pre-exponential factors.....94

Table A14. Valine/Ag/ α -Al₂O₃ calculated activation energy and pre-exponential factors.....94

Table A15. Leucine/ α -Al₂O₃ calculated activation energy and pre-exponential factors.....95

Table A16. Leucine/Ag/ α -Al₂O₃ calculated activation energy and pre-exponential factors.....95

Chapter 1. Introduction and Review

The outbreak of COVID-19 and its widespread transmission across the world has reasserted the need for understanding viruses. According to the World Health Organization (WHO) the latest numbers (January 2020) show around three hundred and forty million confirmed cases of COVID-19 worldwide at a rate of about five hundred thousand new cases per day, resulting in approximately five and a half million deaths.¹ Consequently, the study of interactions of viruses and large biomolecules is of great importance, as are possible ways to characterize and monitoring them.

1.1 COVID-19 and Possible Methods of Virus Deactivation

Viruses are non-living elements containing genetic material that require host cells to acquire the energy and material they need to replicate and thus transmit. On its own, a virion (a single virus particle) consists of a capsid within which genetic material, i.e., DNA or RNA, is contained and that is composed of proteins and occasionally other macromolecules such as lipids and fats.²

The virus that causes COVID-19 is the SARS-CoV-2 virus and its structure is depicted in **Figure 1.1**.¹ The structure of the SARS-CoV-2 virus consists of a nucleocapsid protein that holds the genetic material (RNA in this case). It is enclosed by a membrane and an envelope protein. Protruding out of the membrane are the proteins which allow the virus to attach to host cells during infection and they are called spike proteins.³ These spike proteins are responsible for the transmission of COVID-19.⁴

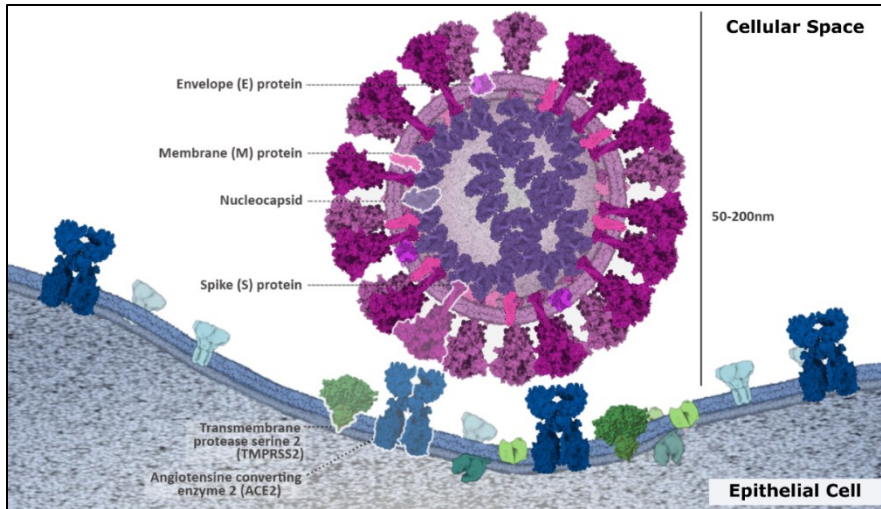


Figure 1.1. Coronavirus structure³

During infection, the spike proteins of the coronavirus attach to the ACE2 receptors which are present in the membrane of the host cells (**Figure 1.2**). After the attachment occurs, the virus penetrates the host cell membrane. The virus then opens up, exposing the cell to its genetic material. Replication of the virus initiates and after a new virion is assembled, its release takes place. The infection of the virus thus continues, leading to widespread transmission.⁵⁻⁷

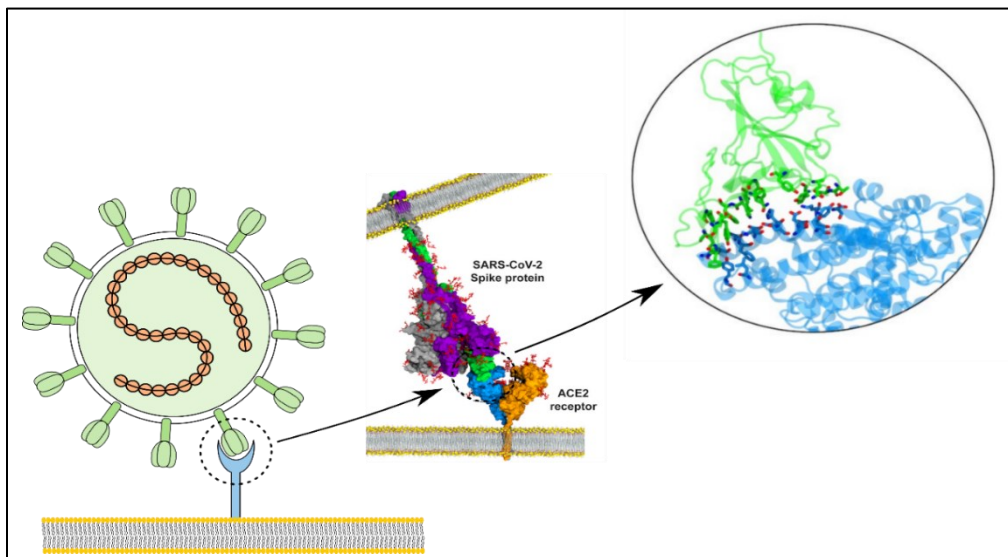


Figure 1.2. Schematics of COVID-19 transmission⁴

Virus particles in the environment have been treated or deactivated using several methods over the years. Some of these procedures include heat treatment, chemicals, or UV irradiation for virus disinfection.⁸ From a catalysis point of view, metals and metal oxides are also a viable means of achieving virus deactivation. In fact, metals have been used for their antimicrobial properties for over thousands of years. The earliest record of such practice was found in Egyptian text dating back to 2600-2200 B.C. which described the use of copper in sterilizing wounds and drinking water.⁹

In more recent times, metal and metal oxide catalysts have been studied as antimicrobial agents. Studies in the literature show the usage of metals such as Au in inhibiting HIV, Herpes and Hepatitis C,^{10, 11} Ag for deactivating H1N1 and Hepatitis B,^{5, 12} Cu for inactivating Influenza and Calicivirus^{13, 14} and other metals tested on various viruses. Some of the metal oxides that have been examined include ZnO,¹⁵ TiO₂,^{16, 17} and CuO,¹⁸ among others. Some of the factors that affect the behavior of viruses with metals (and metal oxides) that have been found include surface charge,^{5, 19} catalyst particle size,²⁰ temperature,²¹ and others.

1.2. Patents Review

A review of the patents in the field of virus deactivation along with a review of the many innovations and inventions made over the past year to combat COVID-19 transmission show the utilization of one or different combinations of the above mentioned materials and techniques. Information about the mechanism of virus deactivation, however, is limited. The patented use of metal catalysts in deactivating viruses and other pathogens has been considerable and some are summarized in **Table 1.1**. These patents describe applications that include numerous products of several forms consisting of a wide variety of metals, metal oxides and other compounds that follow different methods for achieving virus deactivation.

Table 1.1. Review of Patents involving use of metal/metal oxides in virus deactivation²²⁻³⁹

No.	Patent Number	Year	Keywords	Assignee(s)	Form	Primary Component	Secondary Component	Tertiary Component	Synthesis method	Catalysis Mode	Applications
1	JP 2020040374 A	2020	Antimicrobial material for fluid	Ibiden Co. Ltd.	Resin	Cu, Ag, or Zn	Alkoxide of copper	-	Adhesion and drying	Heterogeneous	Interiors, decorations, furniture ²³
2	JP 2020083772 A	2020	Antimicrobial components	Ibiden Co. Ltd.	Coating	Cu, Ag, or Zn	Ti or W	-	Spraying and drying	Heterogeneous, photocatalysis	Coating ²³
3	JP 2019011418 A	2019	Coating composition	Nippon Paint Co. Ltd.; Toto Co. Ltd.	Coating	TiO ₂	Diatomaceous earth or zeolite	-	Crystallization	Heterogeneous, photocatalysis	Coating ²⁴
4	JP 2019099514 A	2019	Antivirus agent and resin	Nippon Electric Glass Co. Ltd.	Coating	SiO ₂	Ag ₂ O or CuO or ZnO	-	Melting and cooling	Heterogeneous	Coating ²⁵
5	JP 2019178076 A	2019	Antivirus composition	Sumika Environmental Science Co. Ltd.	Coating	Ag ₂ MoO ₄ double salt	Alkali metal salts (Li, Na, K)	-	Precipitation	Heterogeneous	Coating ²⁵
6	JP 3222178 U	2019	Antiviral textile and bedding	Masaaki, Fujimoto	Fiber	Zn	-	-	Kneading/dyeing	Heterogeneous	Fiber ²⁷
7	JP 2018002597 A	2018	Antiviral agent and fiber product	Nicca Chemical Co.; Showa Denko K. K.	Fiber	TiO ₂	Cu ²⁺	-	Impregnation or kneading	Heterogeneous, photocatalysis	Fiber ²⁸
8	JP 2018058826 A	2018	Antiviral agent Zn(OH) ₂ , TiO ₂	Osaka Gas Chemicals Co. Ltd.	Powder, solution	Zn(OH) ₂ , Zn ₃ (PO ₄) ₂	Ti ₃ (PO ₄) ₄ , TiO ₂	-	Pulverization and solution	Heterogeneous, photocatalysis	Paints, coatings, masks ²⁹
9	JP 2018083179 A	2018	Surface treatment agent	Akira, Oki	Powder, coating	Ag or Cu	TiO ₂	Nd	Pulverization + electroplating	Heterogeneous, photocatalysis	Surface treatment agent ³⁰
10	JP 2018172462 A	2018	Antiviral plastic	Sumika Environmental Science Co. Ltd.	Plastic	1. Ag, Zn, or Cu oxides	Molybdenum oxide	-	Precipitation	Heterogeneous, photocatalysis	Wallpaper, floor, sheet, film ³¹
11	JP 2016033109 A	2016	Glass + film and composition	Asahi Glass Co. Ltd.	Film	SiO ₂	Ag	Li, Na, K	Desalting	Heterogeneous	Glass coating ³²
12	JP 2016108267 A	2016	Antimicrobial agent rutile TiO ₂	Daicel Corporation	Crystal	TiO ₂	-	-	Solution + drying	Heterogeneous, photocatalysis	Coating ³³
13	JP 2015117187 A	2015	Antiviral resin	Panasonic IP Management Co. (JP)	Coating	CuO	TiO ₂	Iron oxide or Al ₂ O ₃ , ZnO, BaSO ₄ , ZrO ₂	Dispersion	Heterogeneous, photocatalysis	Tiles, filters, textiles, industrial, medical equipment, interiors ³⁴
14	JP 2015195826 A	2015	Bactericidal/antiviral components	NBC Meshtec Co. Ltd.	Fiber, film, sheet, resin	HAlCl ₄ , H ₂ PCl ₄	-	-	Dehydration-condensation	Heterogeneous	Filters, clothes, nets, curtains, masks, gloves, wallpaper ³⁵
15	JP 2014074243 A	2014	Photocatalyst inclusion fiber	Japan Esdan Co. Ltd.	Fiber	TiO ₂ , WO ₃ , or ZnO	-	-	Solution + spinning	Heterogeneous, photocatalysis	Garments, curtains, bedding, rugs ³⁵
16	JP 5914890 B2	2014	Copper TiO ₂ complex	Panasonic IP Management Co. (JP)	Coating	Cu ₂ O	TiO ₂	-	Dispersion	Heterogeneous, photocatalysis	Wallpaper, auto interior, filters, furniture, households ³⁷
17	JP 2013082654 A	2013	Antimicrobial/antiviral composition	Showa Denko KK; University of Tokyo	Coating, film, article	CuO	TiO ₂ or WO ₃	-	Reduction + mixing	Heterogeneous, photocatalysis	Coating agent, film, article ³⁸
18	JP 2013106561 A	2013	Bedding for livestock/poultry	Nishiki Shizai Co. Ltd.	Sand-like particles	TiO ₂ , WO ₃	SiO ₂	-	Visible light irradiation	Heterogeneous, photocatalysis	Livestock, poultry bedding ³⁹

Table 1.1. Review of Patents involving use of metal/metal oxides in virus deactivation (Continued)⁴⁰⁻⁵⁸

No.	Patent Number	Year	Keywords	Assignee(s)	Form	Primary Component	Secondary Component	Tertiary Component	Synthesis method	Catalysis Mode	Applications
19	JP 2013126623 A	2013	Catalyst with antiviral cloth	Tokushu Muki Zairyo Kenkyusho	Film, sheet	Ti, V oxalate, Zr(OAc) ₄	-	-	Charge and dry	Heterogeneous, photocatalysis	Coating, fabric ⁴⁰
20	JP 2013154282 A	2013	Photocatalyst and electronic device	Konica Minolta Inc.	Film, coating	TiO ₂ or WO ₃	PrO ₃ or Au ₂ O ₃	Fe ₂ O ₃ or CuO	Mixing, drying, irradiating	Heterogeneous, photocatalysis	Film, resin, coating ⁴¹
21	JP 2013212997 A	2013	Antiviral material of Cu and CuO	NBC Meshtec Inc. (JP)	Nanofiber	Cu	CuO	-	Electrochemical treatment	Heterogeneous	Coating, filter, mask, cap, medical drapes, paper ⁴²
22	JP 2012020969 A	2012	Palladium antiviral agent	NBC Meshtec Inc. (JP)	Powder, fiber, resin	Pd	-	-	Adsorption + reduction	Heterogeneous	Masks, filters, clothes, nets ⁴³
23	JP 2012024566 A	2012	Wiping sheet	NBC Meshtec Inc. (JP)	Sheet	AgI or CuI	-	-	Pulverization	Heterogeneous	Wiping sheet ⁴⁴
24	JP 2011153163 A	2011	Method for inactivating a virus	Univ. Tokyo; Kanagawa Acad Sci & Technol (JP)	Powder, film	Cu ₂ O, Cu ₂ S, CuI or CuCl	TiO ₂	-	Solution/filtration + centrifugation	Heterogeneous, photocatalysis	Interior in homes, hospitals, electrical appliances, filters ⁴⁵
25	JP 2011213719 A	2011	Gold nanoparticles as antiviral agents	NBC Meshtec Inc. (JP)	Powder, fiber	Au, TiO ₂	-	-	Precipitation, spraying	Heterogeneous, photocatalysis	Powder, fiber ⁴⁶
26	JP 2010168578 A	2010	Antiviral paint with copper	NBC Meshtec Inc. (JP)	Fiber, film, sheet, resin	CuCl, CuBr, Cu(CH ₃ COO)	-	-	Pulverization	Heterogeneous	Filter, mask, bedding, clothing, building material ⁴⁷
27	JP 2003221304 A	2003	Antiviral agent, paint and base	Catalysts & Chemicals Industries Co. Ltd.	Paint, fiber, resin	AgO, CuO or ZnO	-	-	Colloidal solution	Heterogeneous	Paint ⁴⁸
28	WO 2016099417 A1	2016	Antibacterial and antiviral facemask	Kaya, Ceangiz et. al.	Fiber	zeolite support	-	-	Mixing + drying	Heterogeneous	Mask ⁴⁹
29	WO 2014068575 A1	2014	Agricultural barrier for crop cultivation	Tosaf Compounds Ltd.	Barrier	TiO ₂ , ZnO, ZrO ₂ , CdO, CrO or CuO	TiO ₂ , ZnO, ZrO ₂ , CdO, CrO or CuO	PE, PP, PC, ETFE, PVC, PVA, EBA	Mixing	Heterogeneous, photocatalysis	Walls ⁵⁰
30	WO 2014092747 A1	2014	Metal oxide complexes in polymer	Wingfield, W.; Grume, G.L.; Mason, R.L.	Solution	AgO, CuO, ZnO, TiO ₂ , Au ₂ O ₃ , NiO	glycerin or polyethylene glycol	-	Chelation	Heterogeneous, photocatalysis	Food additive ⁵¹
31	WO 2014184989 A1	2014	Photocatalytic and Cu ₂ O coating	Panasonic IP Management Co.	Coating	TiO ₂ , WO ₃ , SrTiO ₃ , ZnO, Nb ₂ O ₅ , SnO ₂	Cu ₂ O	glycol ether solvent	Mixing	Heterogeneous, photocatalysis	Coating ⁵²
32	WO 2014204290 A1	2014	Titanium dioxide with citric extracts	León Gutiérrez, G.	Surface	TiO ₂ or ZnO or Al ₂ O ₃	(OH), (NH) ₂ , (SO) ₄ , (PO) ₄	-	Impregnation	Heterogeneous, photocatalysis	Surface ⁵³
33	WO 2013008807 A1	2013	Antiviral agent	Sumitomo Chemical Co., Ltd.; TUAT, Tokyo	Coating	tungsten oxide	Cu, Pt, Au, Pd, Ag, Ru, Ir, Rh	Si alkoxide (binder)	Dispersion	Heterogeneous, photocatalysis	Glass, appliances, textiles, handrails, elevator buttons ⁵⁴
34	WO 2013160898 A1	2013	Surface application to fibers	Argaman Technologies Ltd.	Fiber	Ag, AgO, Cu, Cu ₂ O, Mg, MgO	ZnO, TiO ₂	-	Plating	Heterogeneous, photocatalysis	Yarns, woven, knit, or non-woven textiles ⁵⁵
35	WO 2012046803 A1	2012	Antibacterial antiviral glass fiber	Takeda, S.	Fiber	SiO ₂	Cu, Zn or Ag	-	Immersion and heating	Heterogeneous	Air purifier ⁵⁶
36	WO 2011018899 A1	2011	Antiviral material, film, fiber	Toshiba Materials Co. Ltd. (JP)	Film, fiber, coating	TiO ₂	Cu or Ag or Zn	-	Dispersion	Heterogeneous, photocatalysis	Masks, auto, hospitals, homes interiors and appliances ⁵⁷
37	WO 2011040048 A1	2011	Virus inactivating sheet	NBC Meshtec Inc. (JP)	Sheet	CuCl, CuI, CuBr, CuO, CuS or CuSCN	Iodides of: Cu, Ag, Pt, Bi, Au, Fe, Co, Ni, Zn	-	Stacking fleece layers	Heterogeneous	Bedsheet, suit, glove, medical drape, cap, filter, gauze, surgical tps, wallpaper ⁵⁸

Table 1.1. Review of Patents involving use of metal/metal oxides in virus deactivation (Continued)⁵⁹⁻⁷⁶

No.	Patent Number	Year	Keywords	Assignee(s)	Form	Primary Component	Secondary Component	Tertiary Component	Synthesis method	Catalysis Mode	Applications
38	WO 2010016082 A1	2010	Decontamination equipment	Nm Tech Ltd. Nanomater Microdevices Technol	Shell	TiO ₂ , SiO ₂ or ZnO	-	-	Spraying	Heterogeneous, photocatalysis	Air decontamination equipment ⁵⁹
39	WO 2010026730 A1	2010	Antiviral agent	NBC Meshtec Inc. (JP)	Powder, fiber, resin, film, sheet	CuI, AgI, SnI ₄ , CuCl, CuBr, CuSCN	-	-	Spinning and adsorption	Heterogeneous catalysis	Mask, air filter, clothes, screen, net, wallpaper, wrapping bag ⁶⁰
40	WO 2009022100 A1	2009	Antiviral composition	Intrinsic Materials Limited (UK)	Coating, fiber	WC, W ₂ X ₃ ; X= Si or Te	TiO ₂	-	Co-deposition	Heterogeneous, photocatalysis	Fabrics, filters, paints ⁶¹
41	WO 2008043396 A1	2008	Anti-microbial products	Nm Tech Ltd. Nanomater Microdevices Technol	Coating	TiO ₂ , SiO ₂ , or ZnO	Ag ⁺ or Cu ²⁺	-	Adsorption	Heterogeneous, photocatalysis	Coating ⁶²
42	WO 2007093808 A2	2007	Virucidal material	Queen Mary & West. Col. Qinetiq Nano Ltd.; Retros. Virol. Ltd. (GB)	Fiber	Cu, W, Ni, Zn, Al, Ca	-	-	Evaporation-condensation	Heterogeneous, photocatalysis	Protective clothing, filters ⁶³
43	US 20190045793 A1	2019	Antiviral, coating, resin, product	Toosogsei Co. Ltd. (JP)	Coating	Ag or Cu ions	-	phosphoric/silicic acid	Mixing	Heterogeneous	Fibers, textiles ⁶⁴
44	US 20180200397 A1	2018	Antiviral disinfectant	Kimberly Clark Worldwide Inc.	Solution	Maleic, succinic or phosphoric acid	anionic N-acyl compounds	Alkali metals, ethoxylates, amines	Solution	Homogeneous	Surface disinfectant ⁶⁵
45	US 20130315972 A1	2013	Antimicrobial metal nanoparticles	Agienic Inc.	Coating	copper iodide	-	-	Grinding	Heterogeneous	Coating ⁶⁶
46	US 20120027809 A1	2012	Pharmaceutical compositions	Bar-Ilan University	Drug	Ag or Au nanoparticles	-	-	One phase method	Heterogeneous	Drug ⁶⁷
47	US 20110171062 A1	2011	Antimicrobial Coatings	Penn State Res Foundation	Coating	ZrO ₂ and Eu ₂ O ₃	Y ₂ O ₃	-	Vapor deposition	Heterogeneous	Surfaces, floors Sterilization ⁶⁸
48	US 20080269186 A1	2008	Antibacterial, Antiviral nanomaterials	Nm Tech Ltd. Nanomater Microdevices Technology	Crystal	TiO ₂ or SiO ₂	Ag ⁺ or Cu ²⁺	-	Precipitation and heating	Heterogeneous, photocatalysis	Medicament ⁶⁹
49	US 20070190174 A1	2007	Antiviral colloidal silver composition	American Silver LLC (US)	Suspension	Ag	AgO	-	Dispersion	Heterogeneous	Drug ⁷⁰
50	CN 103974469 B	2013	Metallic heating element	Qingdao Econ Technol Develop Zone Haier Water Heater Co. Ltd.	Coating	SiO ₂	B ₂ O ₃	TiO ₂ , CoO, Al ₂ O ₃ , CaO, ZrO ₂ , Ag, Cu	Mixing, heating, cooling, drying	Heterogeneous, photocatalysis	Metal heating element ⁷¹
51	CN 104054753 A	2014	Antibacterial and sterilization	Nantong Snakebite Therapy Research Institute	Solution	TiO ₂ , ZnO, Al ₂ O ₃ , Ag ₃ PO ₄ , zeolite	Ag	-	Mixing	Heterogeneous, photocatalysis	Sterilization, disinfection of livestock, poultry, houses ⁷²
52	CN 105019312 A	2014	Multifunctional wallpaper and coating	Shanghai World Prospect Chemtech Co. Ltd.	Coating	TiO ₂ , ZnO, hydrated SiO ₂ , ZnO	Ag, AgCl, Ag ₂ O, CuO, Cu ₂ O, Cu(OH) ₂	TiO ₂ , SiO ₂	Mixing	Heterogeneous, photocatalysis	Wallpaper ⁷³
53	CN 105152683 A	2015	Antibacterial ceramic glaze	Shandong Jianzhu University	Ceramic glaze	SiO ₂	Al ₂ O ₃ , CaO, ZnO	CuO, MgO, TiO ₂ , Ag ₂ O	Powder and fining	Heterogeneous, photocatalysis	Glaze layer ⁷⁴
54	CN 207594471 U	2017	A kind of antiviral sheet	Guangzhou Akso Healthy New Material Co. Ltd.	Sheet	ZnO	Al ₂ O ₃	TiO ₂	Impregnation	Heterogeneous, photocatalysis	Plank ⁷⁵
55	PL 223968 B1	2012	Aqueous borate complexes	Szczepaniak, D. et al.	Solution	citrate-borate of Ag ⁺ , Cu ²⁺ , Zn ²⁺	-	-	Reduction	Heterogeneous, homogeneous	Solution ⁷⁶

The different metals used in these applications include silver,^{22, 23, 30, 32, 54-57, 67, 70-73} copper,^{22, 23, 30, 42, 55-57, 63, 64, 70, 71} zinc,^{22, 23, 27, 56, 57, 63} gold,^{46, 54, 67} palladium,^{43, 54, 58} tungsten,^{23, 63} aluminum,⁶³ calcium,⁶³ lithium,³² magnesium,⁵⁵ manganese,⁵⁵ neodymium,³⁰ nickel,⁶³ platinum,⁵⁴ potassium,³² sodium³² and titanium,²³ among others.

Other compounds used as catalysts were oxides and other compounds of titanium,^{28-30, 33-35-41, 46, 50-53, 55, 57, 59, 61, 62, 69, 72-75} copper,^{22, 26, 28, 31, 34, 37, 38, 41, 42, 44, 45, 47, 48, 50-52, 55, 58, 60, 62, 66, 69, 70, 73, 74} zinc,^{26, 29, 31, 34, 35, 48, 50-53, 55, 58, 59, 62, 72-76} silver,^{25, 26, 31, 44, 48, 51, 55, 58, 60, 62, 64, 69, 70, 72-74, 76} silicon,^{26, 32, 49, 56, 59, 61, 62, 69, 71, 74} tungsten,^{35, 38, 39, 41, 52, 54, 61} aluminum,^{49, 53, 72, 74, 75} gold,^{36, 41, 51, 58} tin,^{51, 52, 58, 60} zirconium,^{34, 40, 50, 68} iron,^{34, 41, 58} platinum,^{36, 41, 58} antimony,^{58, 71} calcium,^{71, 74} cobalt,^{58, 71} magnesium,^{55, 74} mercury,^{50, 58} molybdenum,^{25, 31} nickel,^{51, 58} potassium,^{25, 65} sodium,^{25, 65} barium,³⁴ bismuth,⁵⁸ boron,⁷¹ cadmium,⁵⁰ chromium,⁵⁰ europium,⁶⁸ germanium,⁵⁸ hafnium,⁵⁰ indium,⁵⁸ iridium,⁵⁴ lithium,²⁵ niobium,⁵² rhodium,⁵⁴ ruthenium,⁵⁴ strontium,⁵² tellurium,⁶¹

thallium,⁵⁸ vanadium,⁴⁰ ytterbium,⁶⁸ and more.

Most patents used catalysts that offered more than one mode of catalytic activity. The use of metallic catalysts such as gold, silver, copper etc. suggest heterogeneous catalysis.^{22, 26-27, 32-36, 42-44, 47-49, 56, 58, 60, 64, 66-68} However, most applications combined these catalysts with photocatalysts such as titania and tungsten oxides to enhance catalytic activity.^{23, 24, 28-31, 33-35-41, 45, 46, 50-55, 57, 59, 61-63, 69, 71-75} Some products also suggested the presence of homogeneous catalysis.^{65 76}

The applications of the above metals and compounds comprised of products such as fibers and textiles,^{27, 28, 34-35, 40, 42, 43 46, 47, 49, 54-57, 60, 61, 63, 64} paints and coatings,^{23-25, 29, 32, 33, 38, 40-42, 48, 52, 61, 62, 66} interiors,^{22, 31, 34-37, 45, 47, 50, 54, 57, 60, 73, 75} personal protective equipment (PPE),^{29, 36, 42, 43, 47, 49, 57, 58, 60, 63} disinfectants,^{30, 39, 44, 53, 65, 68, 72, 74, 76} masks,^{29, 36, 42, 43, 47, 49, 57, 60} air filters^{56, 59-61} and medicaments.^{51, 67, 69, 70}

While a large number of patents were from Japan,^{22-48 52 54 56-58 60} there were also a considerable number from the USA,^{51, 55, 64-70} China⁷¹⁻⁷⁵ and the United Kingdom⁶¹⁻⁶³ along with others from Israel,⁵⁰ Italy,⁵⁹ Mexico,⁵³ Poland⁷⁶ and Turkey,⁴⁹ among other countries. Some of the notable companies involved in the field were NBC Meshtec,^{36, 42-44, 46, 47 58, 60} Panasonic,^{34, 37, 52} Ibiden,^{22, 23} Daicel,³³ Kimberly-Clark,⁶⁵ Osaka Gas,²⁹ Toagosei⁶⁴ and Toshiba.⁵⁷

1.3. News Releases and Developments Review

In what follows we will review some recent developments in public releases as summarized in **Table 1.2**. Although these releases are not peer reviewed, they provide an insight into the level of interest and applications deployed to the general public. While most of the applications use metals or other metallic compounds such as oxides,⁷⁷⁻⁸² others utilize ultraviolet light,⁸³⁻⁸⁷ electric charge⁸⁸⁻⁹⁰ and plasma,^{90, 91} among others, which are in line with those found in the patent literature. The usage of metals and metal oxides may be attributed to catalysis and

their known anti germicidal properties; metals such as copper,^{78, 79, 81, 82} nickel,⁸⁰ silver⁷⁸ and zinc⁷⁷ are known for their catalytic properties. Ultraviolet light of 254 nm wavelength is a known germicide but direct exposure to such radiation is hazardous to health as it can cause severe burns of the skin and eye damage.^{83, 84, 87} Far ultraviolet light, which is ultraviolet light with a wavelength of 222 nm, cannot penetrate the eye or outer dead-cell skin layer and has been considered a safer method of ultraviolet disinfection.^{85, 86} Other methods include the use of electric charge to repel virus containing particles.⁸⁸⁻⁹⁰ Additionally, plasma has also been used as a natural disinfectant to kill bacteria and viruses on exposure.^{90, 91}

The applications reviewed include products such as masks and PPEs,^{77-79, 89, 92-99} disinfectants and sanitizers,^{81-87, 90, 91, 100, 101} air filters and purifiers,^{80, 85, 88, 90, 102, 103} respiratory-assist devices,¹⁰⁴⁻¹⁰⁷ and various other applications.^{96, 108-112}

Boeing,^{83, 84} LG,⁹⁹ Mercedes-AMG,¹⁰⁷ and Virgin Orbit¹⁰⁵ are among the major companies involved in these inventions. Institutions working on related products include Columbia University,⁸⁵ Harvard,⁹⁶ MIT,⁹⁶ Universities of Arizona,¹⁰⁴ California,¹¹¹ Hong Kong,⁸¹ Houston,⁸⁰ Illinois,¹¹² Kentucky,⁹⁵ Michigan,⁹⁰ and Virginia Tech,⁸¹ among others.

Table 1.2. Review of press releases involving inventions and innovations related to COVID-19

No.	Device	Company/Organization	Country	Date	Notes
1	Acteev Biodefend™	Ascend Performance Materials	USA	06/2020	Embedded active Zn ions in matrix of specialty polymer to prepare antiviral mask ⁷⁷
2	SurfaceWise2™	Allied Bioscience, Inc.	USA	08/2020	Coating of ammonium polymer twists virus's proteins and attacks its protective layer of fat ¹⁰⁰
3	UV wand	Boeing, Healthe® Inc. and Far UV Technol Inc.	USA	09/2020	UV wand sanitizes the inside of an airplane ^{83 84}
4	B2 Mask	BREATHE99	USA	04/2020	Reusable mask with changeable filters blocking 98.3-99.6% of airborne particles (>0.1 microns) ⁹²
5	UVC lamp	Columbia University	USA	06/2020	>99.9% of seasonal coronaviruses present in airborne droplets were killed when exposed to a far UV light safe to use around humans ⁸⁵
6	Krypton™ Disinfection Lighting	Far UV Technologies Inc.	USA	03/2020	Uses far UV(222nm) light to disinfect ⁸⁶
7	Nasal Spray	Halberd Corporation	USA	11/2020	Utilizes antibody with a solution which blocks ACE2 receptors found in nasal epithelial cells ¹⁰⁸
8	iWave Air Purifiers	iWave	USA	04/2021	Uses needle-point bi-polar ionization ¹⁰²
9	Air sterilization mask	Kepley BioSystems Inc.	USA	06/2020	Active, continuous bio-deactivation of bacteria, fungi, viral and allergenic/antigenic matter ⁹³
10	Antibacterial face mask	Kronos Advanced Technologies Inc.	USA	07/2020	Mask using silver, copper or other materials that have antibacterial threads ⁷⁸
11	Kronos® Air 5G® Air Purifiers	Kronos Advanced Technologies Inc.	USA	04/2020	Electrically charged ions trap and destroy mold, allergens, bacteria, and infectious viruses ⁸⁸
12	Copper Mesh Insert	Kuhn Copper Solutions	USA	06/2021	Cu mesh which can be inserted/worn in mask ⁷⁹
13	Kuhn All Coper Mask	Kuhn Copper Solutions	USA	06/2021	Reusable copper masks ⁷⁹
14	ViralWall™ air purifier	LIGC Applications	USA	03/2021	Uses laser-induced graphene technology to purify air, eliminating over 99% of captured airborne bacteria, viruses and micro-particles ¹⁰³
15	Guardian G-Volt mask	LIGC Applications	USA	05/2020	Applies electric charge to surface to sterilize and repel particles trapped in its graphene filter ⁸⁹
16	Cold Plasma Disinfection Device	Princeton Plasma Physics Lab.; D.O.E	USA	10/2020	Provides “cold” plasma(room-temperature) to keep surfaces disinfected ⁹¹
17	Silicon nitride	SINTX Technologies, Inc.	USA	03/2021	Cleaves RNA by specific, off-stoichiometric chemical reactions and by the release of reactive nitrogen species ¹¹⁰

Table 1.2. Review of press releases involving inventions and innovations related to COVID-19

No.	Device	Company/Organization	Country	Date	Notes
18	Respiratory-Assist Device	University of Arizona	USA	04/2020	Small-scale, low-pressure system that simultaneously removes CO ₂ while adjusting for humidity in a closed system ¹⁰⁴
19	AeroNabs	University of California San Francisco	USA	08/2020	Synthetic molecules that attack the parts of the virus which allow it to infect ¹¹¹
20	Heated Nickel Air Filters	University of Houston; Galveston National Lab.	USA	07/2020	Heating the foam made of nickel to 200 °C eliminate 99.8 % of airborne viruses in a room ⁸⁰
21	Smartphone attachment to detect people infected with bacteria, viruses	University of Illinois at Urbana-Champaign	USA	04/2020	Reagent containing cartridge attached to smartphone which detects RNA of pathogens ¹¹²
22	Antiviral Mask	University of Kentucky	USA	04/2020	Membrane including proteolytic enzymes that attach to the protein spikes of the coronavirus and separate them ⁹⁵
23	Plasma Jet Wand	University of Michigan	USA	04/2020	Plasma produced by running air through high electric field destroy cell walls of pathogens ⁹⁰
24	Coating Deactivating COVID-19	Virginia Tech and University of Hong Kong	USA	07/2020	Cu ₂ O/polyurethane coating ⁸¹
25	Sensor	Wyss Institute – Harvard University and MIT	USA	06/2021	Sensor on face mask that detects COVID-19 virus ⁹⁶
26	Virustatic Shield	Carrington Textiles and Pincroft Dyeing and Printing	UK	03/2020	Mask ⁹⁷
27	CovaGuard™	Covalon Technologies Ltd.	Canada	03/2020	Benzalkonium chloride used as sanitizer ¹⁰¹
28	TrioMed Active mask	I3 BioMedical Inc.	Canada	07/2020	Tri-Iodide antimicrobial used ⁹⁸
29	Violet	Akara Robotics	Ireland	12/2020	Robot using UV light to disinfect ⁸⁷
30	Sanitizing booths	MV Engineering s.r.l.s.; Glowapp s.r.l.	Italy	05/2020	Uses potassium, proximosulfate or euchlorine (KNaCu ₃ (SO ₄) ₃ O) compounds as sanitizing products ⁸²
31	PuriCare™ Wearable Air Purifier	LG Electronics	South Korea	06/2020	Wearable air purifier/mask ⁹⁹

1.4. Hypothesis

While the patents and inventions described above employ various components and methods of deactivation, the details of the mechanisms involved, however, remain largely unknown. The coronavirus, not unlike other life forms, is primarily composed of amino acids (second to water).¹¹³ In fact, the beginning of life on earth itself can be attributed to amino acids,

such is their importance. The molecules of life, as they are called, include proteins, lipids, carbohydrates and nucleic acids and amino acids are the building blocks for all proteins.^{114, 115}

The spikes of the coronavirus are long chain glycoproteins which are proteins consisting of oligosaccharides cross-linked with amino acids as shown in **Figure 1.3**.¹¹⁶

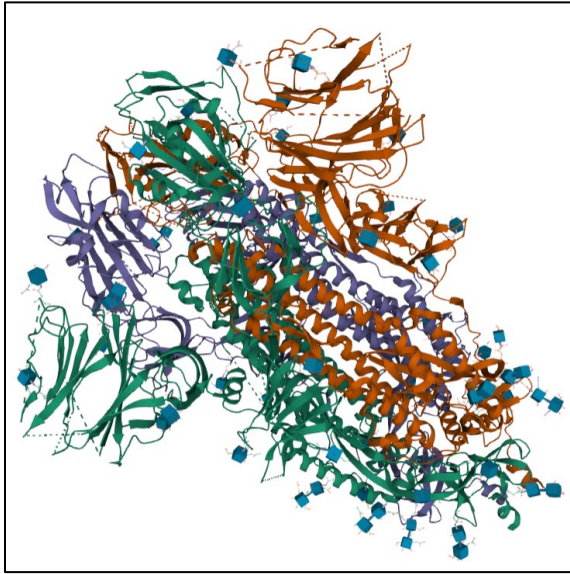


Figure 1.3. Coronavirus spike protein showing long chains of cross-linked aminoacids^{117, 118}

Figure 1.4 shows the structure of the spike protein expressed as a sequence of amino acids; in this sequence, each letter corresponds to an amino acid. A single spike protein consists of 1281 amino acid residues with leucine (~8.6%) and serine (~7.8%) making up the majority of the composition.^{117, 118} A description of aminoacids, code, strcuture, and count in a single spike protein is shown in **Table 1.3**.

```

VFNATRFASVYAWNRRKRISNCVADSVLYNSASFSTFKCYGVSPTKLNDLCFTNVYADSFVIRGDEVQRQIAPGQTGKIADYNYKLPDDFTGCVIAWNSNLDKSVGGNYNYLYRFRKSNLKPFFERDISTEIYQAGSTPCNGVEGFNCYFPLQSYGF
LLHAPATVCGPKKSTNLVKNKCVNFNFNGLTGTGVLTESNKKFLPFQGFGRDIADTTDAVRDPQTLLEILDITPCSFGGVSVITPGTNTSNQVAVLYQDVNCTEVPVAIHADQLTPTWRVYSTGSNVFTQTRAGCLIGAEHVNNSYECDIPIGAGICASYGF
TMSLGAENSVAYSNNIAIPTNFTISVTTEILPVSMTKTSVDCMTYICGDSTECNSLLQYGSFCTQLNRALTGIAVEQDKNTQEVFAQVKQIYKTPPIKDFGGFNFSQILPDPSPKPSKRSFIEDLLFNKVTLADAGFIKQYGDCLGDIARDLCAQKFNGL
AGTITSGWTFGAGAALQIPFAMQMAYRFGNGVTONVLYENQKLIANQFNSAIGKIQDSLSTASALGKLDVVNQNAQALNTLVKQLSSNFGAISSVLDLNDLSRLDPPEAEVQIDRLITGRQLSLQTYVTQQLIRAAEIRASANLAATKMSVCLGOSKI
HGIVFLHVTYVPAQEKNFITPAICHDGKAHFPREGVFSNGTHWFVTRQNFYEPQIIITDNTFVSGNCDVVIGVNNNTVYDPLQPELDSFKEELDKYFKNHTSPDVLGDISGINASVVNIQKEIDRLNEVAKNLNESLIDLQELGKYEYIKGSGREN

```

Figure 1.4. Spike protein aminoacid sequence^{117, 118}

Table 1.3. Amino acids present in coronavirus spike protein¹¹⁷⁻¹¹⁹

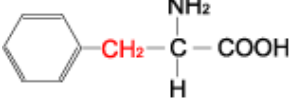
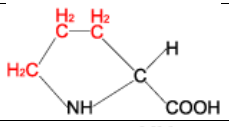
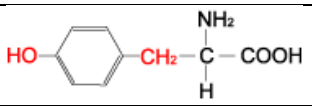
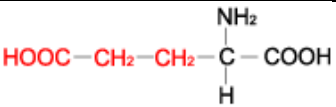
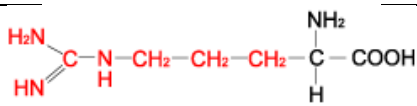
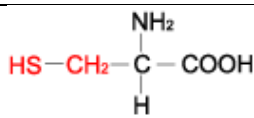
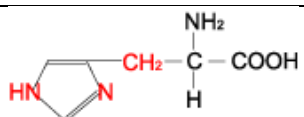
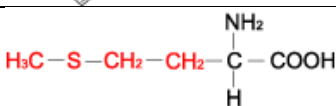
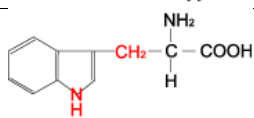
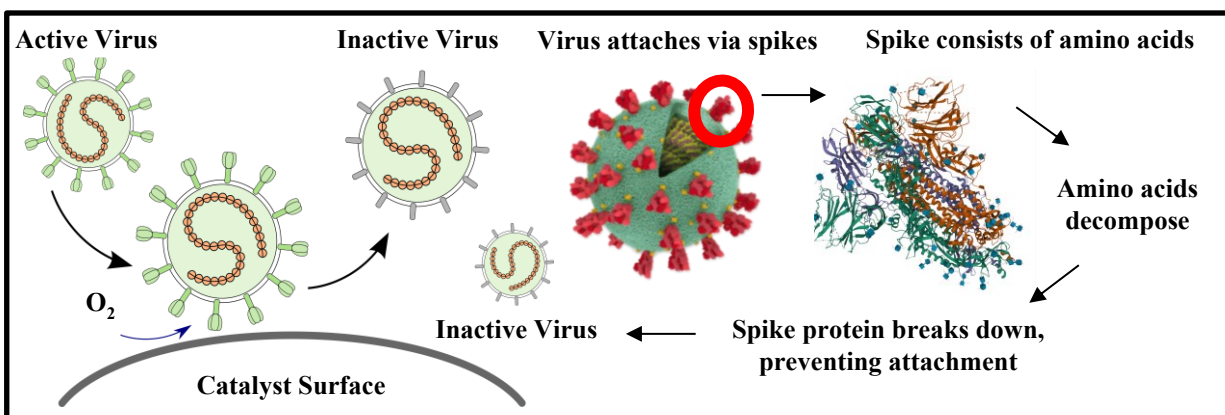
No.	Amino Acid	Code	Structure	Count	Percentage
1	Leucine	L	$ \begin{array}{c} \text{H}_3\text{C} \\ \diagdown \\ \text{CH} - \text{CH}_2 - \text{C} - \text{COOH} \\ \diagup \\ \text{H}_3\text{C} \\ \\ \text{H} \\ \\ \text{NH}_2 \end{array} $	110	8.59
2	Serine	S	$ \begin{array}{c} \text{NH}_2 \\ \\ \text{HOH}_2\text{C} - \text{C} - \text{COOH} \\ \\ \text{H} \end{array} $	100	7.81
3	Threonine	T	$ \begin{array}{c} \text{NH}_2 \\ \\ \text{H}_3\text{C} - \text{CHOH} - \text{C} - \text{COOH} \\ \\ \text{H} \end{array} $	97	7.57
4	Valine	V	$ \begin{array}{c} \text{H}_3\text{C} \\ \diagdown \\ \text{CH} - \text{C} - \text{COOH} \\ \diagup \\ \text{H}_3\text{C} \\ \\ \text{H} \\ \\ \text{NH}_2 \end{array} $	94	7.34
5	Glycine	G	$ \begin{array}{c} \text{NH}_2 \\ \\ \text{H} - \text{C} - \text{COOH} \\ \\ \text{H} \end{array} $	93	7.26
6	Asparagine	N	$ \begin{array}{c} \text{NH}_2 \\ \\ \text{H}_2\text{N} - \text{CO} - \text{CH}_2 - \text{C} - \text{COOH} \\ \\ \text{H} \end{array} $	89	6.95
7	Alanine	A	$ \begin{array}{c} \text{NH}_2 \\ \\ \text{H}_3\text{C} - \text{C} - \text{COOH} \\ \\ \text{H} \end{array} $	81	6.32
8	Phenylalanine	F		75	5.85
9	Isoleucine	I	$ \begin{array}{c} \text{CH}_3 \quad \text{NH}_2 \\ \quad \\ \text{H}_3\text{C} - \text{CH}_2 - \text{CH} - \text{C} - \text{COOH} \\ \\ \text{H} \end{array} $	73	5.70
10	Glutamine	Q	$ \begin{array}{c} \text{NH}_2 \\ \\ \text{H}_2\text{N} - \text{CO} - \text{CH}_2 - \text{CH}_2 - \text{C} - \text{COOH} \\ \\ \text{H} \end{array} $	64	5.00
11	Proline	P		62	4.84
12	Aspartate	D	$ \begin{array}{c} \text{NH}_2 \\ \\ \text{HOOC} - \text{CH}_2 - \text{C} - \text{COOH} \\ \\ \text{H} \end{array} $	61	4.76
13	Lysine	K	$ \begin{array}{c} \text{NH}_2 \\ \\ \text{H}_2\text{N} - \text{CH}_2 - \text{CH}_2 - \text{CH}_2 - \text{CH}_2 - \text{C} - \text{COOH} \\ \\ \text{H} \end{array} $	57	4.45

Table 1.3. Amino acids present in coronavirus spike protein (Continued)¹¹⁷⁻¹¹⁹

No.	Amino Acid	Code	Structure	Count	Percentage
14	Tyrosine	Y		55	4.29
15	Glutamate	E		50	3.90
16	Arginine	R		42	3.28
17	Cysteine	C		31	2.42
18	Histidine	H		24	1.87
19	Methionine	M		13	1.01
20	Tryptophan	W		10	0.78

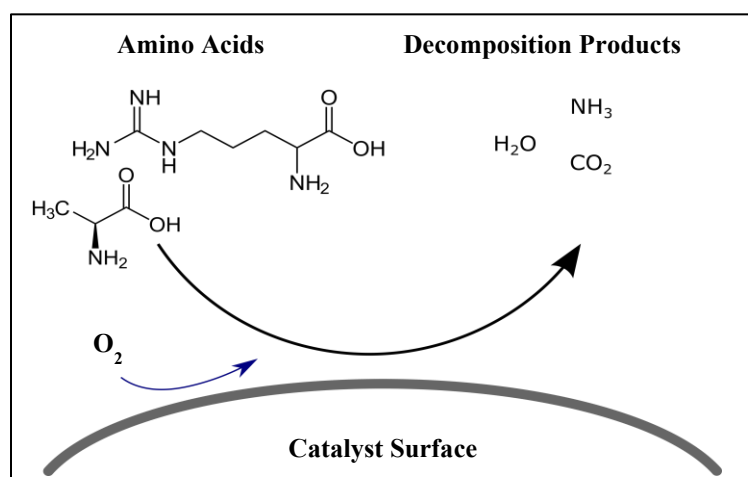
As COVID-19 spreads due to the SARS-CoV-2 spike protein and since the spike protein is primarily made up of amino acids, deactivation of the virus could be achieved by reactions with these amino acids; for example, if amino acids were to decompose, the spike protein would break down and the virus unable to attach to the host cell, rendering it inactive.

Using catalysts, we can come up with a possible mechanism for virus deactivation, as it has been implied from common intuition, experience, and the patent literature. One hypothesis is that when viruses get deposited on the catalyst, the spike proteins come into contact with the surface; it then reacts with oxygen present in the air under heat, decomposing the amino acids of the spike proteins on the surface. This would result in virions with damaged spikes unable to attach to host cells, thereby deactivating the virus as depicted in **Scheme 1.1**.



Scheme 1.1. Possible route and mechanism of virus deactivation¹¹⁷

We hypothesize that the mechanism of amino acids decomposition on a catalyst surface in the presence of oxygen at moderate temperatures may be key to understand the deactivation of viruses. *This work mainly focuses on the interactions of amino acids with metal and metal oxides under oxygen atmosphere as studied in real time with in situ spectroscopic techniques* in order to lay a foundation for the study of larger biomolecules and ultimately viral proteins and viruses where oxidation reactions may be key to their deactivation.



Scheme 1.2. Simplified mechanism of amino acid decomposition in oxygen atmosphere and on a catalyst surface

1.5. Characterization

A key aspect of this work is to find a simple method of identifying and monitoring changes to virus components (e.g., spike protein amino acids) and studying their decomposition in real time. The current method used worldwide for detecting COVID-19 is the Reverse Transcription Polymerase Chain Reaction (RT-PCR) method.¹²⁰ In this procedure, samples are collected from a person's nose or throat and sent to laboratories for testing. After treatment, the RNA is extracted, and reverse transcribed to DNA using a particular enzyme. Short fragments of DNA complementary to the transcribed viral DNA are then added and the sample is placed in a RT-PCR machine, where the temperature is cycled through high and low temperatures to initiate reactions that create identical copies of specific target sections of the viral DNA. As the cycles are repeated, markers are attached to the strands of the DNA that release dyes. After the amplification is completed, the amount of dye released is used to determine whether a test is positive or negative. The test takes, on an average, about 6 to 8 hours to yield results. Moreover, this does not take into account the time taken for transporting the samples from the collection sites to the testing laboratories.^{120, 121} If one was to monitor the presence of viruses on surfaces or to evaluate the efficiency of metals or metal oxides for virus deactivation, the above method would be unpractical.

A faster and less complex method to identify and monitor changes to the virus components could be achieved by using spectroscopic techniques such as Infrared or Raman spectroscopies.^{122, 123} The use of spectroscopy to analyze biological samples is now called biospectroscopy¹²⁴ and has been used to detect entities such as bacteria, cancer, and viruses among others. In this work on amino acids, we propose the use of Fourier Transform Infrared (FTIR) spectroscopy coupled with Two-Dimensional Correlation Spectroscopy analysis (2D-

COS) to identify and track surface changes of adsorbed amino acids. As a proof of concept for the application of the above techniques, we study physical mixtures of amino acids and a common metal oxide (i.e., Al_2O_3) and metal oxide supported ($\text{Ag}/\text{Al}_2\text{O}_3$) catalyst per prior literature review (**Tables 1.1** and **1.2**). Thermogravimetric Analysis (TGA) was also employed to give insight into the temperature ranges involved in the decomposition reactions of the model physical mixture samples.

1.5.1. Thermogravimetric Analysis (TGA)

Thermogravimetric Analysis (TGA) is a method that records the mass of a sample placed in a furnace as the temperature is increased at a programmable ramp rate in the presence of a gas flow, which can be an inert like N_2 or reactive such as O_2 . The mass of the sample decreases with increasing temperature as some components evaporate (for example, moisture) or when reactions like oxidation take place. TGA therefore combines the recorded mass loss, temperature, and time to assist studies such as conversion, kinetics of decomposition and oxidation, etc.¹²⁵

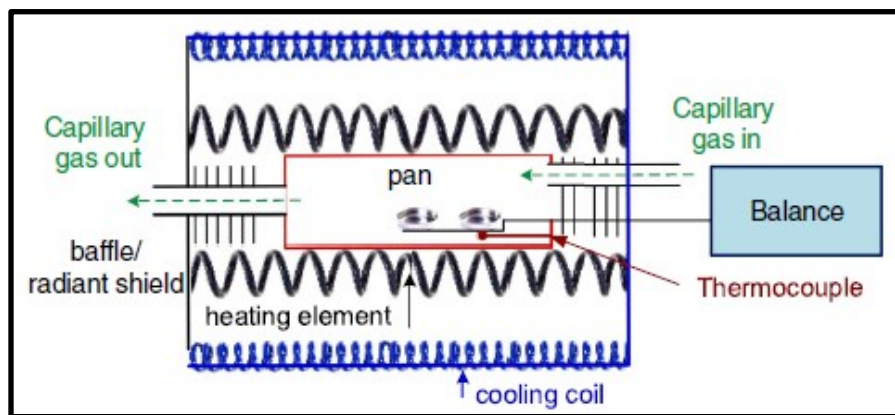


Figure 1.5. Layout of a typical Thermogravimetric Analysis (TGA) setup¹²⁵

The TGA instrument consists of a sensitive microbalance connected to a pan or pans (where one is used as a reference) enclosed in a furnace. A temperature controller and programmer are also present to set specific temperature ramps and methods. A thermocouple

near the pan measures temperature and gas flows over the pan through an inlet and outlet at both ends of the furnace.^{126 127}

The results of a TGA experiment are displayed in the form of a thermogram, which are graphical representations of change in mass versus time or temperature.¹²⁸ The first derivative of the profile can be also graphed, showing points of inflection in the mass profile.¹²⁹ In this work, TGA was utilized to find temperature ranges of thermal decomposition for amino acids and to provide a preliminary comparison of catalyst vs support performance.

1.5.2. Fourier Transform Infrared Spectroscopy (FTIR)

Infrared spectroscopy utilizes the vibrations that occur in molecules and materials when they are exposed to infrared radiation to study their structure.¹³⁰ Infrared radiation consists of multiple regions which can be differentiated as near, mid, and far IR as listed in **Table 1.4**.¹³⁰

Table 1.4. Different Regions of Infrared Radiation¹³⁰

Region	Wavelength (nm)	Wavenumber (cm ⁻¹)
Near IR (NIR)	780-2500	12800-4000
Mid IR (MIR)	2500-25000	4000-400
Far IR (FIR)	25000-1000000	400-10

For heterogenous catalysis studies the region of interest is the Mid Infrared region (4000-400 cm⁻¹) as this is where resonances with molecular vibrational frequencies take place.^{131, 132} The most commonly used instrument for Infrared absorption is the Fourier Transform Infrared spectrometer due to its increased efficiency thanks to the Michelson interferometer.^{130, 131} This interferometer is used to generate interferograms which are signals arising due to changing path lengths between two beams. Fourier transformation is then applied to translate the distance to

frequency in order to calculate wavenumbers,¹³³ after which a mercury cadmium telluride or MCT detector is used to collect the light after interaction.¹³⁴ **Figure 1.6** shows the working of a Michelson interferometer.¹³⁴ During operation, light gets transmitted to a fixed mirror which gets reflected back, recombining with light reflecting to and from the moving mirror at the beam splitter after which it leaves the interferometer and interacts with the sample.

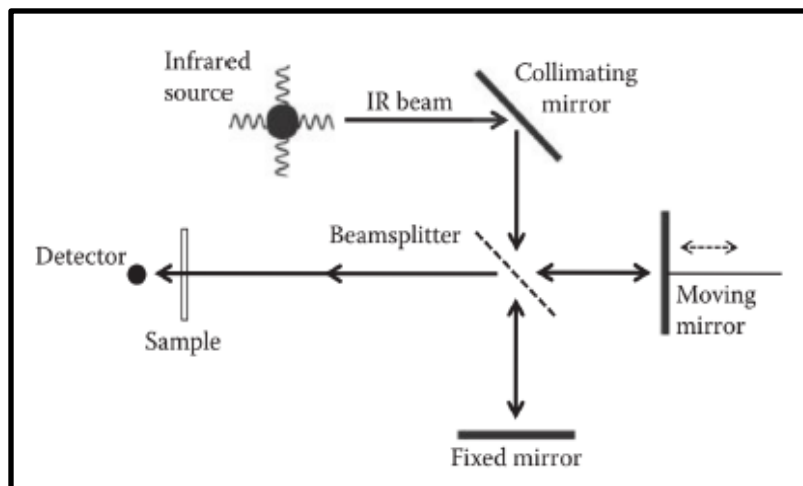
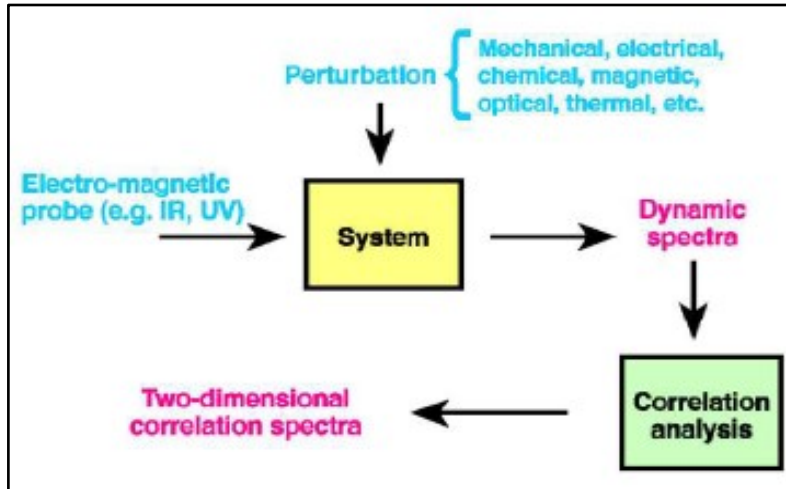


Figure 1.6. Schematic representation of a Michelson interferometer¹³⁴

1.5.3. Two-Dimensional Correlation Spectroscopy (2D-COS)

1.5.3.1. Introduction

2D Correlation spectroscopy (2D-COS) is a tool which plots spectral intensity as a function of two independent spectral variables. Two orthogonal axes of spectral variables define the spectral plane with intensity plotted on a third axis.^{135, 136} 2D-COS is based on the 2D Correlation analysis used for detecting dynamic variations induced by an external perturbation.¹³⁷ The use of a second dimension and correlation helps identify overlapped peaks in spectra which may otherwise not be visible.¹³⁵



Scheme 1.3. General scheme for obtaining 2D Correlation spectra¹³⁸

1.5.3.2. Theory

Considering a pair of dynamic IR signals measured at two different wavenumbers $x(\nu_1, t)$ and $y(\nu_2, t)$ varying with respect to time t , the correlation function $R(\nu_1, \nu_2)$ is the product of the two functions shifted by a time constant τ and can be shown as:

$$R_{xy}(\tau) = \int_{-\infty}^{\infty} x(t) y(t + \tau) dt \quad (1)$$

Fourier transformation (FT) of the correlation function is done to convert this information to the frequency domain (from the time domain) so we get:

$$S_{xy}(\omega) = \int_{-\infty}^{\infty} R_{xy}(\tau) e^{-i\omega\tau} d\tau \quad (2)$$

The overall relationship between the two signals can then be found by summing the correlation function for all ω (> 0). As the FT is a complex operator, the FT of the correlation function can be separated into its real and imaginary parts, and thus we arrive at:

$$\frac{1}{\pi T} \int_0^{\infty} S_{xy}(\omega) d\omega = \Phi_{xy} + i\Psi_{xy} \quad (3)$$

Here, the LHS of the equation corresponds to the calculated overall correlation function. On the RHS, the real part gives information about correlations occurring in-phase, and the imaginary part, out-of-phase (where one signal lags the other); these are known respectively as synchronous

and asynchronous 2D correlation plots. Calculation of the synchronous plot can be done by evaluating the correlation function at $\tau = 0$. Therefore,

$$\Phi_{xy} = R_{xy}(0) \quad (4)$$

Evaluation of the asynchronous plot in one of Noda's approaches involves the application of the Hilbert transform (HT) in place of FT. For $y(t)$, HT of $y(t)$ is given by:

$$h(t') = \frac{1}{\pi} p. v. \int_{-\infty}^{\infty} \frac{y(t)}{t-t'} dt \quad (5)$$

where p. v. is the Cauchy principal value and t' the offset in time. The asynchronous plot is then found by correlation of $x(t)$ and HT of $y(t)$ at $\tau = 0$ or:

$$\Psi_{xy} = R_{xh}(0) \quad (6)$$

Hence, the 2D Correlation plots can be evaluated.¹³⁹

1.5.3.3. Interpretation of 2D-COS spectra

2D-COS synchronous and asynchronous plots are typically presented as contours of their surface plots. For example, **Figure 1.7** shows the 2D-COS synchronous and asynchronous plots for a system in the form of both surface plots and contours.^{139, 140}

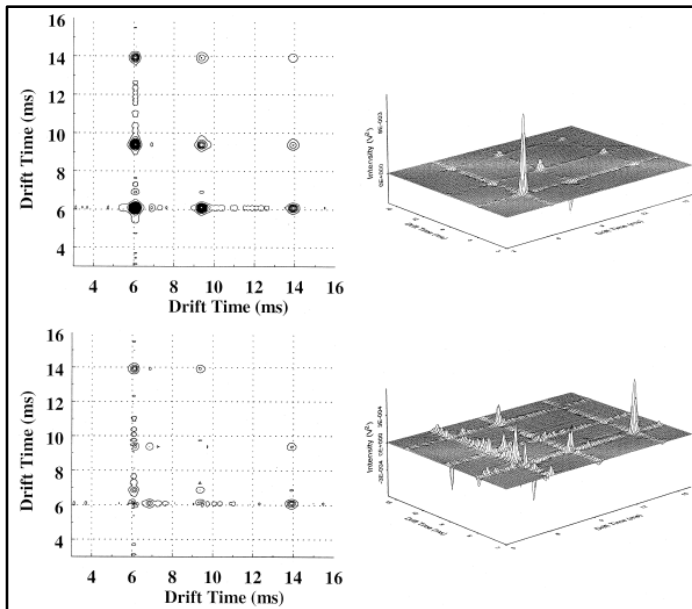


Figure 1.7. Example of 2D COS synchronous spectra (top) and asynchronous plots (bottom)¹³⁹

To get a clearer picture of 2D-COS results, **Figure 1.8** presents a standard example of the synchronous and asynchronous components of 2D-COS spectra. The synchronous spectrum gives information about changes that take place in phase or synchronously (at the same time). The peaks along the diagonal, called auto-peaks, show correlation of each element with itself (as wavenumbers on both x and y axis are equal in the 2D-COS in IR). Peaks occurring away from the diagonal are called cross-peaks and represent the correlation of different elements with one another. The cross-peaks in a synchronous spectrum are symmetric about the diagonal. While the intensities of the auto-peaks are always positive, those of the cross-peaks can be either positive or negative; while positive cross-peaks occur if both elements increase or decrease together, negative cross-peaks arise when one element increases while the other decreases.^{139, 140}

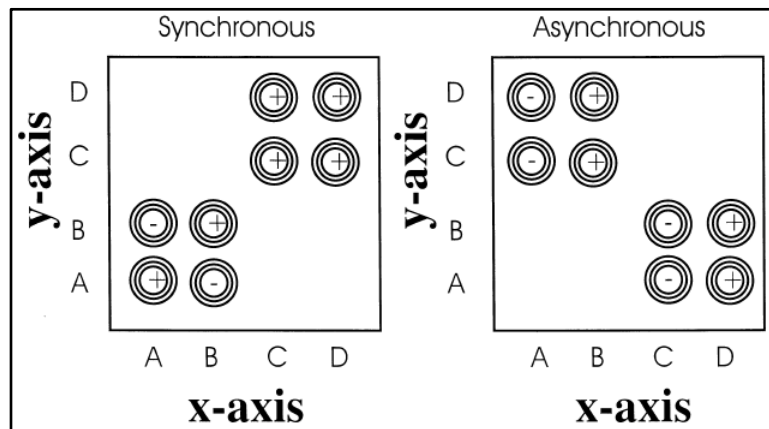


Figure 1.8. Examples of synchronous and asynchronous 2D-COS plots¹³⁹

The asynchronous plot in **Figure 1.8** displays behavior that occurs out of phase. As an element cannot be correlated out of phase with itself, the asynchronous plot does not show auto-peaks along the diagonal. The cross-peaks here are antisymmetric about the diagonal. The temporal information present in the asynchronous plot can be interpreted in tandem with the synchronous spectrum; for a particular point (x, y) , positive peaks in both the synchronous and asynchronous plots imply that the element represented by the x coordinate leads the change in the element represented by the y coordinate. If the synchronous spectrum has a positive peak

while the asynchronous spectrum has a negative one, the element corresponding to the x coordinate lags the one corresponding to the y coordinate. For the scenario where the synchronous spectrum shows a negative peak, the interpretation of the asynchronous spectrum is reversed.

1.5.3.5. Conclusion

Both synchronous and asynchronous plots are instrumental to gather the most information possible about a system, the correlation between two elements (e.g., two wavenumbers), their level of synchronization, and relative dynamic changes.

1.6. References

1. Coronavirus numbers. <https://covid19.who.int/> (accessed December 27, 2021).
2. Boeckmans, J.; Rodrigues, R. M.; Demuyser, T.; Piérard, D.; Vanhaecke, T.; Rogiers, V., COVID-19 and drug-induced liver injury: a problem of plenty or a petty point? *Arch Toxicol* **2020**, *94* (4), 1367-1369.
3. Rodríguez, M. P. How SARS-CoV-2 interacts with the surface proteins of the target cell. <https://pdb101.rcsb.org/news/2020> (accessed December 27, 2021).
4. Dubrow, A. Hidden states of the Covid-19 Spike Protein. <https://www.tacc.utexas.edu/-/hidden-states-of-the-covid-19-spike-protein> (accessed December 27, 2021).
5. Chen, L.; Liang, J., An overview of functional nanoparticles as novel emerging antiviral therapeutic agents. *Materials science & engineering. C, Materials for biological applications* **2020**, *112*, 110924-110924.
6. Vausselin, T.; Calland, N.; Belouzard, S.; Descamps, V.; Douam, F.; Helle, F.; François, C.; Lavillette, D.; Duverlie, G.; Wahid, A.; Fénéant, L.; Cocquerel, L.; Guérardel,

- Y.; Wychowski, C.; Biot, C.; Dubuisson, J., The antimalarial ferroquine is an inhibitor of hepatitis C virus. *Hepatology* **2013**, *58* (1), 86-97.
7. Matsumoto, Y.; Matsuura, T.; Aoyagi, H.; Matsuda, M.; Hmwe, S. S.; Date, T.; Watanabe, N.; Watashi, K.; Suzuki, R.; Ichinose, S.; Wake, K.; Suzuki, T.; Miyamura, T.; Wakita, T.; Aizaki, H., Antiviral Activity of Glycyrrhizin against Hepatitis C Virus In Vitro. *PLOS ONE* **2013**, *8* (7), e68992.
8. Pfaender, S.; Brinkmann, J.; Todt, D.; Riebesehl, N.; Steinmann, J.; Steinmann, J.; Pietschmann, T.; Steinmann, E.; Griffiths, M. W., Mechanisms of Methods for Hepatitis C Virus Inactivation. *Applied and Environmental Microbiology* **2015**, *81* (5), 1616-1621.
9. Grass, G.; Rensing, C.; Solioz, M., Metallic copper as an antimicrobial surface. *Applied and Environmental Microbiology* **2011**, *77* (5), 1541-1547.
10. Lee, M.-Y.; Yang, J.-A.; Jung, H. S.; Beack, S.; Choi, J. E.; Hur, W.; Koo, H.; Kim, K.; Yoon, S. K.; Hahn, S. K., Hyaluronic Acid–Gold Nanoparticle/Interferon α Complex for Targeted Treatment of Hepatitis C Virus Infection. *ACS Nano* **2012**, *6* (11), 9522-9531.
11. Halder, A.; Das, S.; Ojha, D.; Chattopadhyay, D.; Mukherjee, A., Highly monodispersed gold nanoparticles synthesis and inhibition of herpes simplex virus infections. *Materials Science and Engineering: C* **2018**, *89*, 413-421.
12. Mori, Y.; Ono, T.; Miyahira, Y.; Nguyen, V. Q.; Matsui, T.; Ishihara, M., Antiviral activity of silver nanoparticle/chitosan composites against H1N1 influenza A virus. *Nanoscale Research Letters* **2013**, *8* (1), 93.
13. Borkow, G.; Zhou, S. S.; Page, T.; Gabbay, J., A Novel Anti-Influenza Copper Oxide Containing Respiratory Face Mask. *PLOS ONE* **2010**, *5* (6), e11295.

14. Shionoiri, N.; Sato, T.; Fujimori, Y.; Nakayama, T.; Nemoto, M.; Matsunaga, T.; Tanaka, T., Investigation of the antiviral properties of copper iodide nanoparticles against feline calicivirus. *Journal of Bioscience and Bioengineering* **2012**, *113* (5), 580-586.
15. Singh, T. A.; Sharma, A.; Tejwan, N.; Ghosh, N.; Das, J.; Sil, P. C., A state of the art review on the synthesis, antibacterial, antioxidant, antidiabetic and tissue regeneration activities of zinc oxide nanoparticles. *Advances in Colloid and Interface Science* **2021**, *295*, 102495.
16. Cho, M.; Chung, H.; Choi, W.; Yoon, J., Different Inactivation Behaviors of MS-2 Phage and *Escherichia coli* in TiO₂ Photocatalytic Disinfection. *Applied and Environmental Microbiology* **2005**, *71* (1), 270-275.
17. Page, K.; Palgrave, R. G.; Parkin, I. P.; Wilson, M.; Savin, S. L. P.; Chadwick, A. V., Titania and silver–titania composite films on glass—potent antimicrobial coatings. *Journal of Materials Chemistry* **2007**, *17* (1), 95-104.
18. Hang, X.; Peng, H.; Song, H.; Qi, Z.; Miao, X.; Xu, W., Antiviral activity of cuprous oxide nanoparticles against Hepatitis C Virus in vitro. *Journal of Virological Methods* **2015**, *222*, 150-157.
19. Gerba, C. P., Applied and Theoretical Aspects of Virus Adsorption to Surfaces. In *Advances in Applied Microbiology*, Laskin, A. I., Ed. Academic Press: 1984; Vol. 30, pp 133-168.
20. Semagina, N.; Kiwi-Minsker, L., Recent Advances in the Liquid-Phase Synthesis of Metal Nanostructures with Controlled Shape and Size for Catalysis. *Catalysis Reviews* **2009**, *51* (2), 147-217.
21. Knight, C. A., Chemistry of Viruses. In *Chemistry of Viruses*, Knight, C. A., Ed. Springer Vienna: Vienna, 1963; pp 1-177.

22. Horino, K. Antimicrobial member with excellent antiviral and antifungal properties. JP2020040374A, 2020.
23. Yokota, T.; Ito, K.; Otsuka, K.; Takada, K.; Adachi, K.; Horino, K. Antimicrobial member using binder cured product containing antimicrobial component. JP2020083772A, 2020.
24. Matsushima, M.; Kawakami, S.; Oka, K.; Sato, K.; Takami, K.; Fujii, H.; Fukushima, T. Coating composition containing photocatalytic titanium oxide and coating film with low discoloration. JP2019011418A, 2019.
25. Kato, Y. Antiviral composition containing benzotriazole compounds and method for imparting antiviral function. JP2019178076A, 2019.
26. Sawasato, H. Antiviral agent comprising silicate glass, and resin molded product using the same. JP2019099514A, 2019.
27. Tanaka, H. Fiber product having good antibacterial, antiviral and deodorizing effects. JP3222178U, 2019.
28. Teranishi, Y.; Tsuge, Y.; Kuroda, Y.; Li, D. Antiviral agent containing titanium oxide and quaternary compound, and antiviral textile product. JP2018002597A, 2018.
29. Kishida, T.; Ebata, I. Antiviral agent containing zinc hydroxide and titanium oxide. JP2018058826A, 2018.
30. Oki, A. Surface treatment agent containing titanium dioxide for wrist watch, bracelet and mobile phone, and surface treatment method. JP2018083179A, 2017.
31. Kato, Y. Antiviral plastic. JP2018172462A, 2018.
32. Suwa, K. Coated glass and film-forming composition which can suppress occurrence of yellowing due to silver with excellent antibacterial and antiviral nature. JP2016033109A, 2016.

33. Matsuoka, M. N., T. Antimicrobial agent rutile type titanium oxide. JP2016108267A, 2016.
34. Ueda, T.; Yamashina, D.; Kinugawa, K. Antiviral resin composition and anti-viral member. JP2015117187A, 2015.
35. Komiyama, T.; Yamato, Y. Photocatalyst-containing fibers and fiber structures containing them. JP2014074243A, 2014.
36. Naohara, Y.; Hayata, H.; Nagao, T.; Nakayama, T. Antibacterial/antiviral member, mask, and filter comprising the same. JP2015195826A, 2015.
37. Ueda, T.; Yamashina, D.; Kinugawa, K. Copper complex titanium oxide dispersion liquid, coating material composition, and antibacterial/antiviral member. JP5914890B2, 2014.
38. Hashimoto, K.; Sunada, K.; Miyauchi, M.; Li, D.; Kuroda, Y. Antimicrobial and antiviral composition comprising cuprous oxide, and method of producing the same. JP2013082654A, 2013.
39. Ogawa, T. Livestock and poultry litter comprising porous inorganic oxide particles and photocatalytic fine particles supported thereon, and method for preventing viral infection using the litter. JP2013106561A, 2013.
40. Irie, T.; Shirasawa, H.; Suzuki, K.; Okajima, T. Catalyst body having positive holes in absence of light, its manufacture, and antiviral and antimicrobial cloth containing it. JP2013126623A, 2013.
41. Suzuki, S. Photocatalyst article, its manufacture, and electronic device. JP2013154282A, 2013.
42. Fukui, Y.; Fujimori, Y.; Nakayama, T. Antivirus copper-based nanofiber materials, and production thereof. JP2013212997A, 2013.

43. Fujimori, Y. N., Yohei; Kobayashi, Yuk; Fukui, Yoko; Nakayama, Tsuruo Antiviral agents containing palladium or palladium oxide and antiviral members having the agents. JP2012020969A, 2012.
44. Iwatani, T. F., Yoshie; Naohara, Yohei; Nakayama, Tsuruo Antiviral and antibacterial wipe sheets containing metal compound fine particles. JP2012024566A, 2012.
45. Hashimoto, K.; Sunada, K.; Kubota, Y.; Ishiguro, H.; Nakano, R.; Kajioka, S.; Yao, Y. Virus inactivators comprising monovalent copper compounds, and virus-inactivating materials. JP2011153163A, 2011.
46. Naohara, Y. F., Yoshie; Fukui, Yoko; Nakayama, Tsuruo Preparation method of gold nanoparticles as antiviral agents. JP2011213719A, 2011.
47. Fujimori, Y.; Nakayama, T.; Fukui, Y. Antiviral coatings for (non)enveloped viruses and their applied fiber structures. JP2010168578A, 2010.
48. Tanaka, A.; Koyanagi, T.; Shirono, K. Coating materials containing antiviral agents. JP2003221304A, 2003.
49. Kaya, C.; Eren, G. O.; Kaya, F.; Ergen, A.; Gurbuz, G.; Unlu, S.; Soy, M.; Noberi, C. Modular antimicrobial and antiviral facial mask and bamboo layer for social infestations. WO 2016099417 A1 2016.
50. Fleicher, M.; Moyal, Y.; Dinar, M. Agricultural thermoplastic polymer pest repellent barrier with nanoparticles for crop cultivation. WO2014068575A1, 2014.
51. Wingfield, W.; Grune, G. L.; Mason, R. L. Metal oxide complexes and infusion of complexes into polymer compounds. WO2014092747A1, 2014.

52. Miki, S.; Ueda, T.; Yamashina, D.; Kinugawa, K. Photocatalytic particle- and cuprous oxide-containing coating composition and the antimicrobial and antiviral member therefrom. WO2014184989A1, 2014.
53. Leon Gutierrez, G. Nanoparticulate titanium dioxide nanomaterial modified with functional groups and with citric extracts adsorbed on the surface, for the removal of a wide range of microorganisms. WO2014204290A1, 2014.
54. Sakatani, Y.; Takami, H.; Sogabe, K.; Takehara, K. Antiviral agents containing photocatalysts and method for inactivating nonenveloped virus. JP2013018736A, 2013.
55. Greenwald, J. Method for the surface application of chemical compounds to both synthetic and natural fibers and a system for same. WO2013160898A1, 2013.
56. Takeda, S. Process for producing antibacterial and antiviral glass fiber material. WO2012046803A1, 2012.
57. Nakano, K.; Sato, A.; Kusaka, T.; Kasamatsu, S.; Sasaki, A.; Fukushi, D. Antiviral material and film, fiber, and product using same. WO2011018899A1, 2011.
58. Fujimori, Y.; Jikihara, Y.; Sato, T.; Fukui, Y.; Nakayama, T. Virus inactivation sheet comprising monovalent copper compound and/or iodide fine particles. WO2011040048A1, 2011.
59. Della Valle, R.; Bignozzi, C. A. Air decontamination equipment. US20110223057A1, 2011.
60. Fujimori, Y.; Nakayama, T.; Sato, T. Anti-viral agent. WO2010026730A1, 2010.
61. Reip, P. W. Antiviral composition comprising particles of a tungsten compound. WO 2009022100 A1 2009.

62. Bignozzi, C. A.; Dissette, V. Material, item and products comprising a composition having anti-microbial properties. US8389022B2, 2013.
63. Ren, G.; Oxford, J. S.; Reip, P. W.; Lambkin-Williams, R.; Mann, A. Virucidal materials comprising nanoparticles of metal and/or metal compounds. WO2007093808A2, 2007.
64. Sugiura, K. Antiviral agent containing an inorganic solid acid, a coating composition containing thereof, resin composition and an antiviral product. WO2017150063A1, 2017.
65. Hoffman, D. R.; Vanden Heuvel, A. L.; Anunson, P. N.; Kroll, L. M.; Paulsen, J. D.; Cunningham, C. T.; Koenig, D. W. Disinfectant composition with rapid antiviral efficacy. WO2017019010A1, 2017.
66. Krasnow, N. R.; Adams, L. L.; Cronin, J. P.; Reeser, R. J.; Agrawal, A.; Uhlmann, D. R. Compositions and preparation methods for antimicrobial metal nanoparticles. US20130315972A1, 2013.
67. Sarid, R. G., Aharon; Baram-Pinto, Dana Antiviral pharmaceuticals comprising water-soluble sulfonate-protected nanoparticles. US20120027809A1, 2012.
68. Wolfe, D. E. Up-conversion luminescent coatings/materials for antimicrobial applications. US20110171062A1, 2011.
69. Bignozzi, C. A.; Dissette, V.; Corallini, A.; Carra, G.; Della Valle, R. Functional nanomaterials with antibacterial and antiviral activity. US20080269186A1, 2012.
70. Holladay, R. J.; Moeller, W. D. Antiviral colloidal silver composition. WO2008147427A2, 2008.
71. Wang, J.; Yu, C.; Ma, F.; Zhao, X.; Tong, H. Coated metal heating element and its preparing method. CN103974469A, 2014.

72. Cheng, J.; Cheng, G. Antiviral disinfectant for killing avian influenza virus. CN104054753A, 2014.
73. Xu, X.; Yang, Z.; Zhang, Y.; Fan, L. Multifunctional wallpaper and coating composition for multifunctional wallpaper. CN105019312A, 2015.
74. Xu, S.; Li, Z.; Zhang, X. A preparation method of nano-antibacterial ceramic glaze layer. CN105152683A, 2015.
75. Guo, G. A kind of antivirus sheet. CN207594471U, 2018.
76. Szczepaniak, S.; Szczepaniak, R.; Szczepaniak, E.; Szczepaniak, D.; Szczepaniak, M.; Zalewska, A. Aqueous solutions of the citratoborate complexes of silver(I), copper(II) and zinc and a method for preparing thereof. PL223968B1, 2016.
77. Ascend files first FDA 510(k) submission based on Acteev™ technology - Ascend Performance Materials. <https://www.ascendmaterials.com/news/ascend-files-first-fda-510k-submission-based-on-acteev-technology> (accessed June 22, 2021).
78. Kronos advanced technologies files for provisional us patent protection for new antibacterial face mask with cellphone radiation protection features - GlobeNewswire. <https://www.globenewswire.com/en/news-release/2020/07/13/2061073/0/en/KRONOS-ADVANCED-TECHNOLOGIES-FILES-FOR-PROVISIONAL-US-PATENT-PROTECTION-FOR-NEW-ANTIBACTERIAL-FACE-MASK-WITH-CELLPHONE-RADIATION-PROTECTION-FEATURES.html> (accessed December 16, 2020).
79. Is the Copper Mask the New Gold Standard for Global Health? - Newsfile Corp. <https://www.newsfilecorp.com/release/86793/Is-the-Copper-Mask-the-New-Gold-Standard-for-Global-Health> (accessed June 22, 2021).

80. Researchers create air filter designed to trap and kill the coronavirus - University of Houston. <https://uh.edu/news-events/stories/july-2020/07142020ren-covid-filter.php> (accessed December 16, 2020).
81. Coating deactivates Covid-19 viruses on surfaces - Science & Enterprise. <https://sciencebusiness.technewslit.com/?p=39532> (accessed December 16, 2020).
82. Here come the sanitation booths: “A cloud that kills the Coronavirus” - The Patent. <https://www.thepatent.news/2020/05/11/sanitation-booths-coronavirus/> (accessed June 30, 2021).
83. Boeing licenses Ultraviolet Wand to Healthe, Inc. to counter Covid-19 - PR Newswire. <https://www.prnewswire.com/news-releases/boeing-licenses-ultraviolet-wand-to-healthe-inc-to-counter-covid-19-301135616.html> (accessed June 30, 2021).
84. Boeing and Far UV Technologies enter a licensing agreement for Ultraviolet Wand Technology - Associated Press. <https://apnews.com/article/virus-outbreak-technology-business-licensing-agreements-corporate-news-47b651be1e8b8d8b99c0e2635643a870> (accessed June 30, 2021).
85. Far-UVC Light Safely Kills Airborne Coronaviruses - Columbia University. <https://www.cuimc.columbia.edu/news/far-uv-light-safely-kills-airborne-coronaviruses> (accessed June 22, 2021).
86. Far UV launches new Krypton™ Disinfection Lighting Solutions - Far UV Technologies Inc. <https://faruv.com/far-uv-launches-new-krypton-disinfection-lighting-solutions/> (accessed June 30, 2021).
87. Irish company launches virus-killing robot for hospitals and public spaces - The Irish Times. <https://www.irishtimes.com/business/technology/irish-company-launches-virus-killing-robot-for-hospitals-and-public-spaces-1.4426507> (accessed June 30, 2021).

88. Kronos advanced technologies releases its newest Kronos® Air 5G® product line - GlobeNewswire. <https://www.globenewswire.com/en/news-release/2020/04/29/2024509/0/en/KRONOS-ADVANCED-TECHNOLOGIES-RELEASES-ITS-NEWEST-KRONOS-AIR-5G-PRODUCT-LINE.html> (accessed December 16, 2020).
89. Graphene protection against coronavirus: graphene-producing companies embarked on a warpath with COVID-19 - RUSGRAPHENE. <https://rusgraphene.com/graphene-protection-against-coronavirus> (accessed December 16, 2020).
90. Plasma jet wands could rapidly decontaminate hospital rooms - University of Michigan. <https://news.engin.umich.edu/2020/04/plasma-jet-wands-could-rapidly-decontaminate-hospital-rooms/> (accessed December 16, 2020).
91. Invention sparked by COVID-19 pandemic safely disinfects surfaces continuously - Princeton Plasma Physics Laboratory. <https://www.princeton.edu/news/2020/10/12/invention-sparked-covid-19-pandemic-safely-disinfects-surfaces-continuously> (accessed January 14, 2021).
92. BREATHE99 introduces superior respirator mask for Covid-19 crisis - Venn Foundation <https://www.vennfoundation.org/news/2020/4/15/press-release-breathe99-introduces-superior-respiratory-mask-for-covid-19-crisis> (accessed June 22, 2021).
93. Kepley BioSystems files accelerated patent for novel personal protection air sterilization device - Kepley BioSystems Inc. <https://kepleybiosystems.com/2020/06/18/patent-for-personal-protection-air-sterilization-device/> (accessed December 16, 2020).
94. US Army doctors invent COVID-19 isolation chamber to protect hospital staff - EurekAlert! https://eurekalert.org/pub_releases/2020-04/t-uad042120.php (accessed December 16, 2020).

95. UK researchers seek to develop antiviral membrane mask - University of Kentucky.
<https://uknow.uky.edu/research/uk-researchers-seek-develop-antiviral-membrane-mask>
(accessed January 14, 2021).
96. Face mask sensor detects Covid-19 virus - Science & Enterprise.
<https://sciencebusiness.technewslit.com/?p=41842> (accessed June 30, 2021).
97. Snood with germ trap technology fights COVID-19 - Innovation in Textiles.
<https://www.innovationintextiles.com/snood-with-germ-trap-technology-fights-covid19/>
(accessed January 14, 2021).
98. University of Toronto tests confirm first mask that deactivates coronavirus - PR Newswire.
<https://www.prnewswire.com/news-releases/university-of-toronto-tests-confirm-first-mask-that-deactivates-coronavirus-301092580.html> (accessed January 14, 2021).
99. LG revolutionizes personal clean air with Puricare™ Wearable Air Purifier - LG Newsroom.
<https://www.lgnewsroom.com/2020/08/lg-revolutionizes-personal-clean-air-with-puricare-wearable-air-purifier/> (accessed June 30, 2021).
100. SurfaceWise2 Becomes First Antiviral Surface Coating Approved by EPA to Continuously Protect Against COVID-19 With a Single Application - Allied BioScience.
<https://www.alliedbioscience.com/surfacewise2-approved-by-epa/> (accessed June 22, 2021).
101. Covalon announces new breakthrough antimicrobial technology formulated to kill the Covid-19 virus - Covalon Technologies.
<https://ir.covalon.com/press-releases?item=96> (accessed January 14, 2021).
102. Air purifier increases protection against viruses including COVID-19 - Fox43.
<https://www.fox43.com/article/news/local/air-purifier-peoplesbank-park-increases-protection-against-covid19/521-0d128aba-564d-489b-bef8-ddf4f5b9ad80> (accessed June 22, 2021).

103. LIGC Introduces ViralWall™: The Social Distancing Air Purifier Using Innovative Graphene Filters - WBOC. <https://www.w boc.com/story/43259249/ligc-introduces-viralwall-the-social-distancing-air-purifier-using-innovative-graphene-filters> (accessed June 22, 2021).
104. UArizona Invention May Help COVID-19 Patients Breathe Easier - University of Arizona. <https://news.arizona.edu/story/uarizona-invention-may-help-covid19-patients-breathe-easier> (accessed January 14, 2021).
105. Virgin orbit plans to mass-produce new medical breathing device to help fight coronavirus pandemic - The Verge. <https://www.theverge.com/2020/3/30/21199940/virgin-orbit-rocket-launch-satellites-breathing-medical-device-coronavirus-pandemic> (accessed December 16, 2020).
106. Welsh doctor uses military experience to design ventilator that will help coronavirus patients - WalesOnline. <https://www.walesonline.co.uk/news/health/welsh-doctor-uses-military-experience-17970315> (accessed December 16, 2020).
107. Designs for life-saving breathing aid to be made freely available - Mercedes-AMG Petronas Formula One Team. <https://www.mercedesamgf1.com/en/news/2020/04/ucl-uclh-f1-project-pitlane-start-delivery-breathing-aids-nhs-hospitals/> (accessed June 30, 2021).
108. Halberd Corporation Files for Patent Protection on Enhanced Nasal Spray to Prevent Covid-19 - BioSpace. <https://www.biospace.com/article/releases/halberd-corporation-files-for-patent-protection-on-enhanced-nasal-spray-to-prevent-covid-19/> (accessed June 22, 2021).
109. Scylla scanner: Spotted in a crowd - YU Observer. <https://yuobserver.org/2020/10/scylla-scanner-spotted-in-a-crowd/> (accessed January 14, 2021).
110. SINTX Technologies announces a fabric technology shown to inactivate upon contact SARS-CoV-2 - GlobeNewswire. <https://www.globenewswire.com/news->

[release/2021/03/09/2189626/30038/en/SINTX-Technologies-announces-a-fabric-technology-shown-to-inactivate-upon-contact-SARS-CoV-2-the-virus-causing-the-COVID-19-pandemic.html](https://www.sintx.com/news/2021/03/09/2189626/30038/en/SINTX-Technologies-announces-a-fabric-technology-shown-to-inactivate-upon-contact-SARS-CoV-2-the-virus-causing-the-COVID-19-pandemic.html) (accessed June 22, 2021).

111. ‘AeroNabs’ promise powerful, inhalable protection against COVID-19 - UCSF. <https://www.ucsf.edu/news/2020/08/418241/aeronabs-promise-powerful-inhalable-protection-against-covid-19> (accessed December 16, 2020).

112. Smartphone attachment to detect those infected with viruses, bacteria in minutes - Medgadget. <https://www.medgadget.com/2020/04/smartphone-attachment-to-detect-those-infected-with-viruses-bacteria-in-minutes.html> (accessed January 14, 2021).

113. Scheller, C.; Krebs, F.; Minkner, R.; Astner, I.; Gil-Moles, M.; Wätzig, H., Physicochemical properties of SARS-CoV-2 for drug targeting, virus inactivation and attenuation, vaccine formulation and quality control. *Electrophoresis* **2020**, *41* (13-14), 1137-1151.

114. Zaia, D. A. M., From spontaneous generation to prebiotic chemistry. *Quimica Nova* **2003**, *26* (2), 260-264.

115. Ruiz-Mirazo, K.; Briones, C.; de la Escosura, A., Prebiotic Systems Chemistry: New Perspectives for the Origins of Life. *Chemical Reviews (Washington, DC, United States)* **2014**, *114* (1), 285-366.

116. Patwa, T.; Li, C.; Simeone, D. M.; Lubman, D. M., Glycoprotein analysis using protein microarrays and mass spectrometry. *Mass spectrometry reviews* **2010**, *29* (5), 830-844.

117. Structure of SARS-CoV-2 spike glycoprotein. <https://www.rcsb.org/3d-view/6VXX> (accessed December 28, 2021).

118. Sehnal, D.; Bittrich, S.; Deshpande, M.; Svobodová, R.; Berka, K.; Bazgier, V.; Velankar, S.; Burley, S. K.; Koča, J.; Rose, A. S., Mol* Viewer: modern web app for 3D visualization and analysis of large biomolecular structures. *Nucleic Acids Research* **2021**, *49* (W1), W431-W437.
119. Formula of the 20 common amino acids and structural details of the side chains. http://www.imgt.org/IMGTeducation/Aide-memoire/_UK/aminoacids/formuleAA/ (accessed January 1, 2022).
120. Dramé, M.; Tabue Tegu, M.; Proye, E.; Hequet, F.; Hentzien, M.; Kanagaratnam, L.; Godaert, L., Should RT-PCR be considered a gold standard in the diagnosis of COVID-19? *Journal of medical virology* **2020**, *92* (11), 2312-2313.
121. Jawerth, N. How is the COVID-19 Virus Detected using Real Time RT-PCR? <https://www.iaea.org/newscenter/news/how-is-the-covid-19-virus-detected-using-real-time-rt-pcr> (accessed January 1, 2022).
122. Santos, M. C. D.; Morais, C. L. M.; Lima, K. M. G., ATR-FTIR spectroscopy for virus identification: A powerful alternative. *Biomedical Spectroscopy and Imaging* **2020**, *9*, 103-118.
123. Khan, R. S.; Rehman, I. U., Spectroscopy as a tool for detection and monitoring of Coronavirus (COVID-19). *Expert Review of Molecular Diagnostics* **2020**, *20* (7), 647-649.
124. Baker, M. J.; Trevisan, J.; Bassan, P.; Bhargava, R.; Butler, H. J.; Dorling, K. M.; Fielden, P. R.; Fogarty, S. W.; Fullwood, N. J.; Heys, K. A.; Hughes, C.; Lasch, P.; Martin-Hirsch, P. L.; Obinaju, B.; Sockalingum, G. D.; Sulé-Suso, J.; Strong, R. J.; Walsh, M. J.; Wood, B. R.; Gardner, P.; Martin, F. L., Using Fourier transform IR spectroscopy to analyze biological materials. *Nature Protocols* **2014**, *9* (8), 1771-1791.

125. Saadatkah, N.; Garcia, A. C.; Ackermann, S.; Leclerc, P.; Latifi, M.; Samih, S.; Patience, G. S.; Chaouki, J., Experimental methods in chemical engineering: Thermogravimetric analysis-TGA. *Canadian Journal of Chemical Engineering* **2020**, *98* (1), 34-43.
126. Menczel, J. D.; Prime, R. B., *Thermal analysis of polymers: fundamentals and applications*. John Wiley & Sons: 2009.
127. Brown, M. E., *Introduction to thermal analysis: techniques and applications*. Springer Science & Business Media: 2001; Vol. 1.
128. Darabi Mahboub, M. J.; Wright, J.; Boffito, D. C.; Dubois, J.-L.; Patience, G. S., Cs, V, Cu Keggin-type catalysts partially oxidize 2-methyl-1,3-propanediol to methacrylic acid. *Applied Catalysis A: General* **2018**, *554*, 105-116.
129. El-Sayed, S. A.; Mostafa, M. E., Pyrolysis characteristics and kinetic parameters determination of biomass fuel powders by differential thermal gravimetric analysis (TGA/DTG). *Energy Conversion and Management* **2014**, *85*, 165-172.
130. Skoog, D. A.; West, D. M.; Holler, F. J.; Crouch, S. R., *Fundamentals of analytical chemistry*. Cengage learning: 2013.
131. Griffiths, P. R., Introduction to the theory and instrumentation for vibrational spectroscopy. *Applications of Vibrational Spectroscopy in Food Science; Part One: Introduction and Basic Concepts* **2006**, 31-46.
132. Delgass, W.; Haller, G.; Kellerman, R.; Lunsford, J., Chapter 2: Infrared Spectroscopy. *Spectroscopy in Heterogeneous Catalysis* **1979**.
133. Stuart, B. H., *Infrared spectroscopy: fundamentals and applications*. John Wiley & Sons: 2004.

134. Smith, B. C., *Fundamentals of Fourier transform infrared spectroscopy*. CRC press: 2011.
135. Srinivasan, P. D.; Patil, B. S.; Zhu, H.; Bravo-Suárez, J. J., Application of modulation excitation-phase sensitive detection-DRIFTS for in situ/operando characterization of heterogeneous catalysts. *Reaction Chemistry & Engineering* **2019**, *4* (5), 862-883.
136. Noda, I.; Dowrey, A.; Marcott, C.; Story, G.; Ozaki, Y., Generalized two-dimensional correlation spectroscopy. *Applied Spectroscopy* **2000**, *54* (7), 236A-248A.
137. Noda, I., Two-Dimensional Infrared (2D IR) Spectroscopy: Theory and Applications. *Applied Spectroscopy* **1990**, *44* (4), 550-561.
138. Noda, I., Generalized two-dimensional correlation method applicable to infrared, Raman, and other types of spectroscopy. *Applied Spectroscopy* **1993**, *47* (9), 1329-1336.
139. Harrington, P. d. B.; Urbas, A.; Tandler, P. J., Two-dimensional correlation analysis. *Chemometrics and Intelligent Laboratory Systems* **2000**, *50* (2), 149-174.
140. Tandler, P. J.; Harrington, P. d. B.; Richardson, H., Effects of static spectrum removal and noise on 2D-correlation spectra of kinetic data. *Analytica Chimica Acta* **1998**, *368* (1), 45-57.

Chapter 2. Experimental

2.1 Introduction

Four amino acids that make up proteins were examined in this work. Decomposition of each amino acid in a 20% O₂-Ar mixture (simulating air) was studied on two catalyst surfaces: α -Al₂O₃ (~8 m²/g, 0.25-0.45 μ m, Alfa Aesar 42573) and Ag/ α -Al₂O₃ (30 wt. % Ag loading). The chosen amino acids were:

- Glycine (99%, Sigma-Aldrich G7126-100G)
- Alanine (98%, Lancaster 11187)
- Valine (98%, Sigma-Aldrich V0513-25G)
- Leucine (99%, Alfa Aesar A12311)

2.2. Preparation

2.2.1. Catalyst Preparation

2.2.1.1. α -Al₂O₃

α -Al₂O₃ (~8 m²/g, 0.25-0.45 micron, Alfa Aesar 42573) was purchased from Alfa Aesar. α -Al₂O₃ powder was taken in a crucible and placed in an oven (Heratherm, Thermo Scientific) at 150 °C and left to dry overnight; the powder was then stored in a 20 ml vial which was placed in an airtight resealable bag to minimize contact with moisture in the air.

2.2.1.2. Ag/ α -Al₂O₃

An Ag complex precursor was prepared following steps described in the literature.¹⁻⁵ Briefly, silver oxalate was prepared by mixing 0.4 M silver nitrate (AgNO₃, ACS, 99.9+% (metal basis), Alfa Aesar 11414) aqueous solution (HPLC, Fisher Chemical, P/N W5-4) and a 0.2 M

oxalic acid (Oxalic acid, 98%, anhydrous, Acros Organics, AC186432500) aqueous solution. The molar ratio of Ag nitrate to oxalic 1:2 was chosen such that the concentration of oxalate ions $C_2O_4^{2-}$ is four times that of Ag^+ ions to ensure complete consumption of the latter.^{6, 7} The $AgNO_3$ solution was added dropwise by a plastic pipette to $H_2C_2O_4$ solution (1 L beaker) under stirring using a magnetic stirrer (MS-H-Pro Plus hotplate-stirrer, Scilogex) at 60 °C for 20 min. The precipitate $Ag_2C_2O_4$ was filtered by vacuum filtration,⁸ using a 1 μm filter paper placed in a funnel on the top of a 2 L vacuum flask that was connected to a vacuum pump (Buchi V-700) by a rubber hose. Silver oxalate is highly insoluble in water; hence it was used to wash away excess ions and possible impurities. Deionized water (2 L beaker) was used for washing several times during vacuum filtration. Washing was stopped when the pH of the filtrate reached a pH of ~ 5 . The filtered $Ag_2C_2O_4$ was dried in a vacuum oven (Thermo Scientific, 3608-1CE) at 15 kPa and 60 °C overnight to avoid the risk of explosion of $Ag_2C_2O_4$. After that, the sample was stored at room temperature in amber vials (dark vial) to avoid decomposition by light exposure.^{6, 7}

Wet incipient impregnation of the dried $\alpha-Al_2O_3$ with a $Ag_2C_2O_4$ -DEA complex is carried out at room temperature. The impregnation solution is composed of $Ag_2C_2O_4$ dissolved in ethylenediamine (DEA) diluted with HPLC water with a fixed molar ratio of 1:4:16 moles ($Ag_2C_2O_4$:DEA: H_2O) for all prepared catalysts. In a typical preparation, a batch of impregnation solution, 3.9 g (4.3 ml) of DEA was added to 3.8 g (3.8 ml) of HPLC water in a 20 ml amber vial, after which 4 g of $Ag_2C_2O_4$ was added to the DEA-water solution and mixed by sonication for 10 min. The formed complex is stored at 4 °C in amber vials.^{6, 7}

Alpha-alumina ($\alpha-Al_2O_3$, SA $\sim 8 m^2/g$, 0.25-0.45-micron, 99.95% Alpha Aesar P/N 42573) powder was dried at 150 °C overnight in static air in a drying oven (Thermo Scientific, Heratherm

51028112). A specific pore volume of $0.17 \text{ cm}^3/\text{g}$ of $\alpha\text{-Al}_2\text{O}_3$ (close to BET value of $0.19 \text{ cm}^3/\text{g}$) was estimated by wet-incipient impregnation of a known amount of $\alpha\text{-Al}_2\text{O}_3$ with a water.

7.5 grams of dried $\alpha\text{-Al}_2\text{O}_3$ have a total pore volume of 1.125 ml. The corresponding required total weight of the impregnation solution is 5.04 g, equivalent to 74.2 ml, leading to several impregnation-vacuum cycles. In a cycle, an adjustable-volume pipette (adjustable-volume 20-200 μl , Fisherbrand FBE00200, Fisher Scientific) was used in which $\alpha\text{-Al}_2\text{O}_3$ was impregnated 12 times with the solution followed by thorough mixing, after which it was dried in a vacuum oven (Thermo Scientific, 3608-1CE) at 15 kPa and $60 \text{ }^\circ\text{C}$ for 6 h.^{2, 5} The previous steps were repeated for the second cycle. Additional details of the impregnation solution amount and number of cycles are shown in **Appendix A1**.

The vacuum dried $\alpha\text{-Al}_2\text{O}_3$ supported silver sample was then treated in a tube furnace instrument (Thermo Scientific, Thermolyne79300) in O_2 (UHP, Matheson) under flowing conditions at $250 \text{ }^\circ\text{C}$. Flow into tube furnace was adjusted using a rotameter so that a space velocity of $600 \text{ ml g}_{\text{cat}}^{-1} \text{ min}^{-1}$ is maintained. The sample was heated from ambient temperature to $110 \text{ }^\circ\text{C}$ ($5 \text{ }^\circ\text{C}/\text{min}$) and dwelled for 30 min, and then ramped to $250 \text{ }^\circ\text{C}$ ($5 \text{ }^\circ\text{C}/\text{min}$) and kept at that temperature for 2 h after which the sample was cooled down and stored before characterization.^{6, 7}

2.2.2. Amino Acid Samples Preparation

Amino acids were purchased from Sigma-Aldrich and Fisher Scientific and used as received. For each amino acid, 1-5 g of amino acid was first crushed into fine powder (sieved particle size between 38-75 μm) and added to HPLC water in a 100 ml beaker while being continuously stirred by a magnetic stirrer (MS7-H550-Pro, SCILOGEX) at 250 rpm to make 30

ml of homogenous aqueous solution of the acid at a concentration close to its solubility in water. The solubility data used was obtained from the PubChem database, a part of the National Library of Medicine (NLM) at the National Center for Biotechnology Information (NCBI) and is presented in **Appendix A2**.

Amino acids were then deposited onto the Al_2O_3 and $\text{Ag}/\alpha\text{-Al}_2\text{O}_3$ catalyst by a wet impregnation method. A volume of the precursor solution containing the amount of acid required to make a 20 wt.% sample on the supported material was collected in a 100 ml beaker and then placed on the heating/stirring plate (250 rpm). The catalyst was added to the stirring solution and was continued at 40 °C until most of the water evaporated (2-8 h depending on the initial volume of the solution); the solid obtained was then left overnight to dry further at ambient conditions (~21 °C, 30 % humidity). The sample was then crushed into a fine powder (sieved particle size between 38-75 μm) and stored in a 20 ml vial until further use. Details of the calculations are available in **Appendix A3**.

2.3. Characterization

2.3.1. Thermogravimetric Analysis (TGA)

TGA was carried out in a thermogravimetric analyzer (SDT Q600, TA Instruments) to find temperature ranges of decomposition of the samples in the presence of air and to perform kinetic analysis of sample decomposition. Crushed samples (sieved particle size between 38-75 μm) were placed in an alumina sample pan (pan size: 90 μl).

The sample cup was then placed in the TGA furnace and air (UHP, Matheson) flow was set to 80 cm^3/min . The temperature was then ramped at four different rates: 10, 7.5, 5, and 2.5 °C/min to 600 °C. The data collected at the various ramp rates was used to perform kinetic analysis, the details of the study and associated methods are mentioned in **Chapter 3**.

2.3.2. Ex Situ Fourier Transform Infrared Spectroscopy (FTIR)

Ex situ FTIR spectra for all samples were acquired using an FTIR spectrometer (VERTEX 70, Bruker). Samples were crushed into fine powder (sieved particle size between 38-75 μm) and placed in the Harrick micro sampling cup (3 mm diameter, adjustable 0.03 ml volume with funnel), which was then placed inside the Praying Mantis TM (Harrick) diffuse reflectance accessory. The spectra were then collected and averaged over 256 scans (4 cm^{-1}) with an aperture of 8 mm. OPUS spectroscopy software (Version 7.5, Bruker) was used to evaluate, process, and analyze the spectra.

2.4. In Situ FTIR Spectroscopy Experiment

Experiments were performed in a custom made in situ reaction cell.⁹ Finely crushed sample (~100 mg, sieved particle size between 38-75 μm) was loaded into the reaction cell and covered with a ZnSe dome with an O-ring in between them to prevent gas leaks as detailed elsewhere.⁹ The cell was then attached to the diffuse reflection accessory Praying Mantis TM (Harrick). Mass flow controllers (Omega) were used to regulate the flow of gases during the experiment.

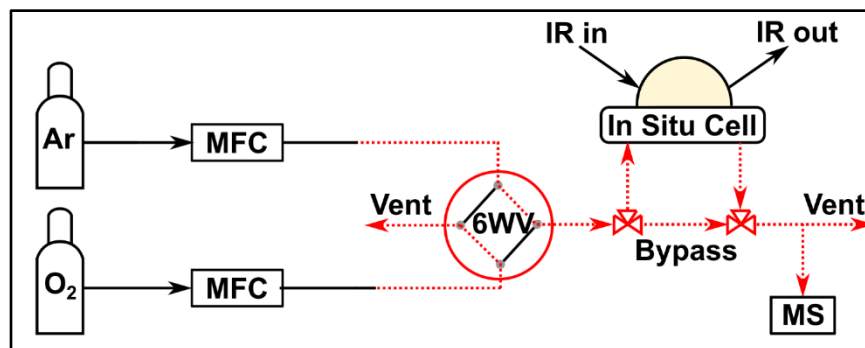


Figure 2.1 In situ FTIR experiment setup (MFC: Mass Flow Controller, 6WV: 6 Way Valve, IR: Infrared radiation)⁹

In an 80 cm^3/min flow of Argon (UHP, Matheson), the temperature was ramped at 10 $^\circ\text{C}/\text{min}$ (to 150 $^\circ\text{C}$ for AA/ Al_2O_3 samples and 80 $^\circ\text{C}$ for AA/Ag/ Al_2O_3 samples) and held for 30 min as a pretreatment to release any moisture present. After the pretreatment, the gas was

switched to an O₂/Ar mixture: 64 cm³/min of Argon and 16 cm³/min of Oxygen (UHP, Matheson) to make a 20% O₂-Ar mixture (resembling air) for the experiment. The flow rates were always changed in bypass mode (by passing the in situ cell) to avoid displacement of the powdered sample in the cell due to pressure fluctuations. The temperature was then ramped to 400 °C at a ramp rate of 10 °C/min while IR spectra were simultaneously collected for the duration of the ramping using a rapid-scan method, which collected spectra approximately every 3.9 seconds (64 scans, 4 cm⁻¹). Mass spectrometer was also used to detect gases exiting the reactor.

The rapid-scan spectra were then analyzed by Two-Dimensional Correlation (2D-COS); the synchronous and asynchronous plots were evaluated using the 2D-COS evaluation method available in Bruker's OPUS software (Version 7.5). As described earlier (**Chapter 1**), the synchronous plot gives information about changes that take place in phase or synchronously (at the same time). The peaks along the diagonal, called auto-peaks, show correlation of each element with itself (as wavenumbers on both *x* and *y* axis are equal in the 2D-COS in IR). Peaks occurring away from the diagonal are called cross-peaks and represent the correlation of different elements with one another. The cross-peaks in a synchronous plot are symmetric about the diagonal. While the intensities of the auto-peaks are always positive, those of the cross-peaks can be either positive or negative; while positive cross-peaks occur if both elements increase or decrease together, negative cross-peaks arise when one element increases while the other decreases.^{10, 11}

The asynchronous plot displays behavior that occurs out of phase. As an element cannot be correlated out of phase with itself, the asynchronous spectrum does not show auto-peaks along the diagonal. The cross-peaks here are antisymmetric about the diagonal. The temporal

information present in the asynchronous plot can be interpreted in tandem with the synchronous spectrum; for a particular point (x, y), positive peaks in both the synchronous and asynchronous plot imply that the element represented by the x coordinate leads the change in the element represented by the y coordinate. If the synchronous plot has a positive peak while the asynchronous plot has a negative one, the element corresponding to the x coordinate lags the one corresponding to the y coordinate. For the scenario where the synchronous plot shows a negative peak, the interpretation of the asynchronous spectrum is reversed. Both synchronous and asynchronous plot are instrumental to gather the most information possible about a system, the correlation between two elements (e.g., two wavenumbers), their level of synchronization, and relative dynamic changes, which are useful in studying chemical reactions occurring on catalysts surfaces such as those described in this thesis.^{10, 11}

2.5. References

1. Kemp, R. A. Process for Preparing Ethylene Oxide Catalysts. US5364826A, 1993.
2. van den Reijen, J. E.; Kanungo, S.; Welling, T. A. J.; Versluijs-Helder, M.; Nijhuis, T. A.; de Jong, K. P.; de Jongh, P. E., Preparation and particle size effects of Ag/ α -Al₂O₃ catalysts for ethylene epoxidation. *Journal of Catalysis* **2017**, *356*, 65-74.
3. Amin In *Bimetallic Cu-Ag and Au-Ag catalyst for ethylene epoxidation reaction Graduation Project (6CPT00)*, 2018.
4. Pinaeva, L.; Noskov, A., Prospects for the Development of Ethylene Oxide Production Catalysts and Processes (Review). *Petroleum Chemistry* **2020**, *60*, 1191-1206.
5. Zope, K. R.; Cormier, D.; Williams, S. A., Reactive Silver Oxalate Ink Composition with Enhanced Curing Conditions for Flexible Substrates. *ACS Applied Materials & Interfaces* **2018**, *10* (4), 3830-3837.

6. Boldyrev, V. V., Thermal decomposition of silver oxalate. *Thermochimica Acta* **2002**, 388 (1), 63-90.
7. Pourmortazavi, S. M.; Hajimirsadeghi, S. S.; Kohsari, I.; Fareghi Alamdari, R.; Rahimi-Nasrabadi, M., Determination of the optimal conditions for synthesis of silver oxalate nanorods. *Chemical Engineering & Technology: Industrial Chemistry-Plant Equipment-Process Engineering-Biotechnology* **2008**, 31 (10), 1532-1535.
8. Yang, W.; Wang, C.; Arrighi, V., Preparation and characterization of organic silver precursors for conductive ink. *International Journal of Electronics and Communication Engineering* **2018**, 12 (9), 670-677.
9. Patil, B. S.; Srinivasan, P. D.; Atchison, E.; Zhu, H.; Bravo-Suárez, J. J., Design, modelling, and application of a low void-volume in situ diffuse reflectance spectroscopic reaction cell for transient catalytic studies. *Reaction Chemistry & Engineering* **2019**, 4 (4), 667-678.
10. Harrington, P. d. B.; Urbas, A.; Tandler, P. J., Two-dimensional correlation analysis. *Chemometrics and Intelligent Laboratory Systems* **2000**, 50 (2), 149-174.
11. Tandler, P. J.; Harrington, P. d. B.; Richardson, H., Effects of static spectrum removal and noise on 2D-correlation spectra of kinetic data. *Analytica Chimica Acta* **1998**, 368 (1), 45-57.

Chapter 3. Thermogravimetric Analysis and Kinetic Study of Amino Acids on α -Alumina and α -Alumina supported Silver Catalyst in Oxygen Atmosphere

3.1. Introduction

Thermogravimetric Analysis (TGA) of the admixtures of amino acids glycine, alanine, valine, and leucine with α -Al₂O₃ and α -Al₂O₃ supported Ag catalyst, Ag(30%)/ α -Al₂O₃, was carried out to determine their decomposition temperature ranges. A kinetic study of the TGA results was also performed to obtain parameters such as apparent activation energy and pre-exponential factor, to gain a better and more complete understanding of the reaction and possible catalysis involved. While there are numerous methods of analyzing non-isothermal solid-state kinetic data acquired from TGA,^{1,2} iso-conversional methods are most often used as they allow a simple and accurate determination of apparent activation energy values without the assumption of a reaction model, relying instead on TGA data collected at different heating rates based on the principle that the reaction model at a given extent of conversion depends only on the temperature.³

3.2. Kinetic Theory

We first start by defining a conversion fraction for the reaction, α , as:

$$\alpha = \frac{m_i - m_a}{m_i - m_f} \quad (1)$$

Where m_i , m_a and m_f are the initial, actual and final masses of the sample respectively, the rate of conversion as a function of temperature can be represented by:

$$\frac{d\alpha}{dt} = k(T) f(\alpha) \quad (2)$$

Where k denotes the reaction constant, and $f(\alpha)$ the reaction model. Using the Arrhenius equation

to express the rate constant, we have:

$$k = A e^{\frac{-E_a}{RT}} \quad (3)$$

where A is the apparent pre-exponential factor, E_a the apparent activation energy (kJ mol^{-1}), R the universal gas constant ($8.314 \text{ J mol}^{-1} \text{ K}^{-1}$) and T the absolute temperature (K). Combining Equations (2) and (3), we get:

$$\frac{d\alpha}{dt} = A f(\alpha) e^{\frac{-E_a}{RT}} \quad (4)$$

Now, the temperature during the TGA run is dependent on time and heating or ramp rate β as given by:

$$T = T_o + \beta t \quad (5)$$

The time derivative in Equation (4) can now be converted to a temperature derivative, yielding:

$$\frac{d\alpha}{dt} = \frac{A}{\beta} f(\alpha) e^{\frac{-E_a}{RT}} \quad (6)$$

Rearranging by separating variables and integrating, we get:

$$\int_0^\alpha \frac{d\alpha}{f(\alpha)} = g(\alpha) = \int_{T_0}^T \frac{A}{\beta} e^{\frac{-E_a}{RT}} \quad (7)$$

3.3. Methods

As the integral in Equation (7) does not have an analytical solution, approximations such as that by Doyle and Serum and Yang have been largely used in the literature for solid-state reaction kinetic analysis; the corresponding solutions lead to the most widely used models in literature, namely, the Flynn-Wall-Ozawa method and the Kissinger-Akahira-Sunose method, which are utilized in this work.³

3.3.1. Flynn-Wall-Ozawa (FWO) Method

One of the first iso-conversional methods, the FWO method implements the Doyle approximation to the integral in Equation (7), resulting in the equation:

$$\ln(\beta_i) = \ln\left(\frac{A_\alpha E_\alpha}{Rg(\alpha)}\right) - 5.331 - 1.052 \frac{E_\alpha}{RT_{\alpha i}} \quad (8)$$

Where subscripts i and α refer to the heating rate and given conversion respectively. Plotting $\ln(\beta_i)$ vs. $1/T$ data for a given conversion value and fitting to a linear graph, the apparent activation energy can be obtained from the slope $-1.052 E_\alpha/R$.

3.3.2. Kissinger-Akahira-Sunose (KAS) Method

The KAS method improves accuracy for the value of apparent activation energy using the equation:

$$\ln\left(\frac{\beta_i}{T_{\alpha i}^2}\right) = \ln\left(\frac{A_\alpha R}{E_\alpha g(\alpha)}\right) - \frac{E_\alpha}{RT_{\alpha i}} \quad (9)$$

In this method, a plot of $\ln(\beta_i/T^2)$ vs. $1/T$ fitted to a linear graph is used to obtain the apparent activation energy from the slope $-E_\alpha/R$.

3.4. Results and Discussion

3.4.1. TGA

Weight loss (TGA) and differential weight (DTG) thermograms for the amino acid admixtures (AA/ α -Al₂O₃ and AA/Ag/ α -Al₂O₃) along with the corresponding amino acid structures⁴ at four different heating rates (2.5, 5, 7.5 and 10 °C min⁻¹) in air are shown in this section. Expected overall reactions for complete amino acid conversion in air to decomposition products are also included; It has been reported in the literature that amino acids will eventually decompose into water, carbon dioxide and water.⁵⁻⁷

The TGA results for glycine on Al₂O₃ and Ag/ α -Al₂O₃ are presented in **Figure 3.1**. This figure shows that the decomposition of this amino acid on alumina started to take place at ~220 °C as indicated from the derivative of the weight vs temperature plot. This temperature reduced to ~120 °C in the case of Ag/ α -Al₂O₃ catalyst. In comparison, the temperature for pure glycine has been reported to be ~230-250 °C which is in line with Al₂O₃ admixture results.^{6,8} The overall

reaction for complete oxidation can be shown by:

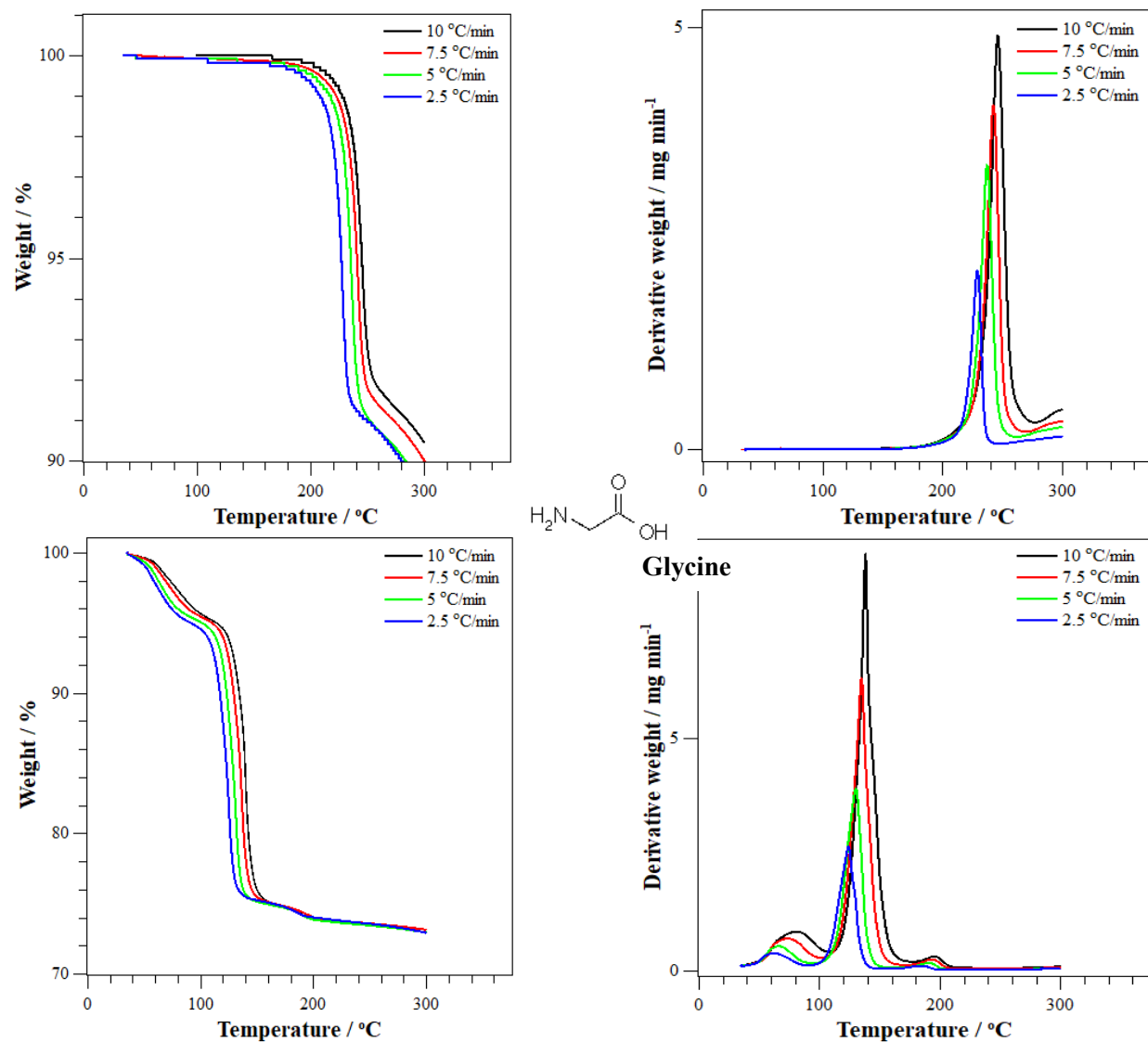
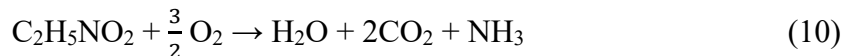


Figure 3.1. Results for Glycine/ Al_2O_3 TGA (top-left) and DTG (top-right), structure (middle), and Glycine/ $\text{Ag}/\text{Al}_2\text{O}_3$ TGA (bottom-left) and DTG (bottom-right).

In the case of alanine, an amino acid which resembles glycine but with an additional methyl group sharing the carbon with the ammine group (**Figure 3.2**), the weight loss began at ~ 190 °C on alumina, whereas in the case of $\text{Ag}/\alpha\text{-Al}_2\text{O}_3$ catalyst it further reduced to ~ 120 °C, which showed a similar behavior as for glycine. For pure alanine, the decomposition temperature

has been reported to be ~ 225 °C, which is also in agreement with the AA/ α -Al₂O₃ admixture.^{8,9}

Also, the overall complete oxidation reaction can be shown as:

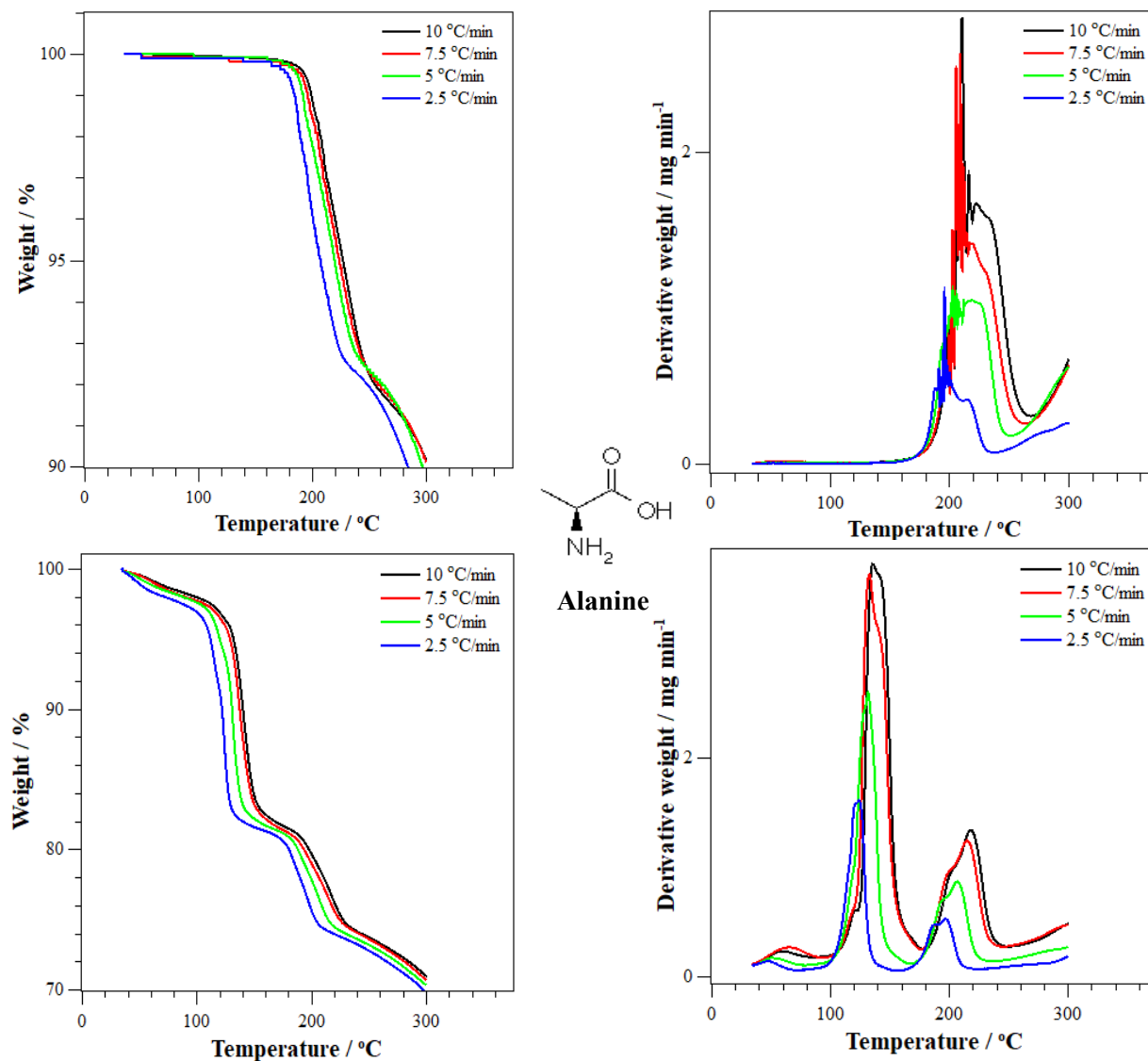
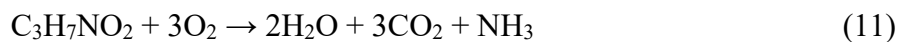


Figure 3.2. Results for Alanine/Al₂O₃ TGA (top-left) and DTG (top-right), structure (middle), and Alanine/Ag/Al₂O₃ TGA (bottom-left) and DTG (bottom-right).

Figure 3.3 shows the decomposition of valine, an amino acid which resembles alanine but with an isopropyl instead of a methyl group sharing the ammine carbon in the glycine structure. The figure shows that the decomposition of this amino acid started at ~ 220 °C on α -

Al₂O₃ and began at ~125 °C on the Ag/α-Al₂O₃ catalyst. The decomposition temperature reported for valine is ~220 °C which is also in line with the results for the α-Al₂O₃ admixture.⁹

The reaction overall oxidation reaction is given by:

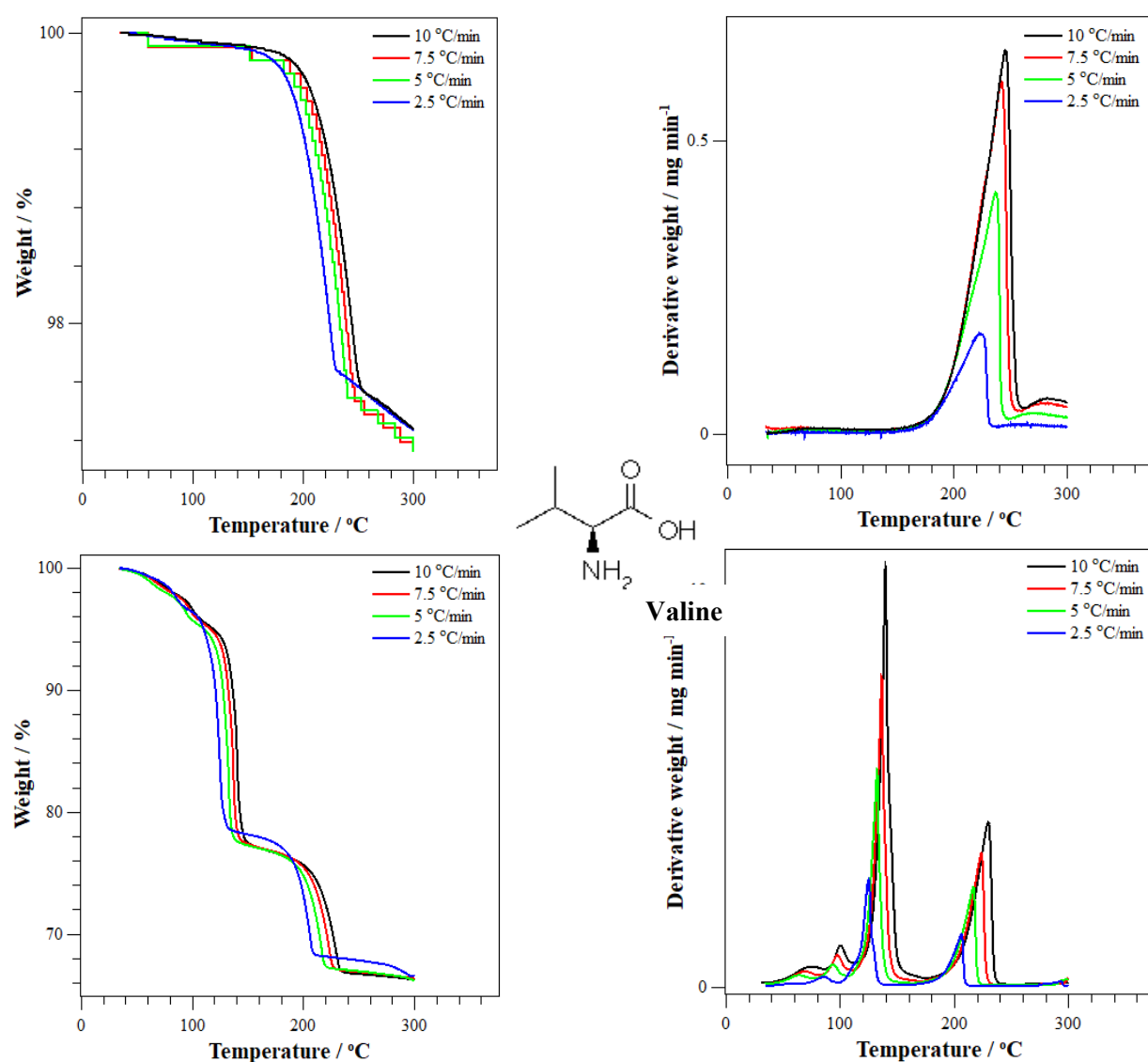
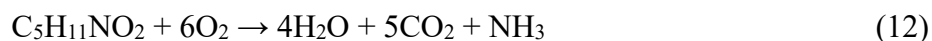


Figure 3.3. Results for Valine/Al₂O₃ TGA (top-left) and DTG (top-right), structure (middle), and Valine/Ag/Al₂O₃ TGA (bottom-left) and DTG (bottom-right).

Lastly, the TGA results for leucine, an alanine analog, except that the extra group attached to the ammine carbon is an isobutyl instead of a methyl group (**Figure 3.4**). The results show that on α-Al₂O₃ the beginning of the decomposition was at ~210 °C, while that on Ag/α-

Al₂O₃ catalyst was began at ~120 °C. These results follow the same trends for the simple amino acids. Additionally, pure leucine starts to decompose at ~240 °C, which is in the same range for the AA/ α -Al₂O₃ admixture.^{7, 10} Similarly, the overall leucine decomposition reaction is given by:

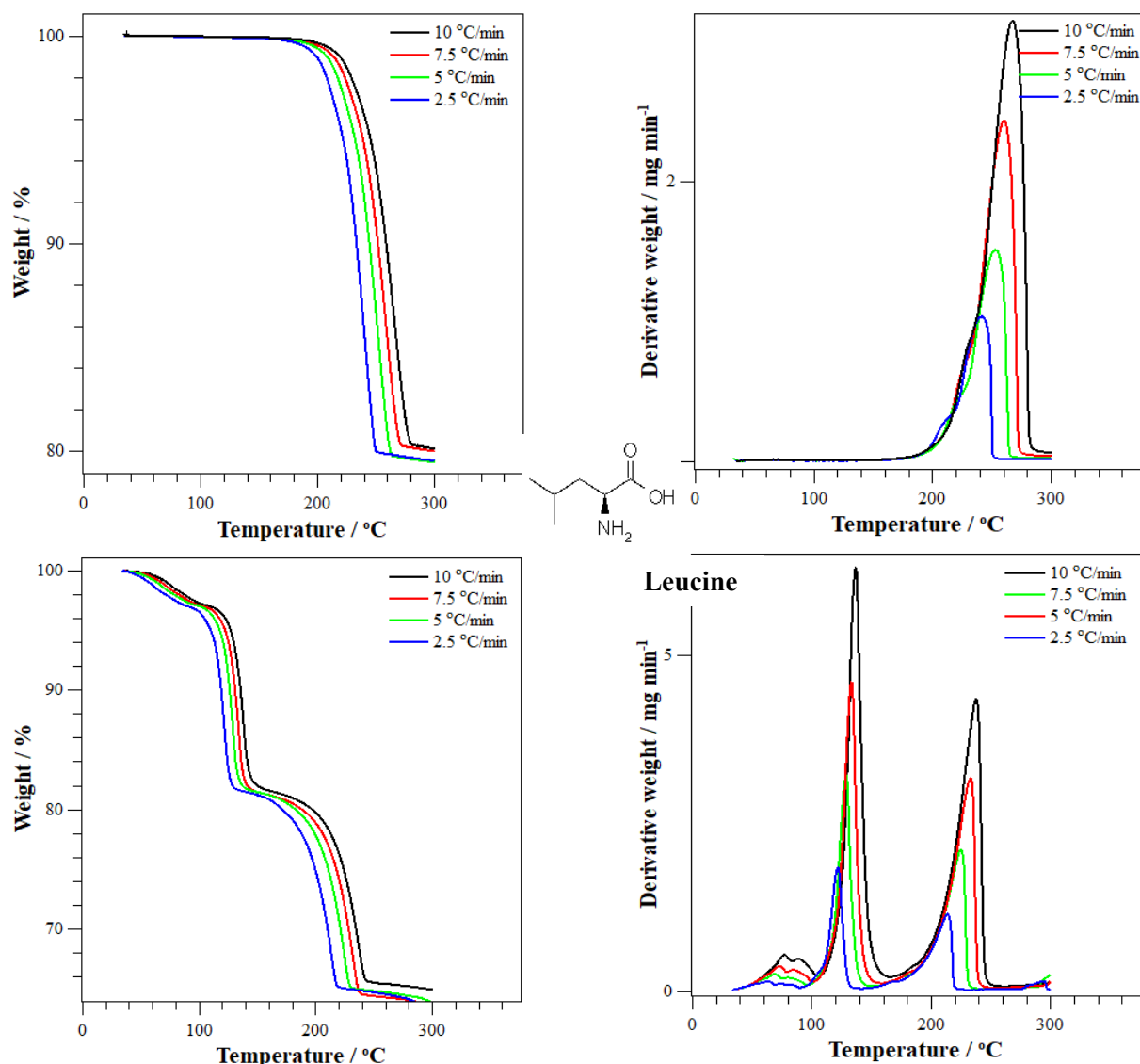
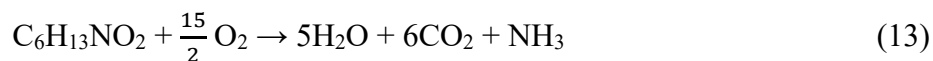


Figure 3.4 Results for Leucine/Al₂O₃ TGA (top-left) and DTG (top-right), structure (middle), and Leucine/Ag/Al₂O₃ TGA (bottom-left) and DTG (bottom-right).

In summary, the decomposition of the glycine, alanine, valine, and leucine amino acids

series in the presence of air took place between $\sim 200\text{-}220$ °C on the $\alpha\text{-Al}_2\text{O}_3$ and $\sim 120\text{-}135$ °C on the Ag/ $\alpha\text{-Al}_2\text{O}_3$. There was not a general trend that could be derived from the structure of the amino acids, but for the most part the order of decomposition tracked for both the support and the Ag catalyst. The initial decrease in weight can be attributed to the loss of adsorbed water from the alumina.⁹ While glycine, valine and leucine show a single TGA peak on the $\alpha\text{-Al}_2\text{O}_3$ (rapid weight loss) indicating considerable decomposition around a particular temperature, alanine and leucine on the Ag/ $\alpha\text{-Al}_2\text{O}_3$ show multiple peaks implying the involvement of the silver catalyst in the decomposition of the amino acid and its surface hydrocarbon fragments via various pathways and at different temperatures.⁸⁻¹⁰ The decomposition process of amino acids via different stages may involve reactions such as dehydration, decarboxylation and deamination.⁹⁻¹² The peaks associated with these different stages will likely overlap as a result of multiple reactions resulting from the action of the silver catalyst. Clearly, the presence of multiple peaks for the amino acids is indicative of distinct temperature regions for different stages associated with different reactions and which is more evident on the Ag/ $\alpha\text{-Al}_2\text{O}_3$.^{9, 10}

In terms of weight loss (or conversion) during amino acid decomposition, the TGA results up to a temperature of 300 °C presented a range of decomposition of up to $\sim 5\text{-}20\%$ of the initial weight when impregnated on $\alpha\text{-Al}_2\text{O}_3$. Notably, the average overall amino acid conversion increased to $\sim 25\text{-}35\%$ in the presence of Ag/ Al_2O_3 , indicating the involvement of the silver catalyst in additional catalyzed oxidation reactions in agreement with a reduction in the decomposition temperatures discussed above when the silver catalyst was present.

3.4.2. Kinetic analysis

The results of the thermogravimetric analysis were processed using the iso-conversional methods of FWO and KAS. The respective $\ln(\beta_i)$ vs. $1/T$ and $\ln(\beta_i/T^2)$ vs. $1/T$ plots at different

conversions are shown here (**Figures 3.5** and **3.6**) and in the Appendix section. To exclude the region of moisture dehydration and to avoid inaccuracies due to DTG peak tails, component conversions in the range of 0.3-0.5 (at intervals of 0.05) were used for both methods.^{13, 14} As an example of the methods, **Figures 3.5** and **3.6** show the application of FWO and KAS methods for Glycine/ α -Al₂O₃ and Glycine/Ag/ α -Al₂O₃ TGA results. The figures show similar qualitative trends and negative slopes for both methods, but with smaller slope values for when the catalyst was used. Similar trends are also observed for other amino acids and they are summarized in the **Appendix**.

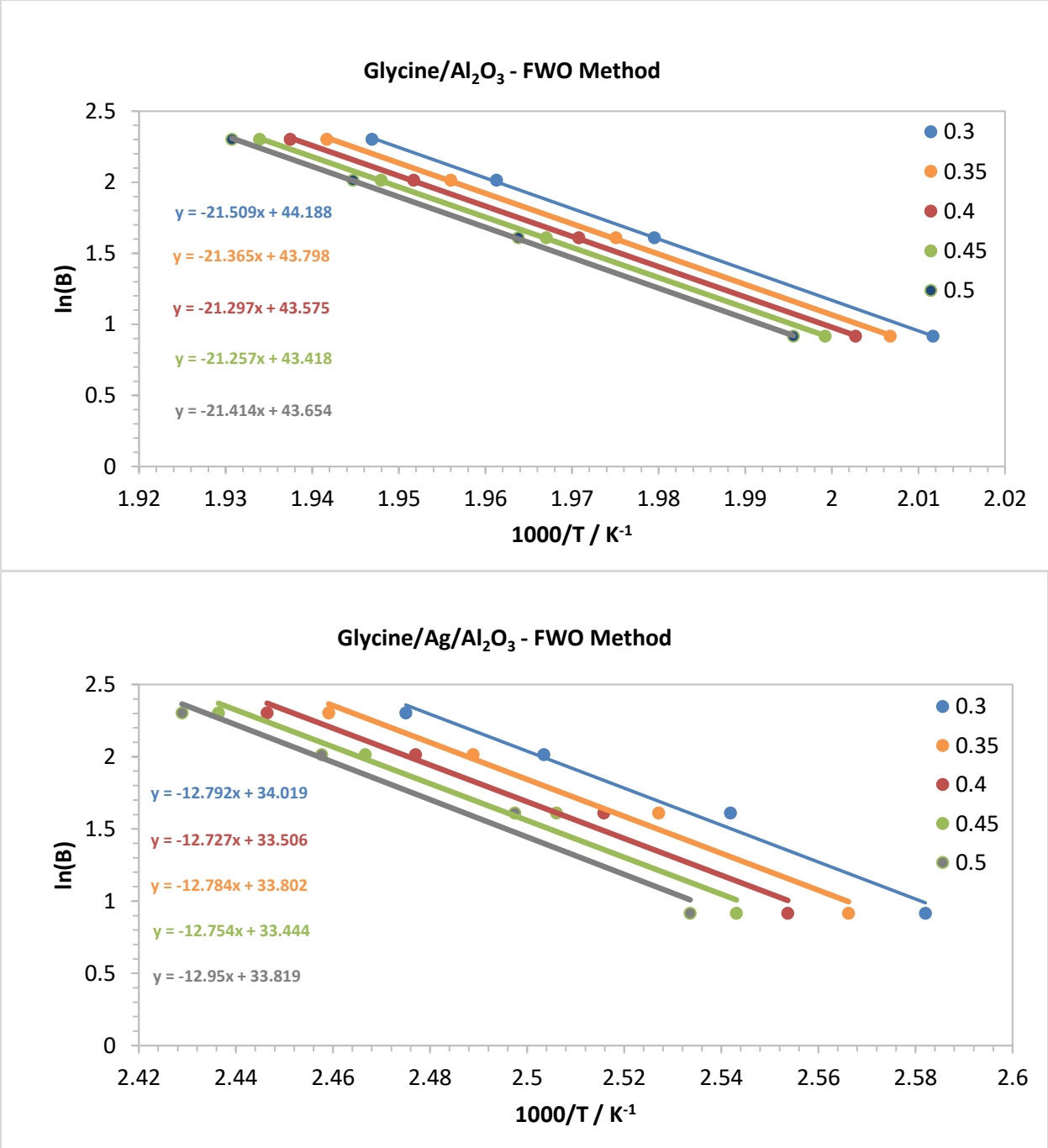


Figure 3.5. TGA kinetic analysis for Glycine/Al₂O₃ (top) and Glycine/Ag/Al₂O₃ (bottom): FWO method

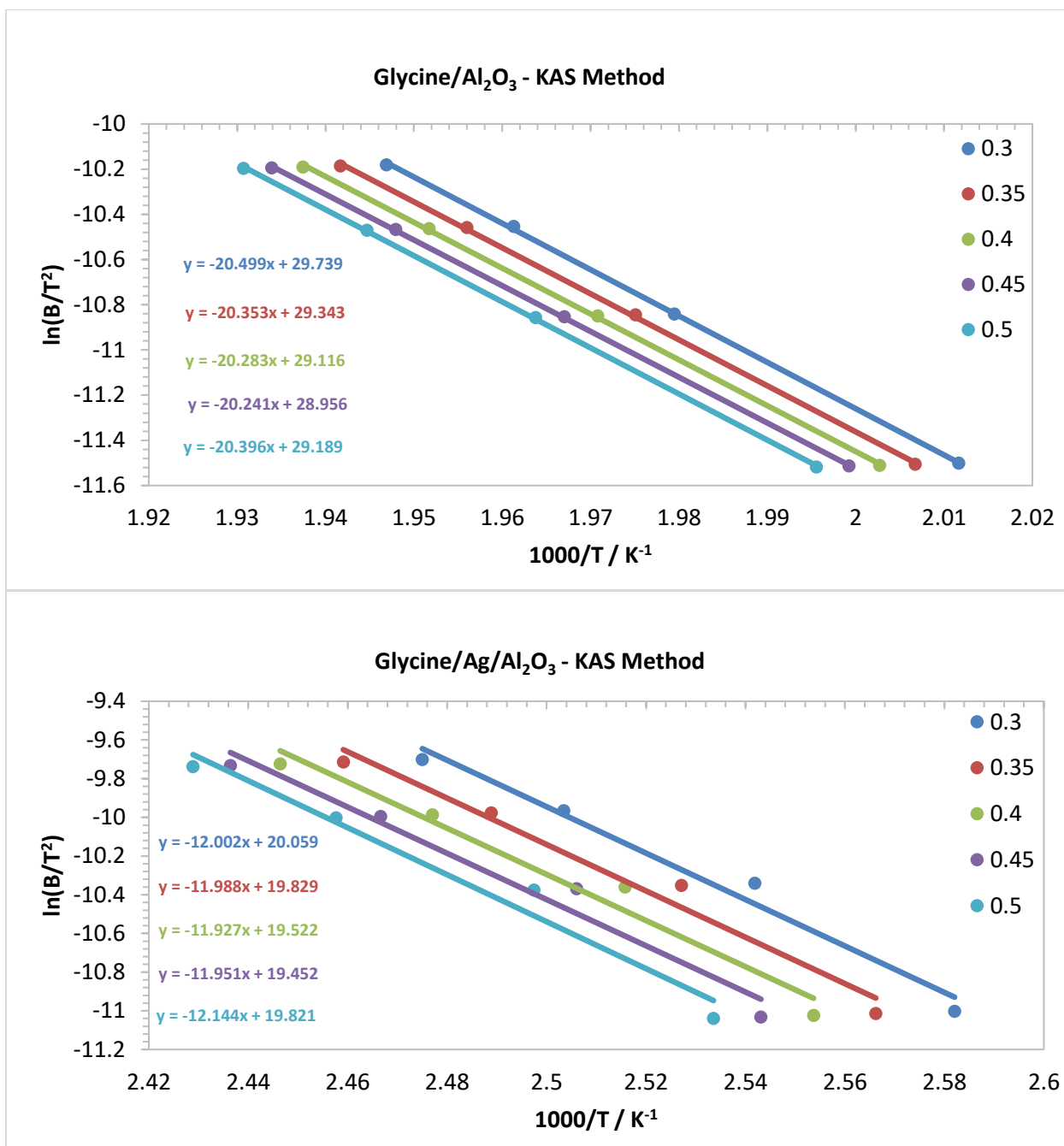


Figure 3.6. TGA kinetic analysis for Glycine/Al₂O₃ (top) and Glycine/Ag/Al₂O₃ (bottom): KAS method

Tables 3.1 and 3.2 summarize the results of apparent activation energies and pre-exponential factors as derived from FWO and KAS methods. The activation energies calculated are considered to be apparent activation energies as they average the different decomposition

stages taking place. However, these values are appreciably accurate as they take into account data collected over different heating rates as compared to methods relying on results arising from experiments run on a single heating rate.

It is clear from the results in **Tables 3.1** and **3.2** that both kinetic parameters are similar within experimental error regardless of the method applied. For example, the apparent activation energies calculated are 168.75 (FWO) and 101.17 (FWO) kJ mol^{-1} for glycine/ Al_2O_3 , and glycine/ $\text{Ag}/\text{Al}_2\text{O}_3$, respectively. When compared with the reported activation energy for glycine decomposition of $\sim 160 \text{ kJ mol}^{-1}$,^{15, 16} the similarity in apparent activation energies indicate that glycine on Al_2O_3 is likely to form admixtures rather than a highly dispersed material as expected from the low pore volume for this support. More importantly, the effect of the presence of the catalyst is clearly reflected in the significant reduction in apparent activation energy, which is also in agreement with the higher conversion and reduction in decomposition temperature. For the case of alanine/ Al_2O_3 and alanine/ $\text{Ag}/\text{Al}_2\text{O}_3$, the corresponding apparent activation energies were 168.82 and 93.00 kJ mol^{-1} , which when compared with that reported for pure alanine decomposition of $\sim 170 \text{ kJ mol}^{-1}$,^{16, 17} also confirm the active role of the catalyst and inertness of the alumina support for oxidation reactions. In the case of valine ($E_a \sim 150 \text{ kJ mol}^{-1}$)¹⁶ and leucine ($E_a \sim 130 \text{ kJ mol}^{-1}$)¹⁶ similar observations were noted. From this kinetic analysis, we see that the determined activation energy values for the amino acids on $\alpha\text{-Al}_2\text{O}_3$ are close to the actual activation energy values of single amino acid decomposition as reported in the literature. Further, on the $\alpha\text{-Al}_2\text{O}_3$ supported Ag, a significant decrease in the activation energy is observed for all amino acids, suggesting possible catalytic activity. The pre-exponential factors calculated (assuming a solid-state first order reaction)¹⁸ mostly remain constant in magnitude throughout the reaction and vary between $\sim 10^{14}$ - 10^{25} for FWO method and between 10^8 - 10^{19} for KAS

method. These results suggest that the KAS method may be more appropriate for TGA estimations of kinetic parameters as the pre-exponential factors are closer within the range expected for unimolecular reactions based on transition state theory.²

Table 3.1. Summary of calculated activation energy and pre-exponential factors during thermal decomposition of AA/ α -Al₂O₃ in oxygen

	FWO				KAS				Rep.
	E _a (kJ mol ⁻¹)	Std. dev.	A (min ⁻¹)	Std. dev.	E _a (kJ mol ⁻¹)	Std. dev.	A (min ⁻¹)	Std. dev.	E _a (kJ mol ⁻¹)
Glycine/ α -Al ₂ O ₃	168.63	0.84	5.1E+19	8.9E+18	169.23	0.84	5.3E+13	1E+13	160 ^{15, 16}
Alanine/ α -Al ₂ O ₃	169.82	7.36	1.4E+21	2.5E+21	170.59	7.68	1.9E+15	3.4E15	170 ^{16, 17}
Valine/ α -Al ₂ O ₃	140.55	1.74	1.7E+17	6.9E+16	139.64	1.78	1.3E+11	5.7E+10	150 ¹⁶
Leucine/ α -Al ₂ O ₃	122.55	1.75	4.6E+14	1.7E+14	120.35	1.90	2.4E+08	1E+08	130 ¹⁶

Table 3.2. Summary of calculated activation energy and pre-exponential factors during thermal decomposition of AA/Ag/ α -Al₂O₃ in oxygen

	FWO				KAS				Rep.
	E _a (kJ mol ⁻¹)	Std. dev.	A (min ⁻¹)	Std. dev.	E _a (kJ mol ⁻¹)	Std. dev.	A (min ⁻¹)	Std. dev.	E _a (kJ mol ⁻¹)
Glycine/Ag/ α -Al ₂ O ₃	101.17	0.69	3.9E+15	1E+15	99.79	0.71	2.3E+9	6.30E+8	160 ^{15, 16}
Alanine/Ag/ α -Al ₂ O ₃	93.00	7.36	2.8E+14	2.4E+14	91.09	4.51	1.3E+08	1.30E+8	170 ^{16, 17}
Valine/Ag/ α -Al ₂ O ₃	113.93	1.93	1.4E+17	1.2E+17	113.13	2.01	1.1E+11	9.3E+10	150 ¹⁶
Leucine/Ag/ α -Al ₂ O ₃	113.20	3.32	3.1E+25	6.9E+25	112.28	3.31	2.4E+19	5.3E+19	130 ¹⁶

Overall, the TGA results gave insights into the stability of the amino acids series of glycine, alanine, valine, and leucine. The high decomposition temperatures of amino acids can be attributed to the intramolecular hydrogen bonding between the carboxyl and amine groups; the decomposition of the amino acids involved has been proposed to follow pathways where decarboxylation is the first stage.^{19, 20} The sidechains are thus responsible for the differences in their thermal behavior due to the formation of intermediates of varying thermal stability after the

initial bond cleavage.²⁰ For the alumina supported amino acids, activation energies were found to decrease in the order of: glycine ~ alanine > valine > leucine. Considering that R-CH⁺-NH₂ may form after decarboxylation of the amino acid, one would expect the amino acids to be more stable when the substituted group R is larger and more branched (glycine (R=H) < alanine (R=methyl) < valine (R= isopropyl) < leucine (R=isobutyl)) due to the greater inductive effect; however, the apparent activation energy order is opposite, indicating that the decomposition of this amino acid series may not go through an initial decarboxylation step or that is kinetically, not thermodynamically controlled. In the presence of a silver catalyst, the apparent activation energies did not follow a particular trend but were closer in values and in the range of 93-113 kJ mol⁻¹. These variations with respect to those on alumina suggest differences to the mechanisms involved and a more complex dependence with the silver catalyst which is probably associated with the variety of oxidation reactions catalyzed by silver but which are more likely to be similar for the studied amino acid analog series.

While the above results show that amino acids decompose at lower temperature ranges on the silver/alumina catalyst compared to alumina along with a reduction in the apparent activation energies, it does not provide information on the nature of the molecular interactions and reaction conversion pathways. These questions will be addressed by in situ spectroscopic characterization via DRIFTS/2D-COS and MS as described in the next chapter.

3.5. References

1. Chong, C. T.; Mong, G. R.; Ng, J.-H.; Chong, W. W. F.; Ani, F. N.; Lam, S. S.; Ong, H. C., Pyrolysis characteristics and kinetic studies of horse manure using thermogravimetric analysis. *Energy Conversion and Management* **2019**, *180*, 1260-1267.

2. Chen, Z.; Zhu, Q.; Wang, X.; Xiao, B.; Liu, S., Pyrolysis behaviors and kinetic studies on Eucalyptus residues using thermogravimetric analysis. *Energy Conversion and Management* **2015**, *105*, 251-259.
3. Trache, D.; Abdelaziz, A.; Siouani, B., A simple and linear isoconversional method to determine the pre-exponential factors and the mathematical reaction mechanism functions. *Journal of Thermal Analysis and Calorimetry* **2017**, *128*, 335+.
4. Formula of the 20 common amino acids and structural details of the side chains. http://www.imgt.org/IMGTEducation/Aide-memoire/_UK/aminoacids/formuleAA/ (accessed January 1, 2022).
5. Yablokov, V. Y.; Smel'tsova, I.; Zelyaev, I.; Mitrofanova, S., Studies of the rates of thermal decomposition of glycine, alanine, and serine. *Russian Journal of General Chemistry* **2009**, *79* (8), 1704-1706.
6. Weiss, I. M.; Muth, C.; Drumm, R.; Kirchner, H. O. K., Thermal decomposition of the amino acids glycine, cysteine, aspartic acid, asparagine, glutamic acid, glutamine, arginine and histidine. *Bmc Biophysics* **2018**, *11* (1), 2.
7. Lien, Y.; Nawar, W., Thermal decomposition of some amino acids. Valine, leucine and Isoleucine. *Journal of Food Science* **1974**, *39* (5), 911-913.
8. Olafsson, P. G.; Brynn, A. M., Evaluation of thermal decomposition temperatures of amino acids by differential enthalpic analysis. *Mikrochimica acta* **1970**, (5), 871-8.
9. Bujdak, J.; Rode, B. M., Peptide bond formation on the surface of activated alumina: peptide chain elongation. *Catalysis Letters* **2003**, *91* (3-4), 149-154.
10. Rodante, F.; Marrosu, G., THERMAL-ANALYSIS OF SOME ALPHA-AMINO-ACIDS USING SIMULTANEOUS TG-DSC APPARATUS - THE USE OF DYNAMIC

THERMOGRAVIMETRY TO STUDY THE CHEMICAL-KINETICS OF SOLID-STATE DECOMPOSITION. *Thermochimica Acta* **1990**, *171*, 15-29.

11. Hung, G. W. C., The use of dynamic thermogravimetry and gas chromatography to the study of the chemical kinetics of solid-state decomposition reactions of some selected crystalline amino acids (and comparison of the method of differential thermal analysis). *Thermochimica Acta* **1978**, *23* (2), 233-248.

12. Alexandrova, A. N.; Jorgensen, W. L., On the Mechanism and Rate of Spontaneous Decomposition of Amino Acids. *The Journal of Physical Chemistry B* **2011**, *115* (46), 13624-13632.

13. Abd-Elghany, M.; Klapötke, T. M.; Elbeih, A., Thermal behavior and decomposition kinetics of Bis (2, 2, 2-trinitroethyl)-oxalate as a high energy dense oxidizer and its mixture with nitrocellulose. *Propellants, Explosives, Pyrotechnics* **2017**, *42* (12), 1373-1381.

14. Cai, J.; Xu, D.; Dong, Z.; Yu, X.; Yang, Y.; Banks, S. W.; Bridgwater, A. V., Processing thermogravimetric analysis data for isoconversional kinetic analysis of lignocellulosic biomass pyrolysis: Case study of corn stalk. *Renewable and Sustainable Energy Reviews* **2018**, *82*, 2705-2715.

15. Huang, M.; Lv, S.; Zhou, C., Thermal decomposition kinetics of glycine in nitrogen atmosphere. *Thermochimica Acta* **2013**, *552*, 60-64.

16. Abdelmoez, W.; Nakahasi, T.; Yoshida, H., Amino Acid Transformation and Decomposition in Saturated Subcritical Water Conditions. *Industrial & Engineering Chemistry Research* **2007**, *46* (16), 5286-5294.

17. Olafsson, P. G.; Bryan, A. M., "Procedural activation energies" for the thermolysis reactions of crystalline amino acids by differential scanning calorimetry. *Geochimica Et Cosmochimica Acta* **1971**, 35 (4), 327-336.
18. Khawam, A.; Flanagan, D. R., Solid-State Kinetic Models: Basics and Mathematical Fundamentals. *The Journal of Physical Chemistry B* **2006**, 110 (35), 17315-17328.
19. SAMANMULYA, T.; INOUE, S.; INOUE, T.; KAWAI, Y.; KUBOTA, H.; MUNETSUNA, H.; NOGUCHI, T.; MATSUMURA, Y., Gasification characteristics of amino acids in supercritical water. *Journal of the Japan Institute of Energy* **2014**, 93 (9), 936-943.
20. Rodante, F., Thermodynamics and kinetics of decomposition processes for standard α -amino acids and some of their dipeptides in the solid state. *Thermochimica Acta* **1992**, 200, 47-61.

Chapter 4. In situ DRIFTS During TPO of Amino Acids on α -Alumina and α -Alumina supported Silver Catalyst Analyzed by 2D-COS and MS

4.1. Introduction

The results of the in situ DRIFTS/2D-COS during TPO of the amino acids (20 wt.%) on α -Al₂O₃ and Ag(30%)/ α -Al₂O₃ (described in **Chapter 2**) are presented here. For each sample, the synchronous and asynchronous plots along with the in situ time domain temperature based FTIR spectra are also shown in this chapter. While the synchronous plot indicates whether correlated functional groups increase or decrease in relation to each other, the asynchronous plot shows the order in which these functional groups increase or decrease, with time domain FTIR spectra showing the temperature region of amino acid decomposition. Positive features in the synchronous plot indicate that the changes taking place are in the same direction; from the time domain FTIR spectra we see that these changes are the decreasing peaks for the functional groups of the amino acids. Here, the asynchronous plot are analyzed to predict the order in which the different functional groups react during amino acid oxidation. Regions of the asynchronous plot not analyzed correspond to peaks representing overtone of multiple signals and therefore, only the main characteristic vibrational frequencies are employed (a complete list of peak assignments is given in **Table A6**). Mass spectrometry was also used during the course of the TPO to identify gases exiting the reactor (by following m/z fragments as summarized in **Table A8**), these results are also presented in this chapter. Mass spectra of the major products will be shown along with some of those occurring in trace amounts. These results were used to corroborate the information obtained from the 2D-COS predictions. Information relating to the

bond energies of the amino acids were also reviewed to gain some insight into the observed functional group reactivity.

Before discussing the results, an overview of the bond chemistry of glycine, alanine, valine, and leucine was done to get an insight into their bond dissociation energies; this information may help understand and predict the pathways followed by the amino acids during decomposition.

4.2. Bond Dissociation Energies

Bond dissociation enthalpies (BDE) and free energies (BDFE) of glycine, alanine, valine and leucine are presented and discussed in this section with regards to amino acid stability. As discussed in **Chapter 3**, the selected amino acids correspond to the analog sequence R-CH(COOH)-NH₂ where R corresponds to H, methyl, isopropyl, and isobutyl for glycine, alanine, valine, and leucine, respectively.

Table 4.1 summarizes the BDE and BDFE for glycine and alanine, with each bond been listed in the order of increasing bond energy. Higher bond energies would indicate that reactions to cleave this bond are more difficult to occur. Here, it can be noted then that for glycine, the surface reactions would take place in the bond cleavage order of: CH > CN > CC > NH > CO > OH. This then implies that either surface transformations or gases produced due to oxidation would follow the order: H₂O > NH₃ > CO₂ as a result of the following contributions:

- H₂O due to C-H bond break
- NH₃ due to C-N bond break
- COOH and C-NH₂ due to C-C bond break which would lead to CO₂, H₂O, NH₃
- H₂O due to N-H bond break
- H₂O due to C-O bond break

- H₂O due to O-H bond break

In the case of alanine, the bond dissociation energies increase in the following order: CC (-methyl) > CH (methylene) > CN > CC (methylene-COOH) > NH > CH (methyl) > CO > OH. This then would imply that gases produced due to oxidation follow a slightly different order than for glycine: CO₂ > H₂O > NH₃. In both cases, water changes should be reflected by broad features as dehydrogenation can occur from hydroxyl, methylene, or ammine groups.

Table 4.1. Glycine¹ and Alanine² Bond Dissociation Energies (E: Enthalpy and FE: Free Energy in kcal/mol) as Determined from NREL's ALFABET Machine Learning Approach

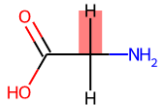
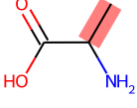
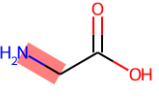
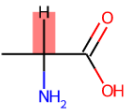
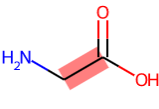
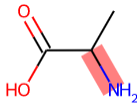
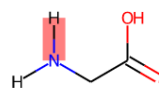
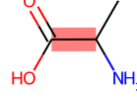
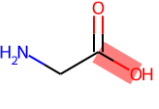
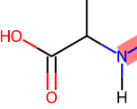
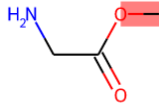
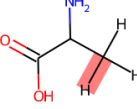

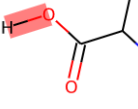
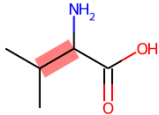
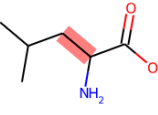
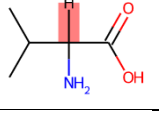
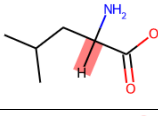
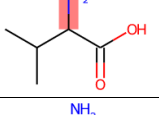
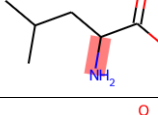
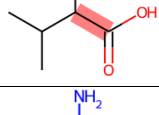
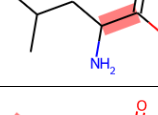
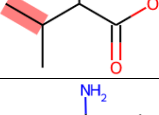
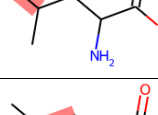
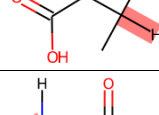
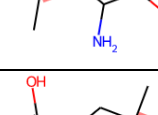
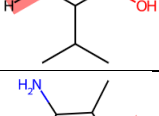
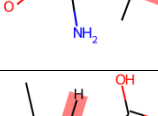
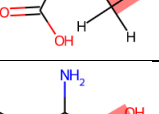
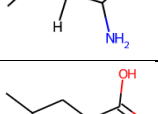
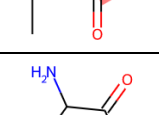
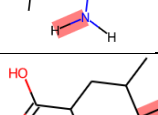
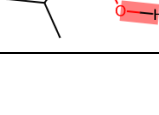
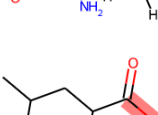
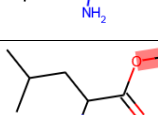
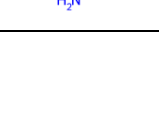
Glycine		Alanine	
	Bond 1 Bond Type: C-H BDE: 78.3 BDFE: 69.8		Bond 1 Bond Type: C-C BDE: 70.0 BDFE: 56.7
	Bond 2 Bond Type: C-N BDE: 83.3 BDFE: 70.8		Bond 2 Bond Type: C-H BDE: 75.2 BDFE: 66.5
	Bond 3 Bond Type: C-C BDE: 87.4 BDFE: 74		Bond 3 Bond Type: C-N BDE: 81.2 BDFE: 67.9
	Bond 4 Bond Type: H-N BDE: 100.0 BDFE: 91.5		Bond 4 Bond Type: C-C BDE: 86.6 BDFE: 72.4
	Bond 5 Bond Type: C-O BDE: 110.7 BDFE: 98.8		Bond 5 Bond Type: H-N BDE: 100.6 BDFE: 92.2
	Bond 6 Bond Type: H-O BDE: 112.7 BDFE: 103.8		Bond 6 Bond Type: C-H BDE: 101.2 BDFE: 92.3
			Bond 7 Bond Type: C-O BDE: 110.3 BDFE: 98.5
			Bond 8 Bond Type: H-O BDE: 112.0 BDFE: 103.1

Table 4.2 summarizes the BDE/BDFE for valine and leucine. Because of the larger functional group attached to the glycine core, the number of bond energies increased. Here, it is seen that the bond cleavage follows the order of: CC (-isopropyl) > CH (methylene) > CN > CC (methylene-COOH) > CC (methyl-isopropyl) > CH (isopropyl) > NH > CO > OH. This then implies that either surface transformations or gases produced due to oxidation would follow the order: CO₂ (from C₃ combustion) > H₂O > NH₃, which also matches that expected for alanine and leucine.

Table 4.2. Valine³ and Leucine Bond Dissociation Energies (E: Enthalpy and FE: Free Energy in kcal/mol) as Determined from NREL's ALFABET Machine Learning Approach

Valine		Leucine	
	Bond 1 Bond Type: C-C BDE: 67.4 BDFE: 52.0		Bond 1 Bond Type: C-C BDE: 68.6 BDFE: 53.7
	Bond 2 Bond Type: C-H BDE: 76.2 BDFE: 67.0		Bond 2 Bond Type: C-H BDE: 74.5 BDFE: 65.5
	Bond 3 Bond Type: C-N BDE: 82.0 BDFE: 68.3		Bond 3 Bond Type: C-N BDE: 80.4 BDFE: 66.9
	Bond 4 Bond Type: C-C BDE: 87.3 BDFE: 72.7		Bond 4 Bond Type: C-C BDE: 86.3 BDFE: 72.0
	Bond 5 Bond Type: C-C BDE: 87.9 BDFE: 73.4		Bond 5 Bond Type: C-C BDE: 86.7 BDFE: 72.1
	Bond 6 Bond Type: C-H BDE: 95.0 BDFE: 85.3		Bond 6 Bond Type: C-C BDE: 86.9 BDFE: 71.1
	Bond 7 Bond Type: H-N BDE: 99.7 BDFE: 91.3		Bond 7 Bond Type: C-H BDE: 94.1 BDFE: 84.4
	Bond 8 Bond Type: C-H BDE: 100.1 BDFE: 91.1		Bond 8 Bond Type: C-H BDE: 97.9 BDFE: 88.6
	Bond 9 Bond Type: C-O BDE: 110.0 BDFE: 98.2		Bond 9 Bond Type: H-N BDE: 100.4 BDFE: 92.0
	Bond 10 Bond Type: H-O BDE: 111.9 BDFE: 103.0		Bond 10 Bond Type: C-H BDE: 100.5 BDFE: 91.4
			Bond 11 Bond Type: C-O BDE: 110.1 BDFE: 98.3
			Bond 12 Bond Type: H-O BDE: 111.7 BDFE: 102.9

The orders for bond cleavage and expectations for gas phase products derived from BDE/BDFE analysis can then be of help to predict functional groups reaction orders which can be tested by DRIFTS 2D-COS and to verify them as well from MS results by tracking gas phase products formation during in situ FTIR and temperature programmed oxidation (TPO).

4.3. Results and Discussion

Figure 4.1 shows the 2D-COS synchronous and asynchronous plots along with time domain in situ FTIR traces during TPO of glycine on α -Al₂O₃. Peaks observed in the time domain plot can be assigned to individual functional groups in glycine (see **Table A6**) including CC (890 cm⁻¹), CN (1030 cm⁻¹), CH₂ (1330, 1440 cm⁻¹), CO (1590 cm⁻¹) and NH₂ (3000, 3160 cm⁻¹); the region around 3500 cm⁻¹ can be attributed to the OH present on the Al₂O₃.^{4, 5} The disappearing peaks in the time domain FTIR spectra with increasing temperature show that decomposition of the acid occurs after 250 °C (**Figure 4.1**). As expected, the synchronous plot correlation is positive in the entire range because all peaks change in the same direction. Therefore, these results and those of other amino acids in the synchronous plot will not be further discussed. From the asynchronous plot, negative features at (890, 1330 cm⁻¹), (890, 1590 cm⁻¹), (890, 3500 cm⁻¹), (890, 3000 cm⁻¹) and (890, 3160 cm⁻¹) indicate that the CC group reacts after the CH₂, CO, OH and NH₂ groups. Negative features around (1330, 3000 cm⁻¹), (1330, 3160 cm⁻¹) and (1330, 3500 cm⁻¹) show that the CH₂ reacts after the NH₂ and OH, with (1330, 1590 cm⁻¹) showing that CH₂ reacts after the CO as well. The negative features around (1590, 3000 cm⁻¹), (1590, 3160 cm⁻¹) and (1590, 3500 cm⁻¹) further indicate that the CO reacts after the NH₂ and OH. Also, positive features in the (3000, 3500 cm⁻¹) and (3160, 3500 cm⁻¹) regions show that the NH₂ reacts before the OH. All in all, these results combined lead to the following order of reaction on the surface based on functional groups: NH₂ > OH > CH₂ > CO > CC. From this

reaction order, we can predict that NH_3 would be the first product from the decomposition. Water would then be formed from the reacting OH from the support and dehydrogenation of methylene group, followed by CO_2 production from the CH_2 and carboxyl group reactions. The presence of some small peaks at 300 °C in the CN (1030 cm^{-1}) and CH_2 (1330 cm^{-1}) regions further elucidate that complete conversion of the amino acid does not take place, with fragments still remaining on the support surface.

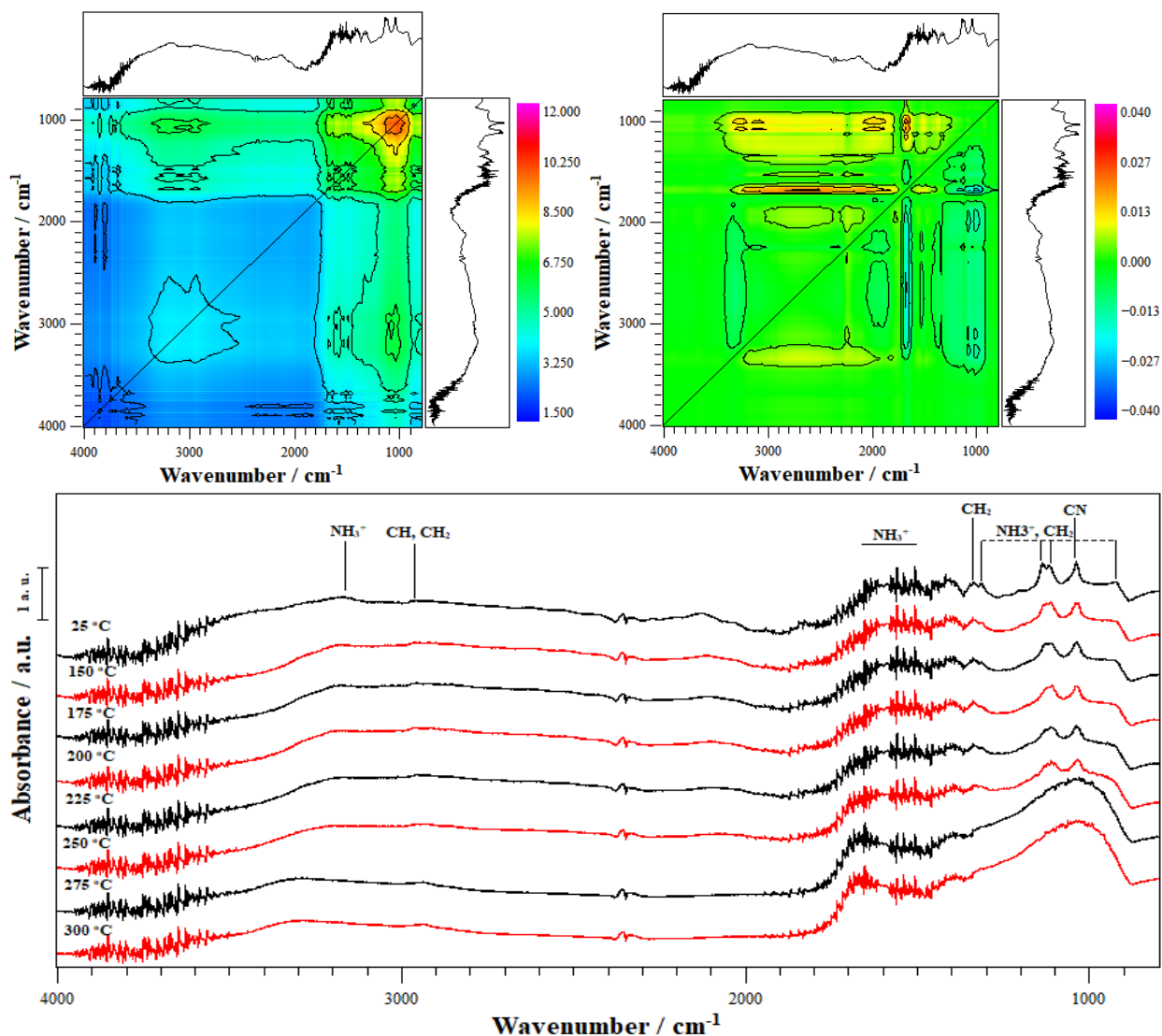


Figure 4.1. Glycine/ Al_2O_3 synchronous (top-left) and asynchronous 2D-COS plots (top-right) and time domain in situ FTIR spectra at different temperatures (bottom) during TPO

Concomitant MS results for TPO of Glycine/ Al_2O_3 (**Figure 4.2**) show that the formation

of products occurs around 250 °C which concurs with the temperature based FTIR spectra. While the peaks for all gaseous products are in very close proximity (probably due to difficulties in resolving sharp peaks from gas phase products due to mixing in the in situ cell and mass spectrometer chamber), rise in NH₃ spectra seems to occur just before water which itself starts increasing before the CO₂, thus agreeing with the order expected from the 2D-COS analysis. It is worth noting that 2D-COS averages all spectra information across the entire TPO temperature range and it is likely that the agreement with MS arises from the single decomposition event for glycine on Al₂O₃ (**Figure 3.1**). Additionally, minute traces of nitrogen oxides were also observed, along with the presence of CO and HCN indicating partial oxidation of the amino acid.

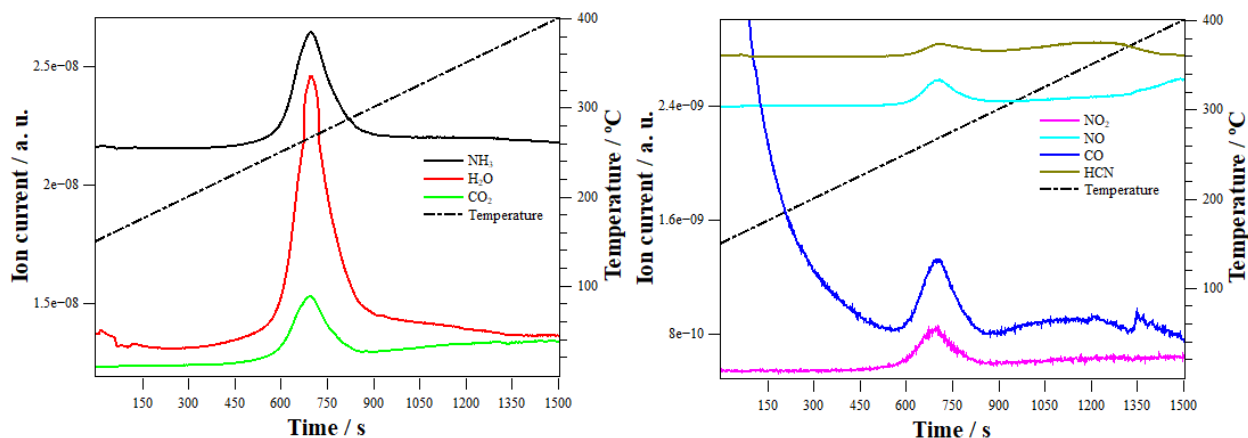


Figure 4.2. Glycine/Al₂O₃ oxidation products from MS corresponding fragments for NH₃, H₂O, CO₂ (left); NO, NO₂, CO, HCN (right)⁶⁻¹² Uncalibrated MS traces were displaced vertically to facilitate reading

Figure 4.3 presents the 2D-COS and time domain in situ FTIR results for TPO of Glycine/Ag/Al₂O₃. The disappearing peaks in the FTIR spectra show that decomposition of the acid occurs after 150 °C in agreement with the TGA results (**Figure 3.2**). As expected from the TGA kinetic analysis, the asynchronous plot is significantly different from that for Glycine/Al₂O₃. Following an analysis of correlation from the 2D-COS data for Glycine/Al₂O₃, we can see that: 1) CC reacts after the OH functional group; 2) CH₂ reacts before the NH₂; 3)

CH₂ reacts before CO and OH functional groups; 4) CO reacts before the NH₂ and OH; and that 5) NH₂ reacts before OH. All these results together lead to the following order of reaction: CH₂ > CO > NH₂ > OH > CC. From this order, we can predict that CH₂ would react first, leading to oxidation products such as CO_x and H₂O. CO₂ would then be produced from the carboxyl group followed by NH₃, after which water would also be produced due to the OH group reaction. In this case, we also observed the presence of some small peaks at 300 °C in the CN (1030 cm⁻¹) and CH₂ (1330 cm⁻¹) regions further indicating that complete conversion of the amino acid does not take place up to these conditions even in the presence of a catalyst.

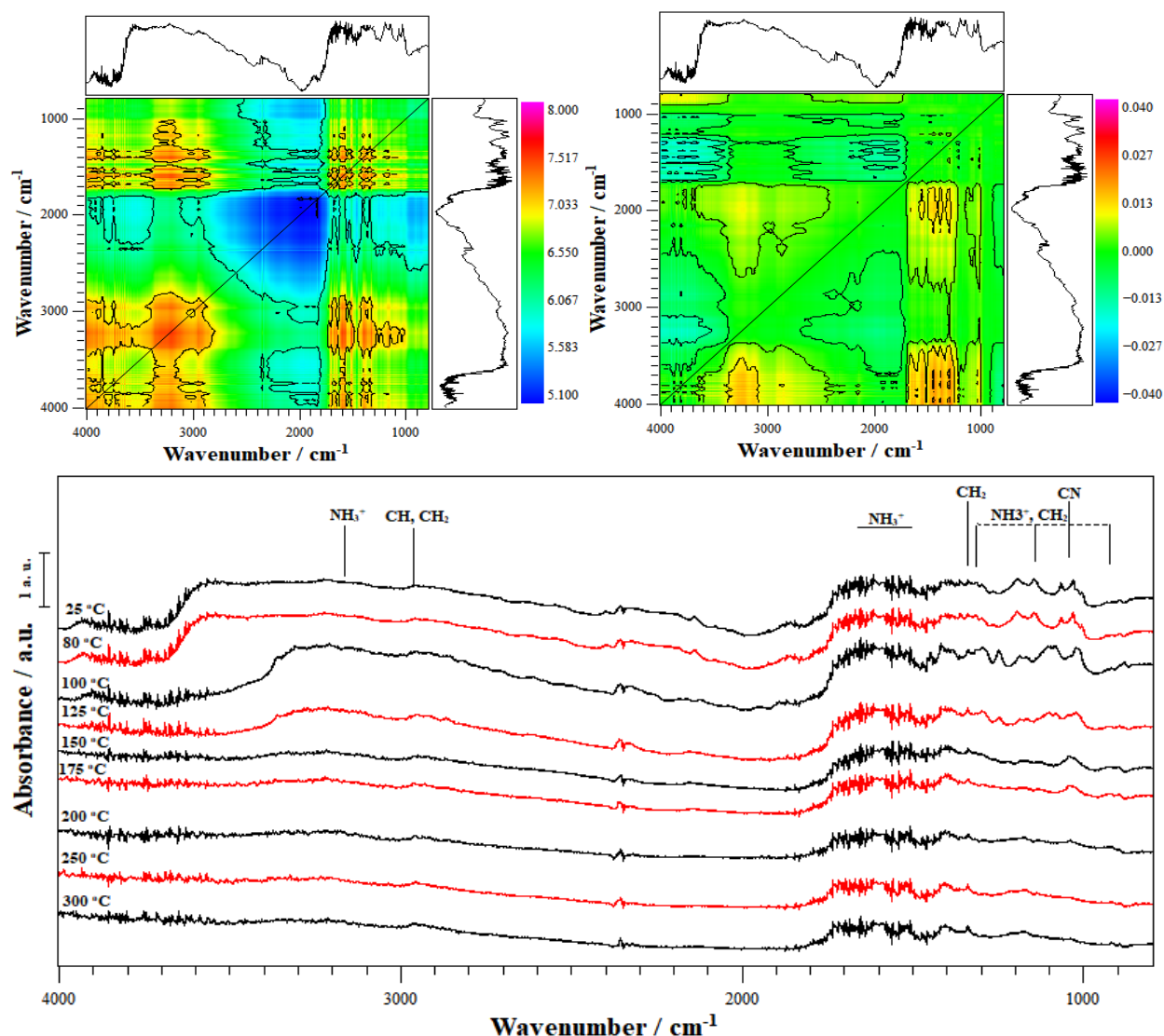


Figure 4.3. Glycine/Ag/Al₂O₃ synchronous (top-left) and asynchronous 2D-COS plots (top-right) and time domain in situ FTIR spectra at different temperatures (bottom) during TPO

From the MS results during TPO of Glycine/Ag/Al₂O₃ (**Figure 4.4**), gas phase products seem to track with the decomposition stages determined from TGA analysis (**Figure 3.1**). For example, the initial decomposition seems to take place around 125 °C. Peaks for CO, CO₂ and H₂O are present just before those for NH₃ and HCN. During the reaction, additional formation of products takes place at around 200 and 300 °C also as expected from TGA, implying further conversion of the amino acid. Broadly, these results agree with the trends predicted from the 2D-

COS as well which predicted an order of CO_x , H_2O > NH_3 at the various temperature conversion stages. The complex and asymmetric MS peaks may reflect the various origins of H_2O and CO_x gas phase products.

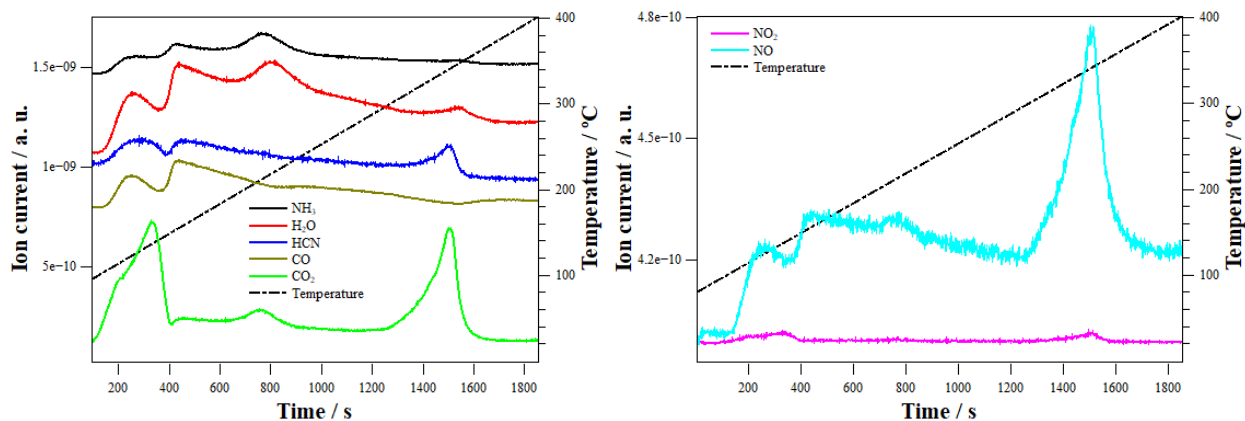


Figure 4.4. Glycine/Ag/Al₂O₃ oxidation products from MS corresponding fragments for NH₃, H₂O, HCN, CO, CO₂ (left); NO, NO₂ (right) ⁶⁻¹² Uncalibrated MS traces were displaced vertically to facilitate reading

2D-COS of in situ FTIR and MS results during TPO for alanine, valine, and leucine on Al₂O₃ and Ag/Al₂O₃ are given in detail in **Figures A7-A18** in the Appendix. As expected from TGA analysis, the decomposition temperatures from time domain in situ FTIR spectra concurs reasonably well. Decomposition temperatures start to occur for alanine, valine, and leucine at around 200, 250, and 200 °C on Al₂O₃, whereas on Ag/Al₂O₃ various functional groups changes occurred over a wider range of temperatures starting at 100-150°C as anticipated by TGA. Moreover, similar to glycine on Al₂O₃ and on Ag/Al₂O₃, time domain in situ FTIR results also evidence the presence of carbonaceous traces on the support or catalysts up to 300 °C indicating incomplete conversion of the amino acid. These results are also supported by the detection of trace amounts of incomplete oxidation products from MS towards higher temperatures, for example, of NO_x and acetone (**Figures A8, A10, A12, A14, A16 and A18**).

Based on the peak assignments as listed in **Table A6** in the Appendix and by performing

a similar correlation analysis to that for Glycine/ Al_2O_3 and Glycine/ $\text{Ag}/\text{Al}_2\text{O}_3$, it is possible to establish the reaction order of functional groups in the corresponding amino acids. For the sake of simplicity, these results are summarized in **Table 4.3**.

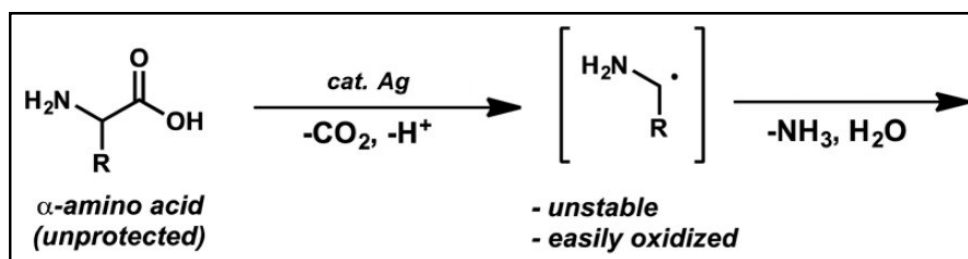
Table 4.3. Comparison of functional groups reaction order

Amino Acid	Pure Amino Acid (from BDE/BDFE)	Amino Acid/α-Al_2O_3 (from 2D-COS)	Amino Acid/ Ag/ α-Al_2O_3 (from 2D-COS)
Glycine	CH > CN > CC > NH > CO > OH	NH ₂ > OH > CH ₂ > CO > CC	CH ₂ > CO > NH ₂ > OH > CC
Alanine	CC (-methyl) > CH (methylene) > CN > CC (methylene-COOH) > NH > CH (methyl) > CO > OH	OH > CC > NH ₂ > CN > CH ₃ > CO	CO > CN > NH ₂ > CC > OH > CH ₃
Valine	CC (-isopropyl) > CH (methylene) > CN > CC (methylene-COOH) > CC (methyl-isopropyl) > CH (isopropyl) > NH > CO > OH	CO > NH ₂ > OH > CH ₂ > CC, CN > CH	CH ₂ > NH ₂ > OH > CO > CC, CN > CH
Leucine	Similar to Valine	CH ₂ > CH > CO > NH ₂ > OH > CC > CN	CC > CO > CN > NH ₂ > OH > CH, CH ₂

The results in this table clearly show that BDE and 2D-COS mostly agree when the amino acid is adsorbed on the $\text{Ag}/\text{Al}_2\text{O}_3$ catalyst when the main expected gaseous products are CO_x , H_2O followed by NH_3 likely as a result of the favorable oxidation energetics of the CC, CH, and CO bonds in methylene, alkyl, or carboxyl groups. When the catalyst is employed, MS also show that at low temperatures, CO_x and H_2O also evolve just before NH_3 as a result of the high activity of the silver catalyst. While BDE/BDFE do not quite track with 2D-COS results for amino acids on Al_2O_3 , the latter do seem to concord with MS gas evolution where NH_3 and H_2O evolve slightly faster than CO_2 . These results may be explained by the known inability of Al_2O_3 to catalyze oxidation reactions, thus suggesting that the observed products on this material of are

the result of amino acids thermal decomposition. Similar to Glycine MS results on Al₂O₃ and Ag/Al₂O₃, gaseous products (e.g., CO_x, H₂O, NH₃) temperature evolution tracks with that expected from TGA amino acid decomposition indicating that thermal and/or oxidation reactions are taking place. Such coincidence of temperature is even more evident when the catalyst is used where multiple stages for the decomposition of the amino acids (e.g., alanine, valine, leucine) are clearly noted.

In conclusion, for all amino acids, significant reduction in decomposition temperatures is observed in the presence of the Ag(30%)/ α -Al₂O₃ catalyst. The higher decomposition temperatures on the α -Al₂O₃ support than in the presence of the silver catalyst could be due to the fact Al₂O₃ is a poor oxidation catalyst and that amino acids may undergo peptide formation in the presence of alumina, resulting in stabler intermediates before decomposition.¹³ A possible explanation for the difference in behavior on the Ag catalyst could be that Ag catalysts are excellent oxidation catalysts, but also because they have been shown to promote easy decarboxylation of unprotected amino acids (**Scheme 4.1**), leading to unstable amino alkyl intermediate species which can then undergo rapid deamination.¹⁴



Scheme 4.1 Amino alkyl radical formation in presence of Ag catalyst¹⁴

4.4. References

1. Glycine bond dissociation energies.

<https://bde.ml.nrel.gov/result?name=C%28C%28%3DO%29O%29N> (accessed July 26, 2022).

2. Alanine bond dissociation energies.
<https://bde.ml.nrel.gov/result?name=CC%28C%28%3DO%29O%29N> (accessed July 26, 2022).
3. Valine bond dissociation energies.
<https://bde.ml.nrel.gov/result?name=CC%28C%29C%28C%28%3DO%29O%29N> (accessed July 26, 2022).
4. Chowdhry, B. Z.; Dines, T. J.; Jabeen, S.; Withnall, R., Vibrational Spectra of α -Amino Acids in the Zwitterionic State in Aqueous Solution and the Solid State: DFT Calculations and the Influence of Hydrogen Bonding. *The Journal of Physical Chemistry A* **2008**, *112* (41), 10333-10347.
5. Morterra, C.; Ghiotti, G.; Garrone, E.; Boccuzzi, F., Infrared spectroscopic characterization of the α -alumina surface. *Journal of the Chemical Society, Faraday Transactions 1: Physical Chemistry in Condensed Phases* **1976**, *72*, 2722-2734.
6. NH₃ mass spectrometry.
<https://webbook.nist.gov/cgi/cbook.cgi?ID=C7664417&Units=SI&Mask=200#Mass-Spec> (accessed July 25, 2022).
7. H₂O mass spectrometry.
<https://webbook.nist.gov/cgi/cbook.cgi?ID=C7732185&Units=SI&Mask=200#Mass-Spec> (accessed July 25, 2022).
8. CO₂ mass spectrometry.
<https://webbook.nist.gov/cgi/cbook.cgi?ID=C124389&Units=SI&Mask=200#Mass-Spec> (accessed July 25, 2022).

9. NO mass spectrometry.

<https://webbook.nist.gov/cgi/cbook.cgi?ID=C10102439&Units=SI&Mask=200#Mass-Spec>

(accessed July 27, 2022).

10. NO₂ mass spectrometry.

<https://webbook.nist.gov/cgi/cbook.cgi?ID=C10102440&Units=SI&Mask=200#Mass-Spec>

(accessed July 27, 2022).

11. HCN mass spectrometry.

<https://webbook.nist.gov/cgi/cbook.cgi?ID=C74908&Units=SI&Mask=200#Mass-Spec>

(accessed July 27, 2022).

12. CO mass spectrometry.

<https://webbook.nist.gov/cgi/cbook.cgi?ID=C630080&Units=SI&Mask=200#Mass-Spec>

(accessed July 27, 2022).

13. Bujdak, J.; Rode, B. M., Alumina catalyzed reactions of amino acids. *Journal of Thermal Analysis and Calorimetry* **2003**, 73 (3), 797-805.

14. Hua, A. M.; Mai, D. N.; Martinez, R.; Baxter, R. D., Radical C–H Fluorination Using Unprotected Amino Acids as Radical Precursors. *Organic Letters* **2017**, 19 (11), 2949-2952.

Chapter 5. Conclusions and Future Work

As the living in pandemics becomes the norm, the need for simple and effective methods to identify and study microorganisms and viruses has grown substantially. A review of patents and inventions in the field shows the vast applications of metal/metal oxide catalysts, as means to understand viral activity and for their virucidal potential. In this work, α -Al₂O₃ and an α -Al₂O₃ supported Ag catalyst were used to prepare admixtures with amino acids with the objective of finding a straightforward method to characterize biomolecules and to study their oxidation on metal/metal oxide surfaces.

Four amino acid analogs, namely glycine, alanine, valine and leucine that make up viral proteins were, through TGA, shown to decompose on α -Al₂O₃ support and oxidize on Ag(30%)/ α -Al₂O₃ catalyst surfaces. While the temperature of decomposition lowered on the Ag catalyst, kinetic studies on the TGA data also revealed a reduction in activation energies for the oxidation, suggesting catalytic activity on silver surfaces.

To understand the possible reaction pathways followed by the amino acids, their bond dissociation energies (BDE), derived from machine learning approach using an NREL database, were analyzed to predict the order of bond cleavage. In situ DRIFTS was used to characterize the adsorbed amino acids on the support and catalyst during TPO along with MS characterization of gaseous products. The IR spectra collected showed the loss of peaks corresponding to reacted functional groups and time domain data also showed the temperature ranges of decomposition, which were in close agreement with those observed from TGA under oxidizing conditions. With the utilization of 2D-COS, results from infrared spectroscopy were further analyzed in detail to understand the order of reactivity of functional groups relative to one other, providing important information about reaction and expected products without the use of additional equipment or

methods. Mass spectrometry was used to analyze gases evolved during the reaction to confirm the predictions from the 2D-COS procedure. From the time domain in situ DRIFTS during TPO, we observed that complete oxidation was not achieved up to 300 °C, with residual fragments remaining on the surface after the reaction, which agrees with the high stability of amino acids.

Overall, it was found that BDE expected reactivity trends tracked moderately with functional group changes during TPO on amino acids/Ag/Al₂O₃ but not with the amino acids/Al₂O₃ samples. When employing the silver catalyst, the main expected gaseous products were CO_x, H₂O followed by NH₃ likely as a result of the favorable oxidation energetics of the CC, CH, and CO bonds in methylene, alkyl, or carboxyl groups. MS also showed that at low temperatures, CO_x and H₂O also evolve just before NH₃ as a result of the high activity of the silver catalyst. In the case of amino acid/Al₂O₃ samples, only 2D-COS predictions matched with evolved gases for most amino acids TPO, where NH₃ and H₂O evolve slightly faster than CO₂.

Thus, in situ DRIFTS/2D-COS in combination with online MS proved to be a useful tool for quickly and qualitatively tracking and understanding changes in real time and determining the reaction dynamics in amino acids interacting with catalytic surfaces. These results were explained by inability of Al₂O₃ to catalyze oxidation reactions and thus suggested that the observed gaseous products by MS were the result of amino acids thermal decomposition.

In the future, various other supports and metal catalysts will be studied to determine the selection of catalysts to both preserve and expend biological systems such as proteins, viruses, etc. For instance, peptides such as glycylglycine and glycylglycylglycine could be studied, using different supports such as silica with different porosity and different metal catalysts such as Cu. Larger and different biomolecules could be similarly studied towards achieving the objective of working with virus like particles on metal/ metal oxide catalysts and to expand the applicability

of in situ DRIFTS/2D-COS to more complex biomolecules.

Appendices

1. Preliminary Calculations for Catalysts Preparation

The tables below present the physical properties of the used materials and detailed calculations for catalysts preparation.

Table A1. Physical properties of the used materials

Constant	Value
AgNO ₃ molecular weight / g/mole	169.87
Ag Atomic Weight / g/mole	107.868
Oxalic Acid Molecular Weight / g/mole	90.04
Silve Oxalate Molecular Weight / g/mole	303.74
Water molecular weight / g/mol	18
Water density / g/cm ³	1
Ethylenediamine density / g/cm ³	0.899
Support	α -Alumina
Support specific surface area (manufacturer)/ m ² /g	8
Support water specific pore volume/ cm ³ /g	0.15

Table A2. Silver catalyst preparation target values and calculations required for the impregnation solution and number of impregnations

Targets	
Targeted Particle size / nm	120
Support amount / g	7.5
Total support surface area / m ²	60
Total pore volume	1.125
Total Ag weight / g	3.20
Total Ag / Moles	0.029
Number of Ag total Atoms	1.8E+22
Number of Ag Atoms in single Spherical NP	5.3E+07
Number of Spherical Ag NPs	3.40E+14
Interparticle distance / nm	253.26
Catalyst weight / g	10.70
Ag wt%	29.92
Calculations of required impregnation solution and number of impregnations	
AgNO ₃ Concentration / M	0.4
Oxalic Acid Concentration / M	0.2
AgNO ₃ weight needed / g	5.04
AgNO ₃ moles needed / m	0.0297
Volume of water need for AgNO ₃ solution / ml	74.22
Oxalic acid moles needed / mol	0.059
Oxalic Acid weight needed / g	5.46
Volume of water need for Oxalic Acid solution / ml	296.88
Total volume after mixing both solutions	371.10
Filtered silver oxalate wight / g	4508.77
Ethylenediamine weight needed / g	4342.81
Water weight needed / g	4275.12
Total volume of impregnation solution / ml	9.11
Total impregnation volume / ml	1.24
Number of impregnations	12

Table A3. Amino acid water solubilities

Amino acid	Solubility (g/100ml water)
Glycine	24.990
Alanine	16.720
Valine	8.850
Leucine	2.426

2. Amino Acid Sample Preparation Calculations**Table A4. Amino acid/alumina**

Amino Acid	Purity	Solubility (g/100ml)	Sample wt. %	Support wt. (g)	Acid amt. req. (g)	Act. acid amt. req. (g)	Solution wt. %	Solution vol. (ml)	Acid amt. req. for solution (g)	Vol. of solution req. (ml)
Glycine	0.99	24.990	25	0.6	0.15	0.152	24.990	10	2.499	0.606
Alanine	0.98	16.720	25	0.6	0.15	0.153	16.720	10	1.672	0.915
Valine	0.98	8.850	25	0.6	0.15	0.153	8.850	10	0.885	1.730
Leucine	0.99	2.426	25	0.6	0.15	0.152	2.426	10	0.243	6.245

Table A5. Amino acid/Ag/alumina

Amino Acid	Purity	Solubility (g/100ml)	Sample wt. %	Support wt. (g)	Acid amt. req. (g)	Act. acid amt. req. (g)	Solution wt. %	Solution vol. (ml)	Acid amt. req. for solution (g)	Vol. of solution req. (ml)
Glycine	0.99	24.990	25	2	0.5	0.505	24.990	10	2.499	2.021
Alanine	0.98	16.720	25	2	0.5	0.510	16.720	10	1.672	3.051
Valine	0.98	8.850	25	2	0.5	0.510	8.850	10	0.885	5.765
Leucine	0.99	2.426	25	2	0.5	0.505	2.426	30	0.728	20.818

3. Amino Acid IR Peak Assignments

Table A6. Reported peak assignments for glycine,^{1,2} alanine,^{1,2} valine³ and leucine^{2,4}

Func. Grps.	Amino Acids Wavenumber (cm ⁻¹)			
	Alanine	Glycine	Valine	Leucine
NH ₂ str.	3070	3160	3420	3420
	3010	3000		3360 3090
NH ₂ bend.	1640	1660	1630	1680
	1590	1590	975	1630
	1520	1520	890	1430
	1505	1500	825 800	1410
NH ₂ rock.	1300	910	---	1240
	1235			1040
	1150	1000		
	1010			
NH ₂		1310		1180
	---	1130	---	800
		1100		
OH str.	---	---	3560 3180	---
	---	---	1300	---
OH bend.	---	---	---	---
CH ₃ str.	---	---	---	3020 2950
	2800	---	1050	1510 - 1480 1400 1000
1450	---			
CH ₂ str.	---	2960	2950 - 2900	3020
	---	2890		
CH ₂ bend.	---	1440	1470	1510 - 1480 1430
		1410		
		1385		
CH ₂ rock.	---	910	---	---

Table A6. Reported peak assignments for glycine,^{1,2} alanine,^{1,2} valine³ and leucine^{2,4} (continued)

Func. Grps	Amino Acids Wavenumber (cm ⁻¹)			
	Alanine	Alanine	Alanine	Alanine
CH ₂ o.o.p.	---	1330 1130 1100	---	1330 1240
CH str.	---	---	---	3090 3080 9075
CH bend.	---	---	1320 1300 1050 960	1280 1180 1040
CC str.	1410 1110 920	890 600	1140 1040 975 945 825 800 780 720 700	1330 1140 970 860
CC bend.	770	600	655	---
CC o.o.p.	---	---	---	---
C=O str.	1640 1590 1300 850	---	1780 1760	1680
C-O str.	---	---	1160 720	---
CN str.	---	1030	1160 1140 945 890	930 860
CN bend.	---	690 600	645	1140 670

4. Amino Acid Mass Spectrometry

Table A7. Possible amino acid decomposition products reported in literature

Amino Acid	Possible Decomposition Products
Glycine	NH ₃ , H ₂ O, CO, CO ₂ , NO, NO ₂ , HCN ⁵⁻⁷
Alanine	NH ₃ , H ₂ O, CO, CO ₂ , NO, NO ₂ , (CH ₃) ₂ CO ^{6, 8, 9}
Valine	NH ₃ , H ₂ O, CO, CO ₂ , NO, NO ₂ , (CH ₃) ₂ CO ^{9, 10}
Leucine	NH ₃ , H ₂ O, CO, CO ₂ , NO, NO ₂ , (CH ₃) ₂ CO ^{9, 10}

Table A8. Example of mass spectrometry products m/z values vs % intensity

m/z	FW	16	17	18	27	30	32	38	39	40	41	42	43	44	46
Acetone, C ₃ H ₆ O	58	1			10			5	8	2	5	11	100	5	
Isobutane, C ₄ H ₁₀	58	1			30	1		4	17	4	39	33	100	5	
But-2-ene, C ₄ H ₈	56	4			35		15	8	53	14	100	4			
Nitrous Dioxide, NO ₂	46	22				100									38
Carbon Dioxide, CO ₂	44	10												100	1
Argon, Ar	40							0		100					
Water, H ₂ O	18	1	21	100											
Oxygen, O ₂	32	22					100								
Ammonia, NH ₃	17	80	100												
Carbon Monoxide, CO	28	2													
Nitrogen, N ₂	28														
Nitrous Oxide, N ₂ O	44					32								100	
Acetone, (CH ₃) ₂ CO		1			7			3	5	13	3	10	100	2	
Nitric Oxide, NO	30					100									
Carbon Monoxide, CO	28	2													
Hydrogen Cyanide, HCN	27				100										

5. TGA Results

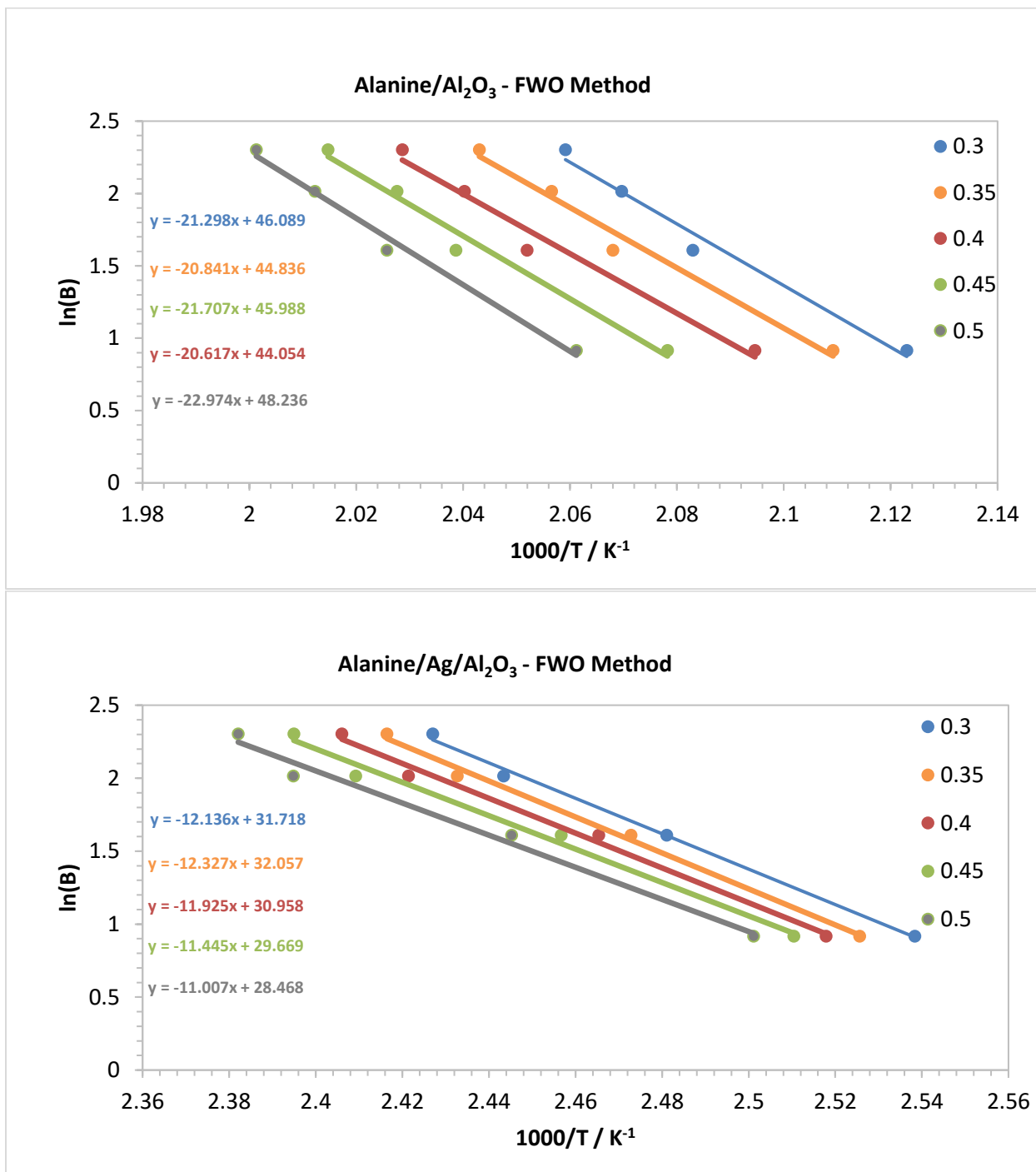


Figure A1. TGA kinetic analysis for Alanine/Al₂O₃ (top) and Alanine/Ag/Al₂O₃ (bottom): FWO method

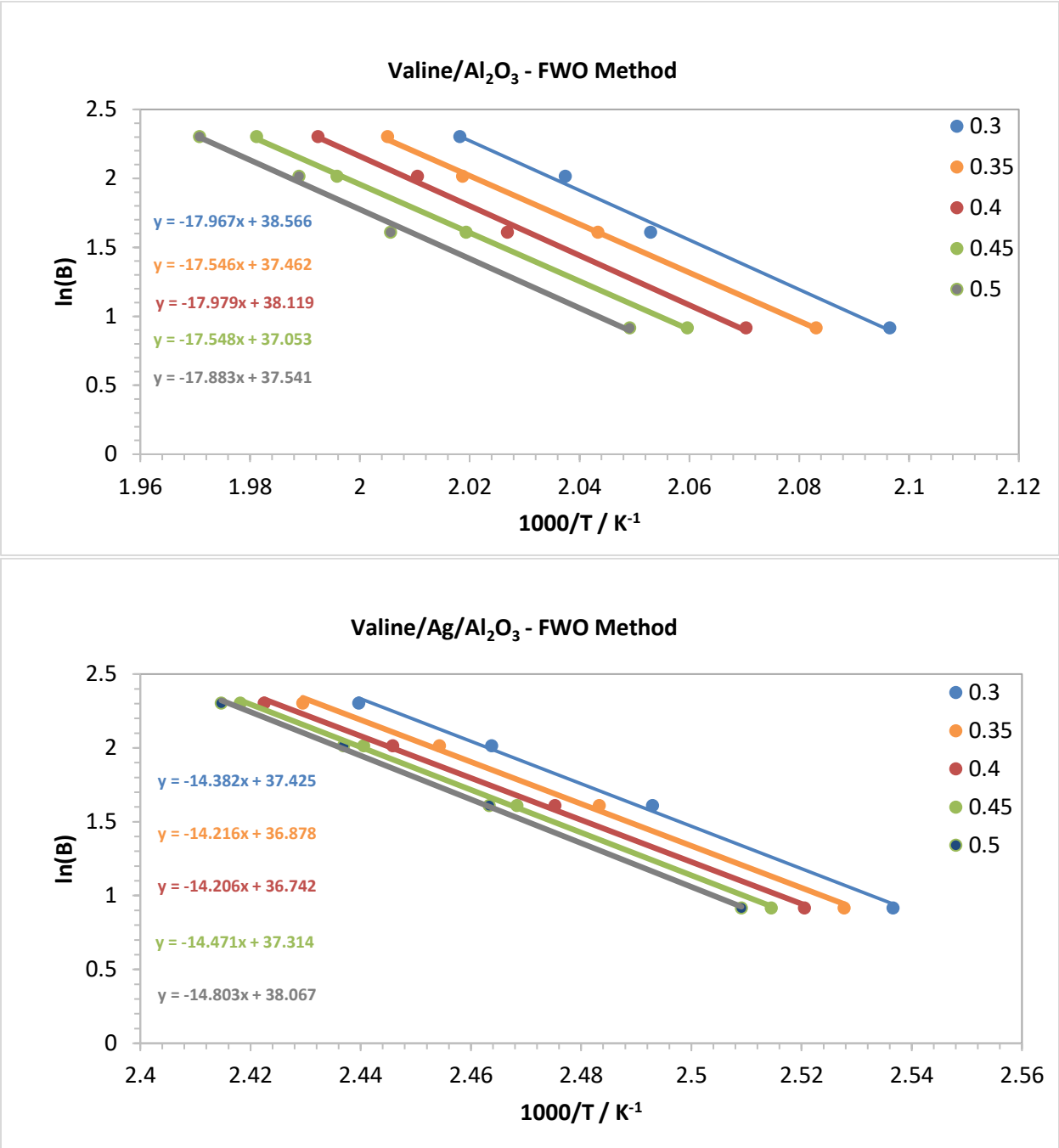


Figure A2. TGA kinetic analysis for Valine/Al₂O₃ (top) and Valine/Ag/Al₂O₃ (bottom): FWO method

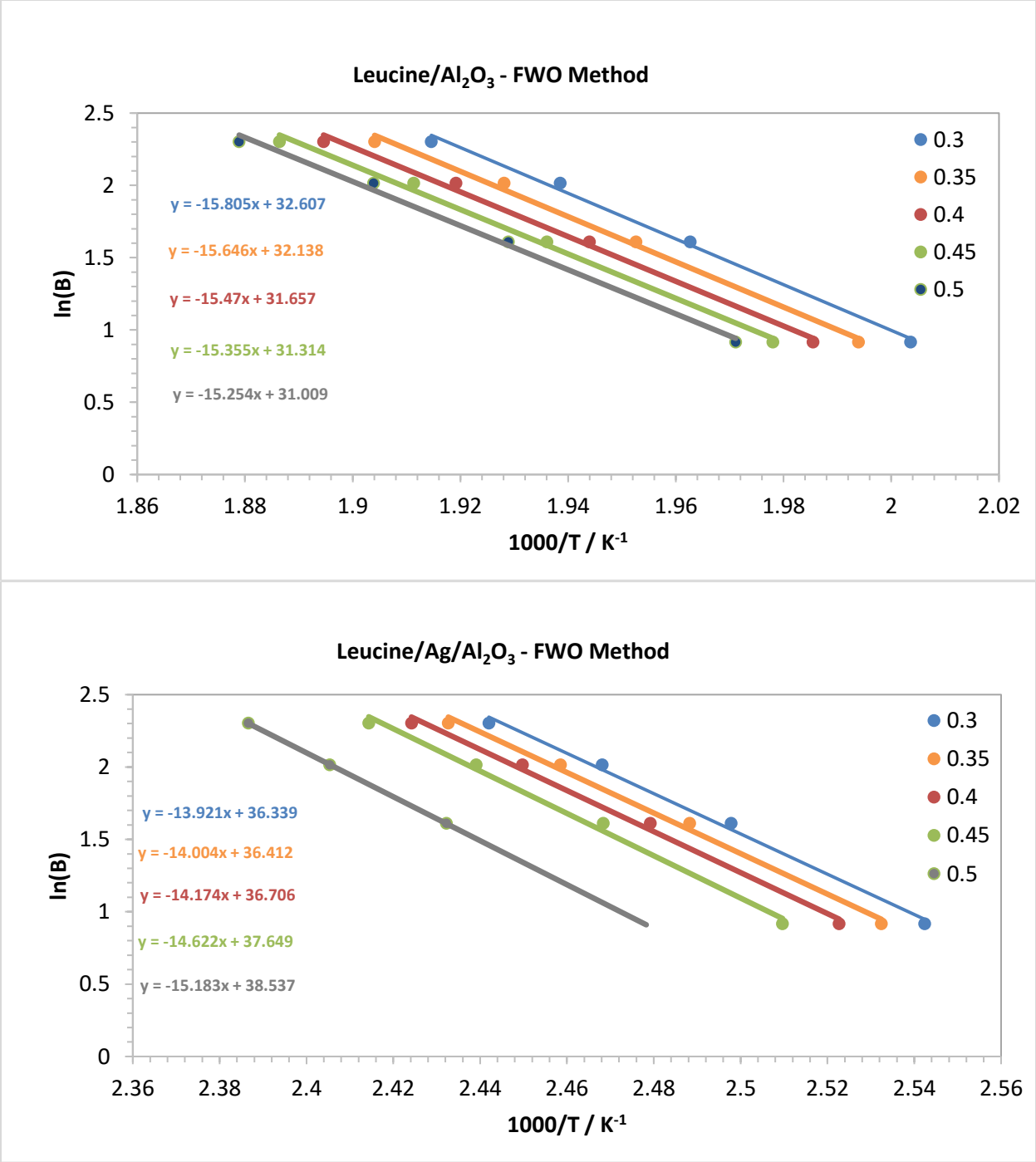


Figure A3. TGA kinetic analysis for Leucine/Al₂O₃ (top) and Leucine/Ag/Al₂O₃ (bottom): FWO method

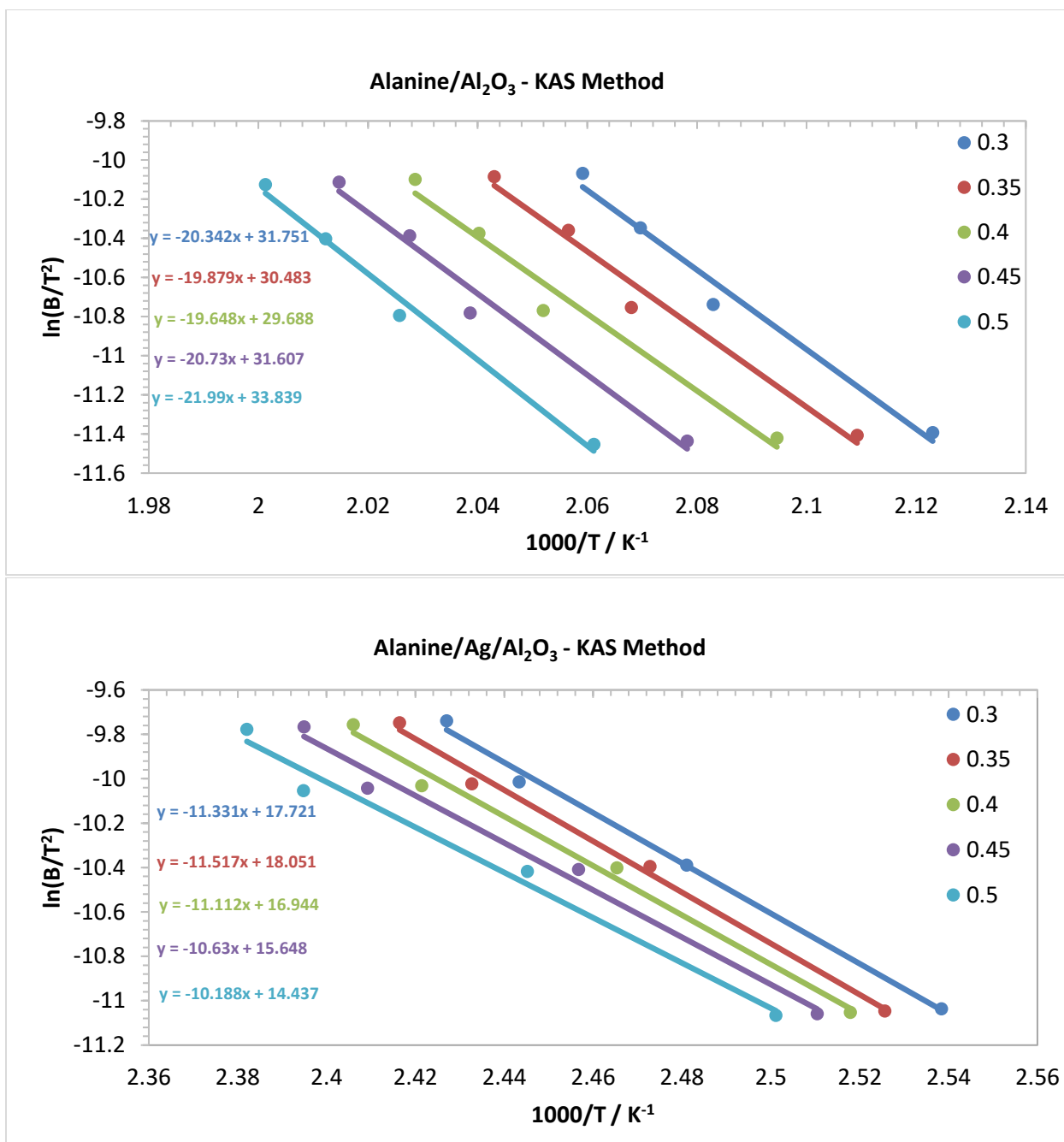


Figure A4. TGA kinetic analysis for Alanine/Al₂O₃ (top) and Alanine/Ag/Al₂O₃ (bottom): KAS method

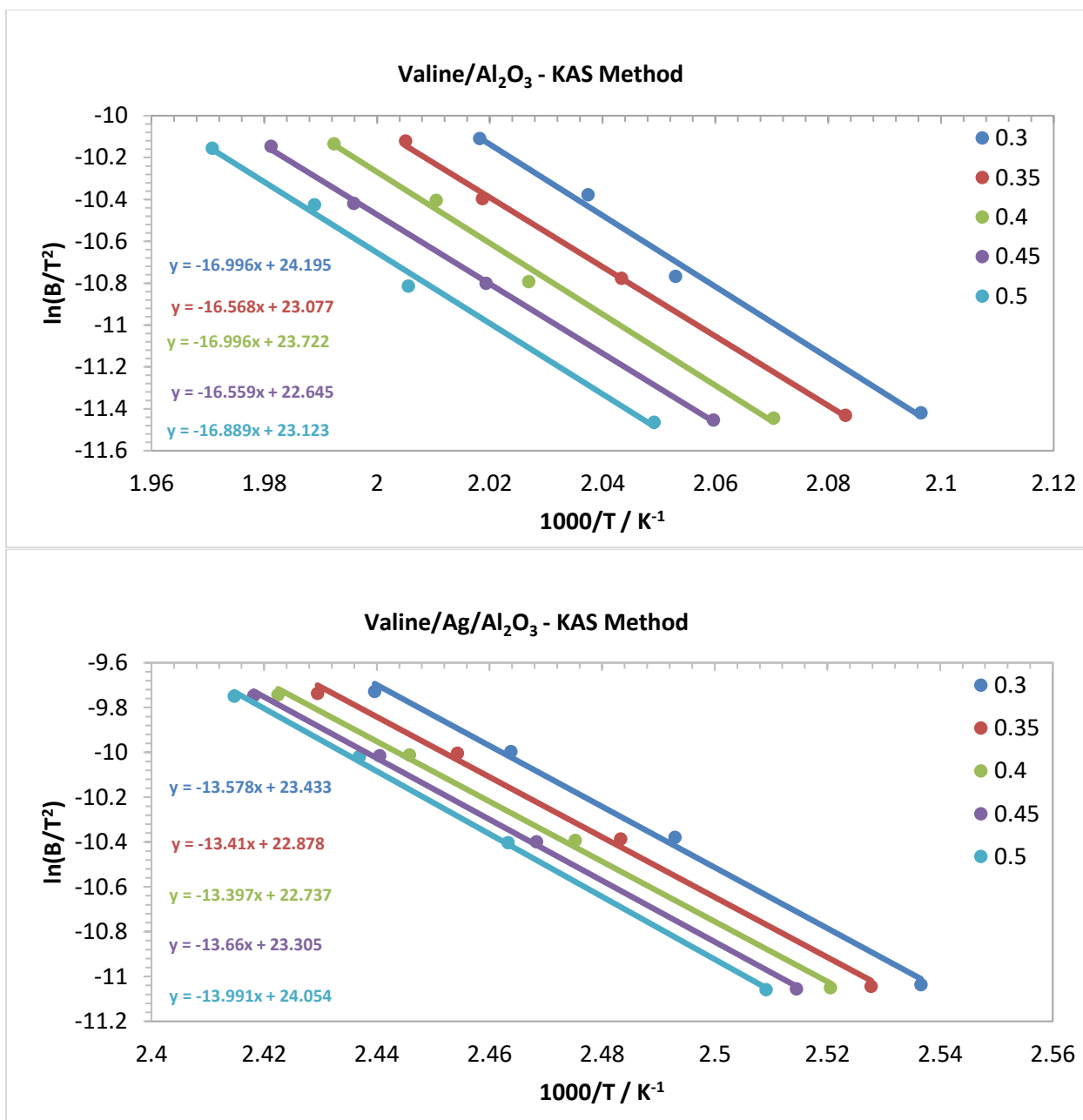


Figure A5. TGA kinetic analysis for Valine/Al₂O₃ (top) and Valine/Ag/Al₂O₃ (bottom): KAS method

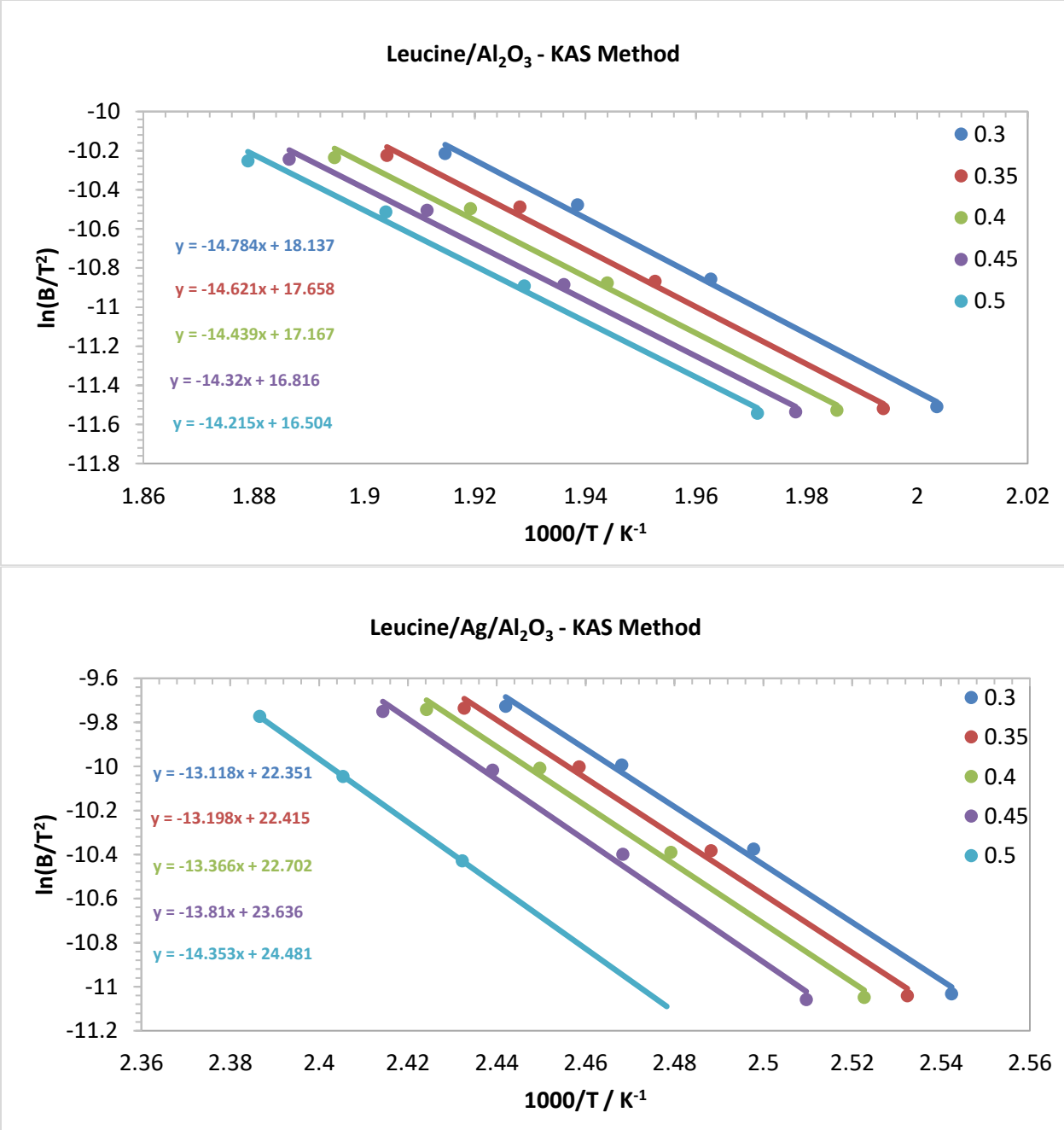


Figure A6. TGA kinetic analysis for Leucine/Al₂O₃ (top) and Leucine/Ag/Al₂O₃ (bottom): KAS method

Table A9. Glycine/ α -Al₂O₃ calculated activation energy and pre-exponential factors

Glycine/ α -Al ₂ O ₃	FWO			KAS		
Conversion α	E _a (kJ mol ⁻¹)	A (min ⁻¹)	R ²	E _a (kJ mol ⁻¹)	A (min ⁻¹)	R ²
0.30	169.99	5.59E+19	0.999	170.43	6.02E+13	0.999
0.35	168.85	4.60E+19	0.999	169.22	4.86E+13	0.999
0.40	168.00	4.40E+19	0.999	168.63	4.57E+13	0.999
0.45	168.31	4.40E+19	0.999	168.28	4.40E+13	0.999
0.50	167.99	6.40E+19	0.999	169.57	6.69E+13	0.999
Avg.	168.63	5.08E19		169.23	5.31E13	
Std. dev.	0.84	8.88E+19	—	0.84	1E+13	—

Table A10. Glycine/Ag/ α -Al₂O₃ calculated activation energy and pre-exponential factors

Glycine/Ag/ α -Al ₂ O ₃	FWO			KAS		
Conversion α	E _a (kJ mol ⁻¹)	A (min ⁻¹)	R ²	E _a (kJ mol ⁻¹)	A (min ⁻¹)	R ²
0.30	101.10	3.61E+15	0.982	99.78	2.20E+9	0.979
0.35	101.03	3.51E+15	0.978	99.67	2.11E+9	0.975
0.40	100.58	3.11E+15	0.974	99.16	1.83E+9	0.970
0.45	100.79	3.41E+15	0.972	99.36	2.00E+9	0.968
0.50	102.34	5.67E+15	0.971	100.97	3.41E+9	0.968
Avg.	101.17	3.86E15	-	99.79	2.31E+9	-
Std. dev.	0.69	1E+15	-	0.70	6.30E+8	-

Table A11. Alanine/ α -Al₂O₃ calculated activation energy and pre-exponential factors

Alanine/ α -Al ₂ O ₃	FWO			KAS		
Conversion α	E _a (kJ mol ⁻¹)	A (min ⁻¹)	R ²	E _a (kJ mol ⁻¹)	A (min ⁻¹)	R ²
0.30	168.32	3.78E+20	0.981	169.12	4.47E+14	0.980
0.35	164.71	1.33E+20	0.980	165.27	1.48E+14	0.979
0.40	162.94	7.31E+19	0.975	163.35	7.85E+13	0.972
0.45	171.55	5.62E+20	0.980	172.35	6.61E+14	0.979
0.50	181.56	5.83E+21	0.990	182.83	7.97E+15	0.989
Avg.	169.82	1.39E21	-	170.59	1.86E+15	-
Std. dev.	7.36	2.49E+21	-	7.68	3.40E+15	-

Table A12. Alanine/Ag/ α -Al₂O₃ calculated activation energy and pre-exponential factors

Alanine/Ag/ α -Al ₂ O ₃	FWO			KAS		
Conversion α	E _a (kJ mol ⁻¹)	A (min ⁻¹)	R ²	E _a (kJ mol ⁻¹)	A (min ⁻¹)	R ²
0.30	95.91	3.81E+14	0.996	94.21	1.22E+08	0.996
0.35	97.42	6.35E+14	0.995	95.75	3.43E+08	0.994
0.40	94.25	2.59E+14	0.992	92.39	1.29E+08	0.991
0.45	90.45	8.72E+13	0.989	88.38	3.97E+07	0.987
0.50	86.99	3.16E+13	0.985	84.70	1.19E+07	0.984
Avg.	93.00	2.79E14	-	91.09	1.29E+08	-
Std. Dev.	4.25	2.4E+14	-	4.51	1.30E+08	-

Table A13. Valine/ α -Al₂O₃ calculated activation energy and pre-exponential factors

Valine/ α -Al ₂ O ₃	FWO			KAS		
Conversion α	E _a (kJ mol ⁻¹)	A (min ⁻¹)	R ²	E _a (kJ mol ⁻¹)	A (min ⁻¹)	R ²
0.30	141.99	2.42E+17	0.992	141.31	1.95E+11	0.991
0.35	138.67	9.93E+16	0.999	137.75	7.51E+10	0.999
0.40	142.09	2.22E+17	0.994	141.06	1.74E+11	0.993
0.45	138.68	9.15E+16	0.999	137.67	6.77E+10	0.999
0.50	141.33	1.69E+17	0.994	140.42	1.29E+11	0.993
Avg.	140.55	1.65E17	-	139.64	1.28E+11	-
Std. dev.	1.74	6.88E+16	-	1.79	5.71E+10	-

Table A14. Valine/Ag/ α -Al₂O₃ calculated activation energy and pre-exponential factors

Valine/Ag/ α -Al ₂ O ₃	FWO			KAS		
Conversion α	E _a (kJ mol ⁻¹)	A (min ⁻¹)	R ²	E _a (kJ mol ⁻¹)	A (min ⁻¹)	R ²
0.30	113.66	9.66E+16	0.996	112.89	7.28E+10	0.996
0.35	112.35	6.83E+16	0.996	111.49	4.98E+10	0.996
0.40	112.27	7.08E+16	0.998	111.38	5.13E+10	0.998
0.45	114.37	1.44E+17	0.999	113.57	1.08E+11	0.999
0.50	116.99	3.47E+17	0.999	116.32	2.71E+11	0.999
Avg.	113.33	1.45E+17	-	113.13	1.11E11	-
Std. dev.	1.93	1.17E+17	-	2.01	9.27E+10	-

Table A15. Leucine/ α -Al₂O₃ calculated activation energy and pre-exponential factors

Leucine/α-Al₂O₃	FWO			KAS		
Conversion α	E_a (kJ mol⁻¹)	A (min⁻¹)	R²	E_a (kJ mol⁻¹)	A (min⁻¹)	R²
0.30	124.91	7.11E+14	0.995	122.91	3.97E+08	0.994
0.35	123.65	5.43E+14	0.995	121.56	2.94E+08	0.995
0.40	122.26	4.02E+14	0.995	120.05	2.11E+08	0.994
0.45	121.35	3.37E+14	0.995	119.06	1.72E+08	0.994
0.50	120.55	2.89E+14	0.995	118.18	1.45E+08	0.994
Avg.	122.55	4.56E+14	-	120.35	2.44E+08	-
Std. dev.	1.75	1.71E+14	-	1.90	1E+08	-

Table A16. Leucine/Ag/ α -Al₂O₃ calculated activation energy and pre-exponential factors

Leucine/Ag/α-Al₂O₃	FWO			KAS		
Conversion α	E_a (kJ mol⁻¹)	A (min⁻¹)	R²	E_a (kJ mol⁻¹)	A (min⁻¹)	R²
0.30	110.02	3.37E+16	0.995	109.06	2.38E+10	0.994
0.35	110.67	4.35E+16	0.995	109.73	3.09E+10	0.994
0.40	112.02	6.84E+16	0.995	111.13	4.94E+10	0.999
0.45	115.56	7.33E+16	0.994	114.82	5.59E+10	0.993
0.50	117.73	1.55E+26	1	116.65	1.18E+20	1
Avg.	113.20	3.09E25	-	112.28	2.35E+19	-
Std. dev.	3.32	6.90E+25	-	3.31	5.30E+19	-

6. TPO 2D-COS, Time Domain in Situ FTIR, and MS Results

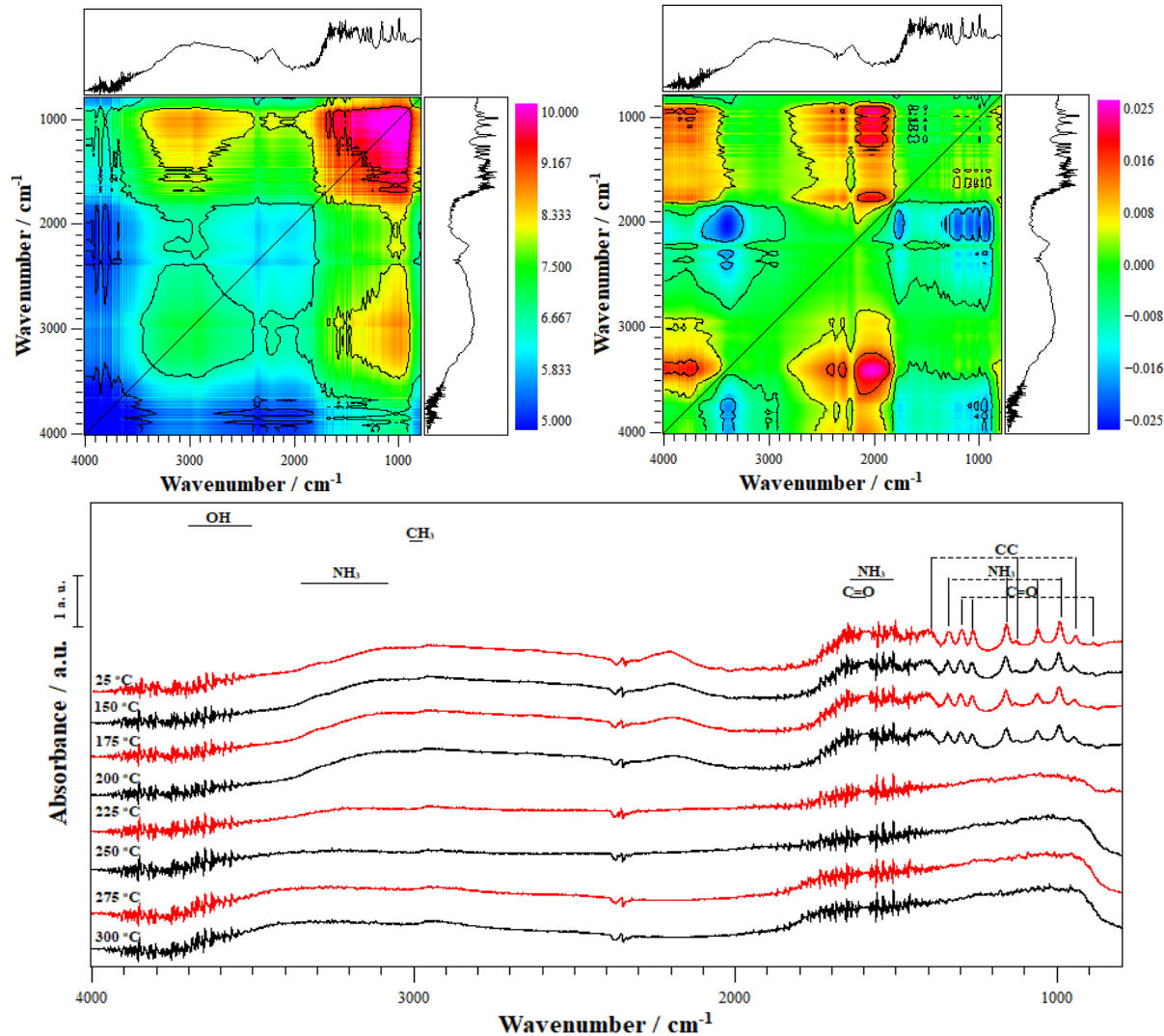


Figure A7. Alanine/ Al_2O_3 synchronous 2D-COS spectra (top-left), asynchronous 2D-COS spectra (top-right) and FTIR spectra at different temperatures (bottom)

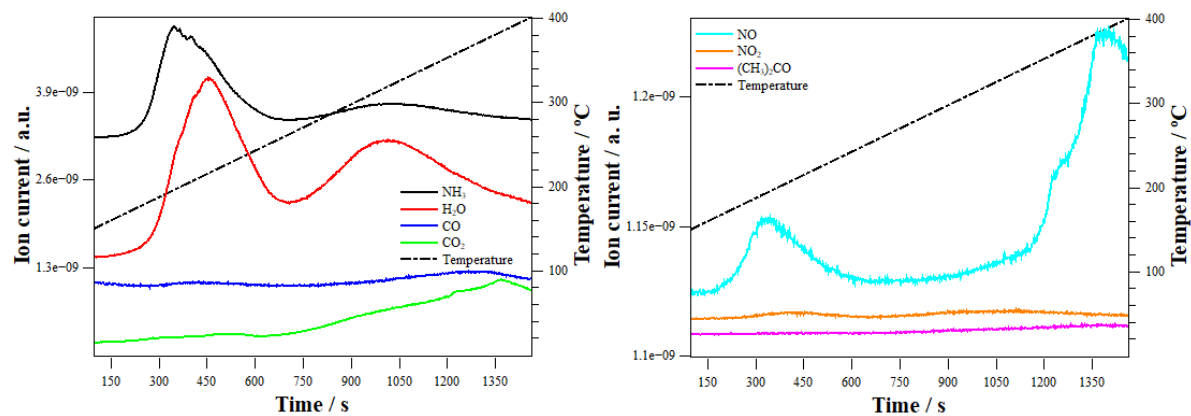


Figure A8. Alanine/ Al_2O_3 oxidation products mass spectra: NH_3 , H_2O , CO , CO_2 (left); NO , NO_2 , $(\text{CH}_3)_2\text{CO}$ (right) ¹¹⁻¹⁷ Uncalibrated MS traces were displaced vertically to facilitate reading.

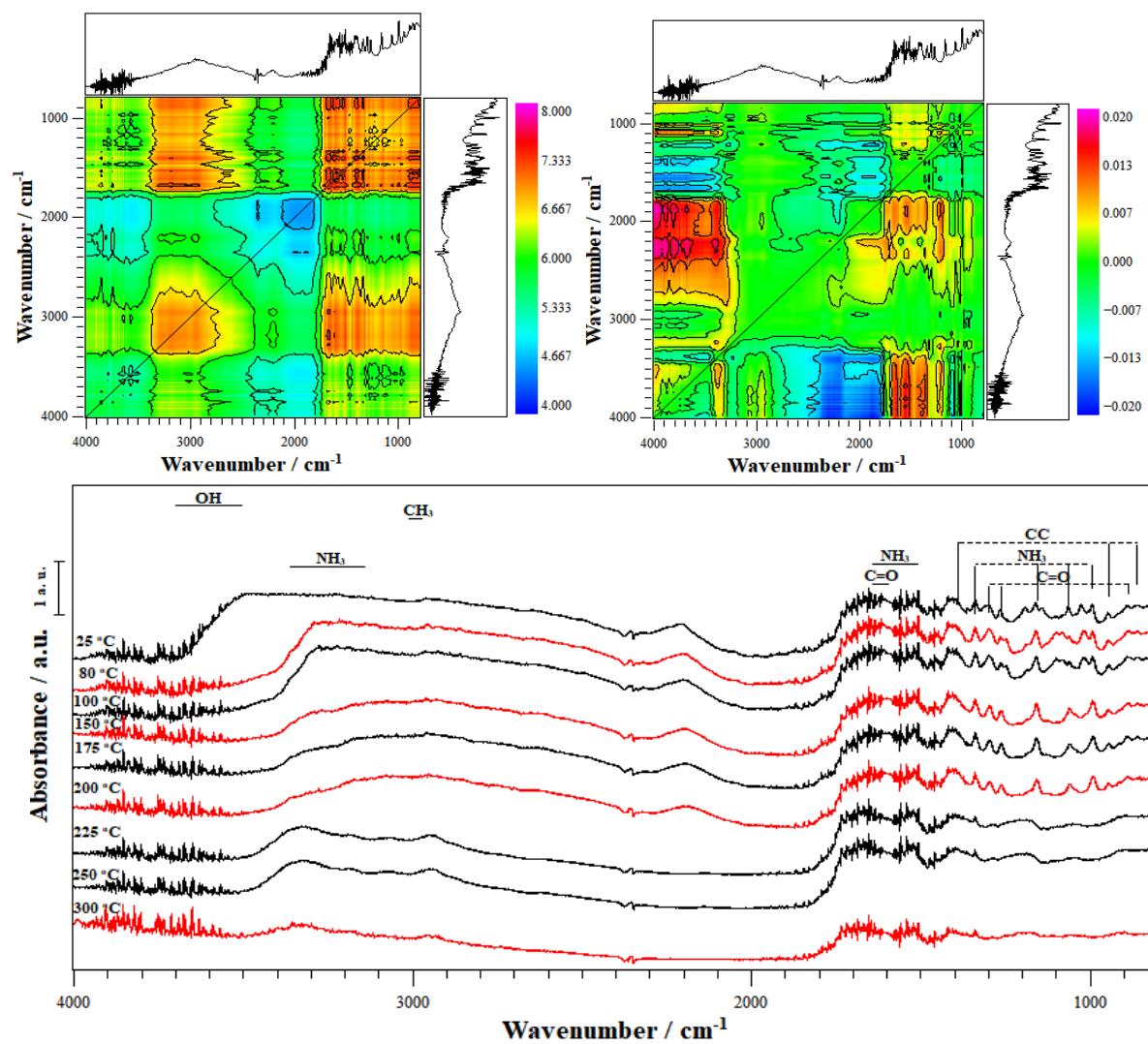


Figure A9. Alanine/Ag/ Al_2O_3 synchronous 2D-COS spectra (top-left), asynchronous 2D-COS spectra (top-right) and FTIR spectra at different temperatures (bottom)

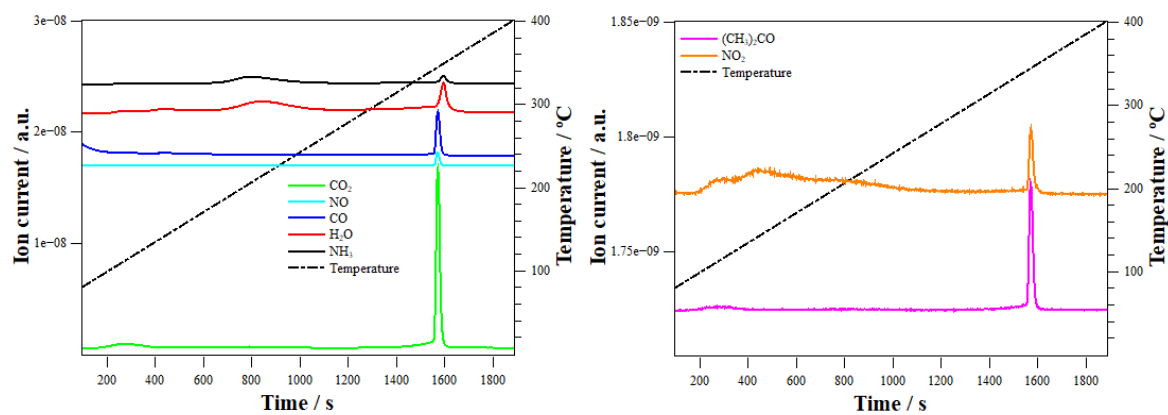


Figure A10. Alanine/Ag/Al₂O₃ oxidation products mass spectra: NH₃, H₂O, CO, NO, CO₂ (left); NO₂, (CH₃)₂CO (right) ¹¹⁻¹⁷ Uncalibrated MS traces were displaced vertically to facilitate reading.

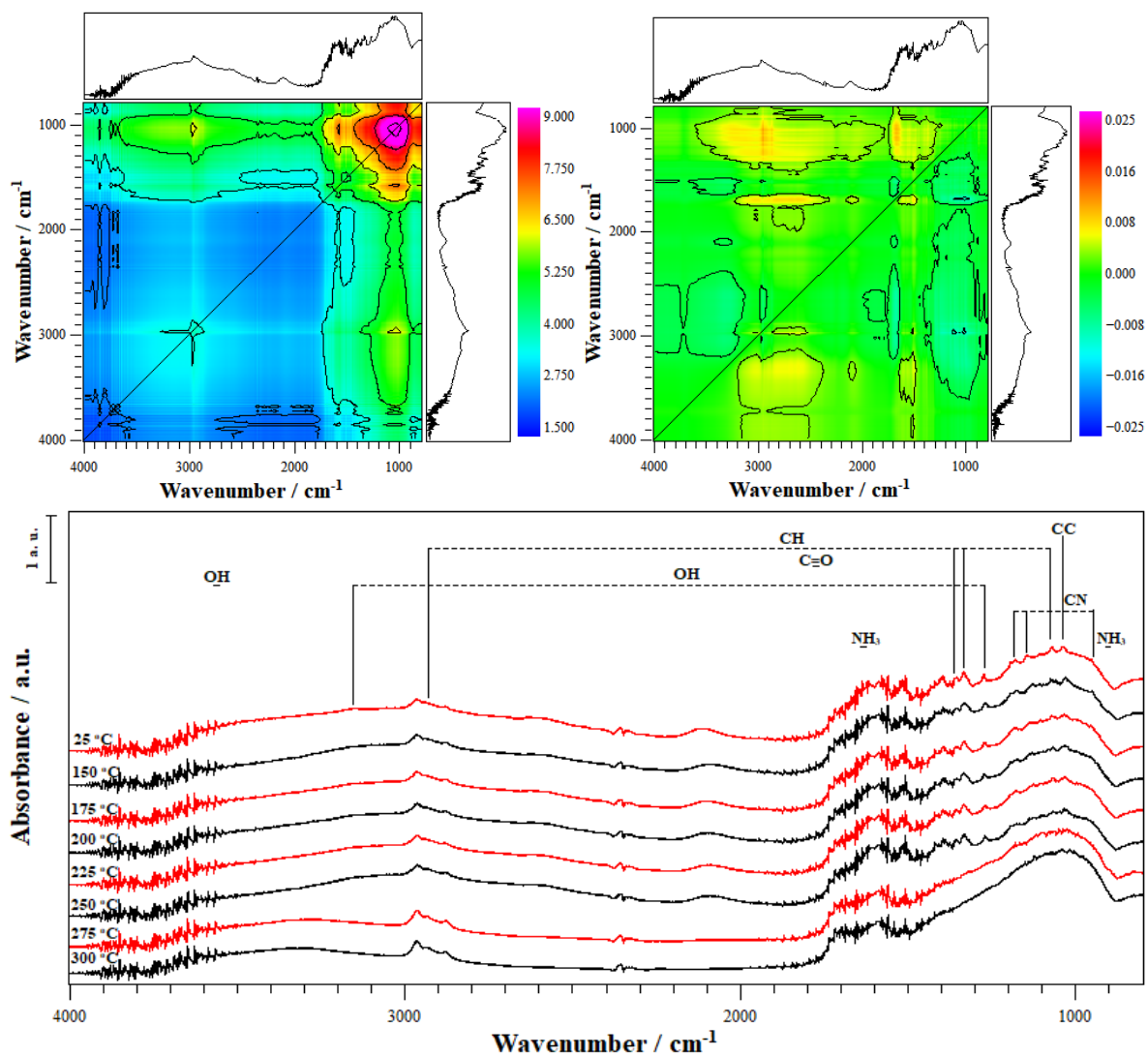


Figure A11. Valine/ Al_2O_3 synchronous 2D-COS spectra (top-left), asynchronous 2D-COS spectra (top-right) and FTIR spectra at different temperatures (bottom)

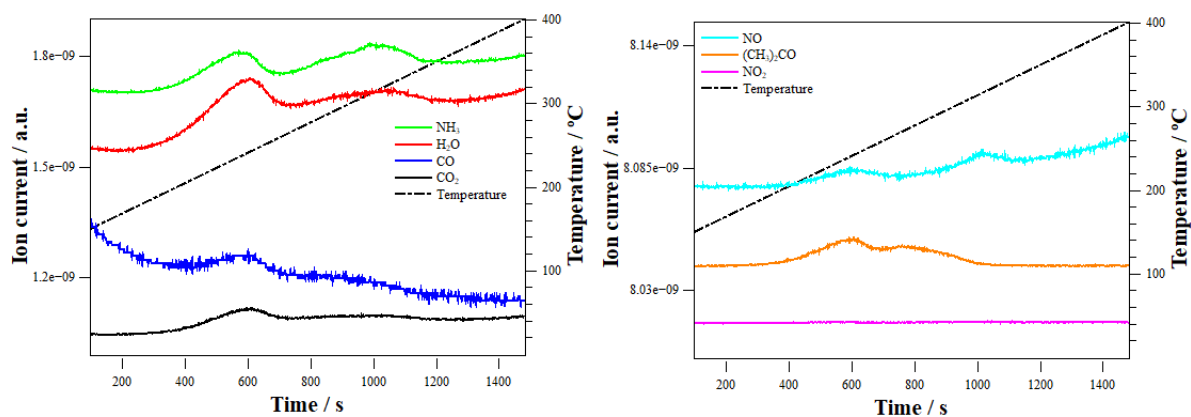


Figure A12. Valine/ Al_2O_3 oxidation products mass spectra: NH_3 , H_2O , CO , CO_2 (left); NO , $(\text{CH}_3)_2\text{CO}$, NO_2 (right) ¹¹⁻¹⁷ Uncalibrated MS traces were displaced vertically to facilitate reading.

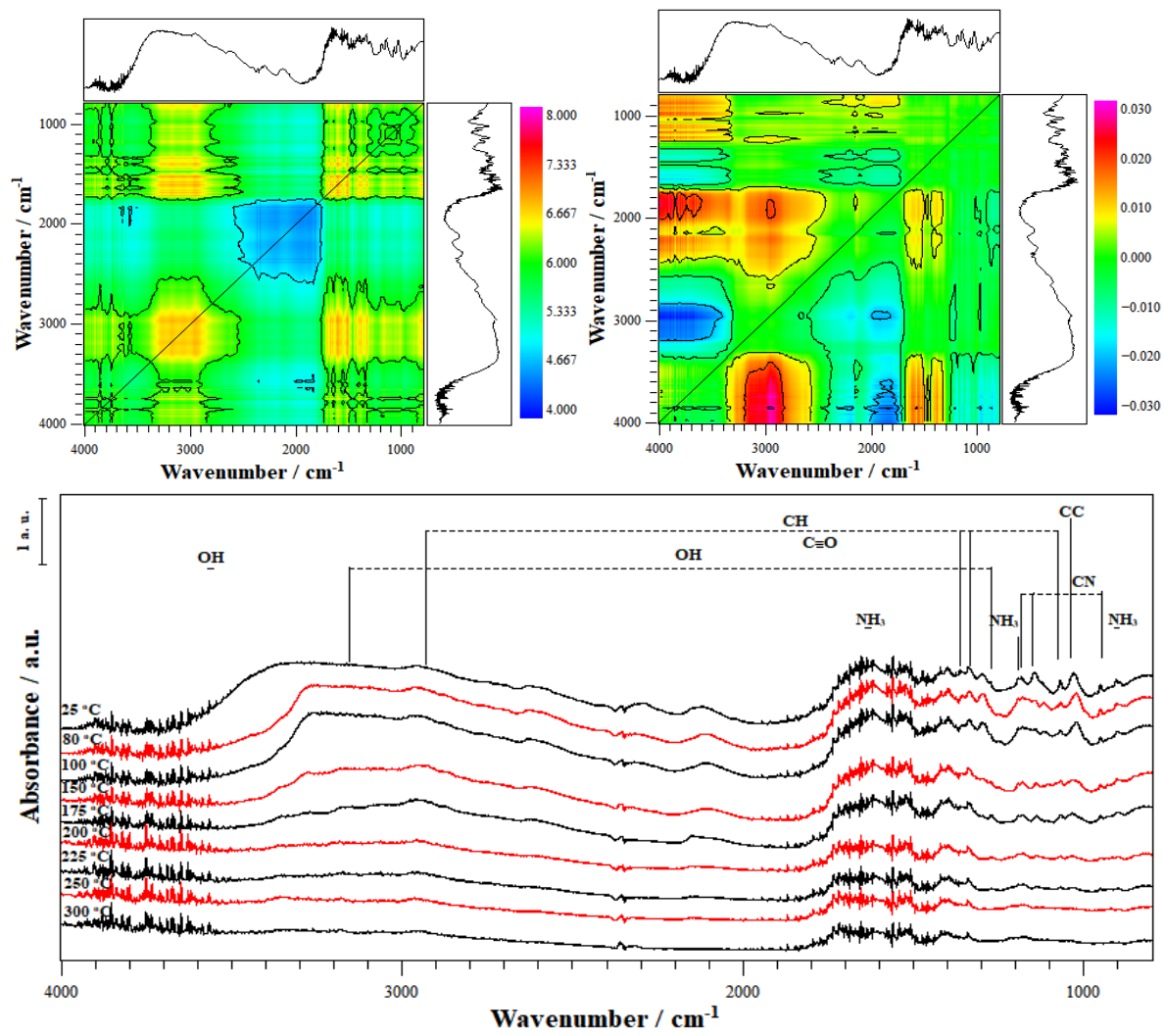


Figure A13. Valine/Ag/Al₂O₃ synchronous 2D-COS spectra (top-left), asynchronous 2D-COS spectra (top-right) and FTIR spectra at different temperatures (bottom)

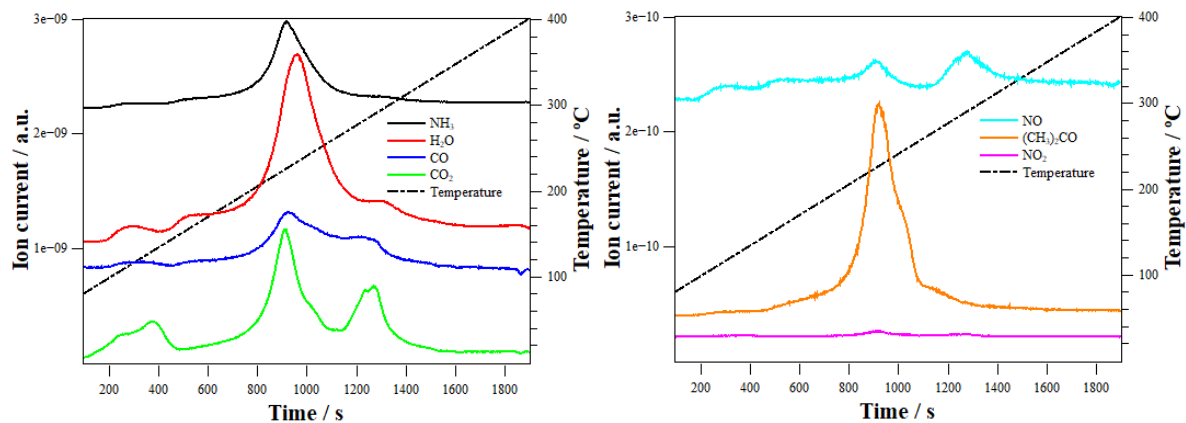


Figure A14. Valine/Ag/Al₂O₃ oxidation products mass spectra: NH₃, H₂O, CO, CO₂ (left); NO, (CH₃)₂CO, NO₂ (right) ¹¹⁻¹⁷ Uncalibrated MS traces were displaced vertically to facilitate reading.

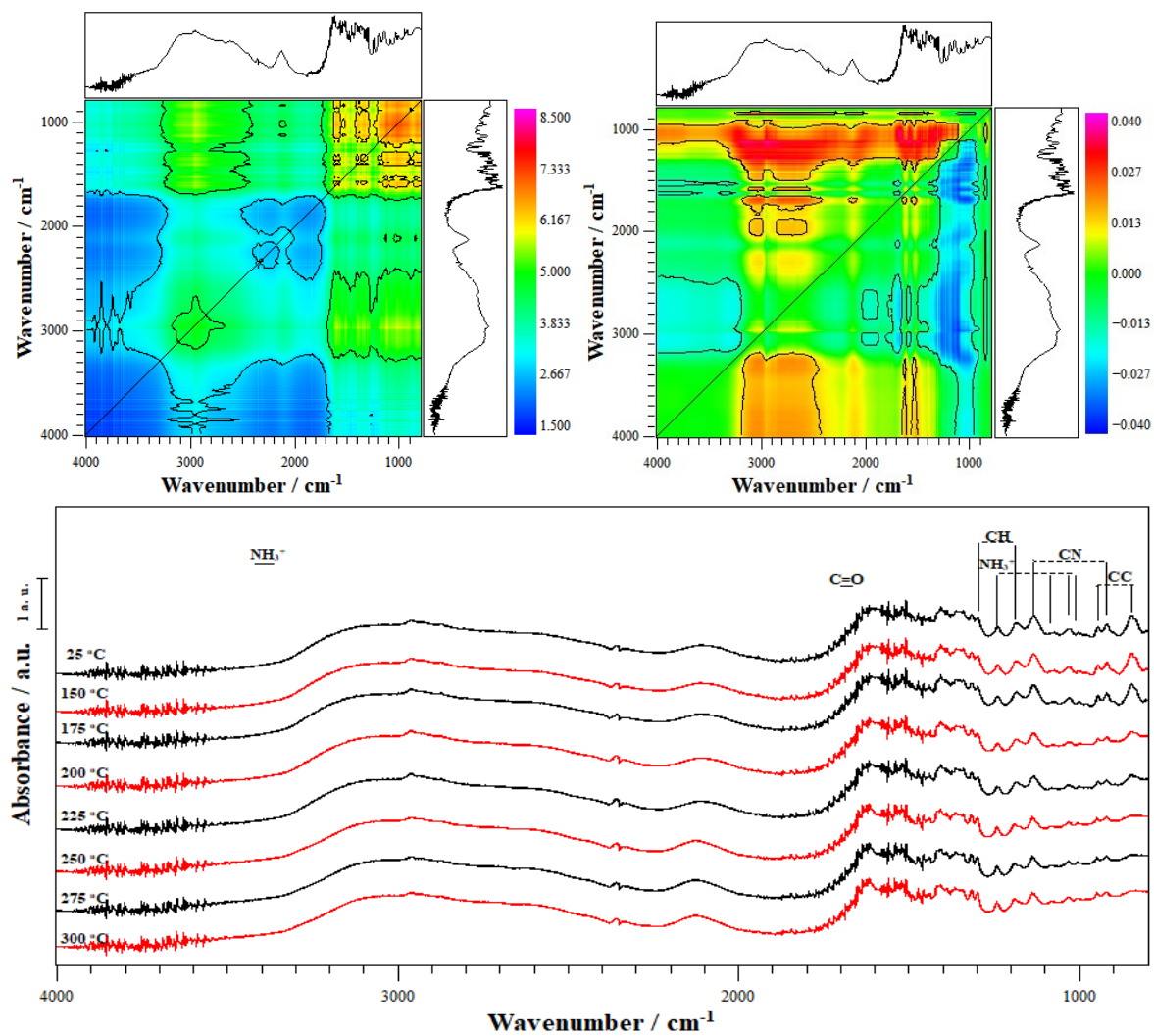


Figure A15. Leucine/ Al_2O_3 synchronous 2D-COS spectra (top-left), asynchronous 2D-COS spectra (top-right) and FTIR spectra at different temperatures (bottom)

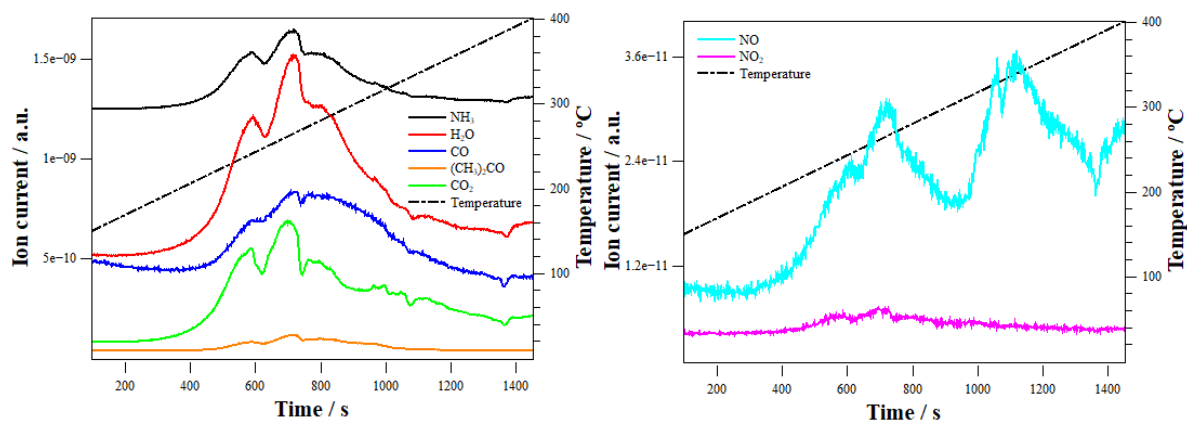


Figure A16. Leucine/ Al_2O_3 oxidation products mass spectra: NH_3 , H_2O , CO , $(\text{CH}_3)_2\text{CO}$, CO_2 (left); NO , NO_2 (right) ¹¹⁻¹⁷ Uncalibrated MS traces were displaced vertically to facilitate reading.

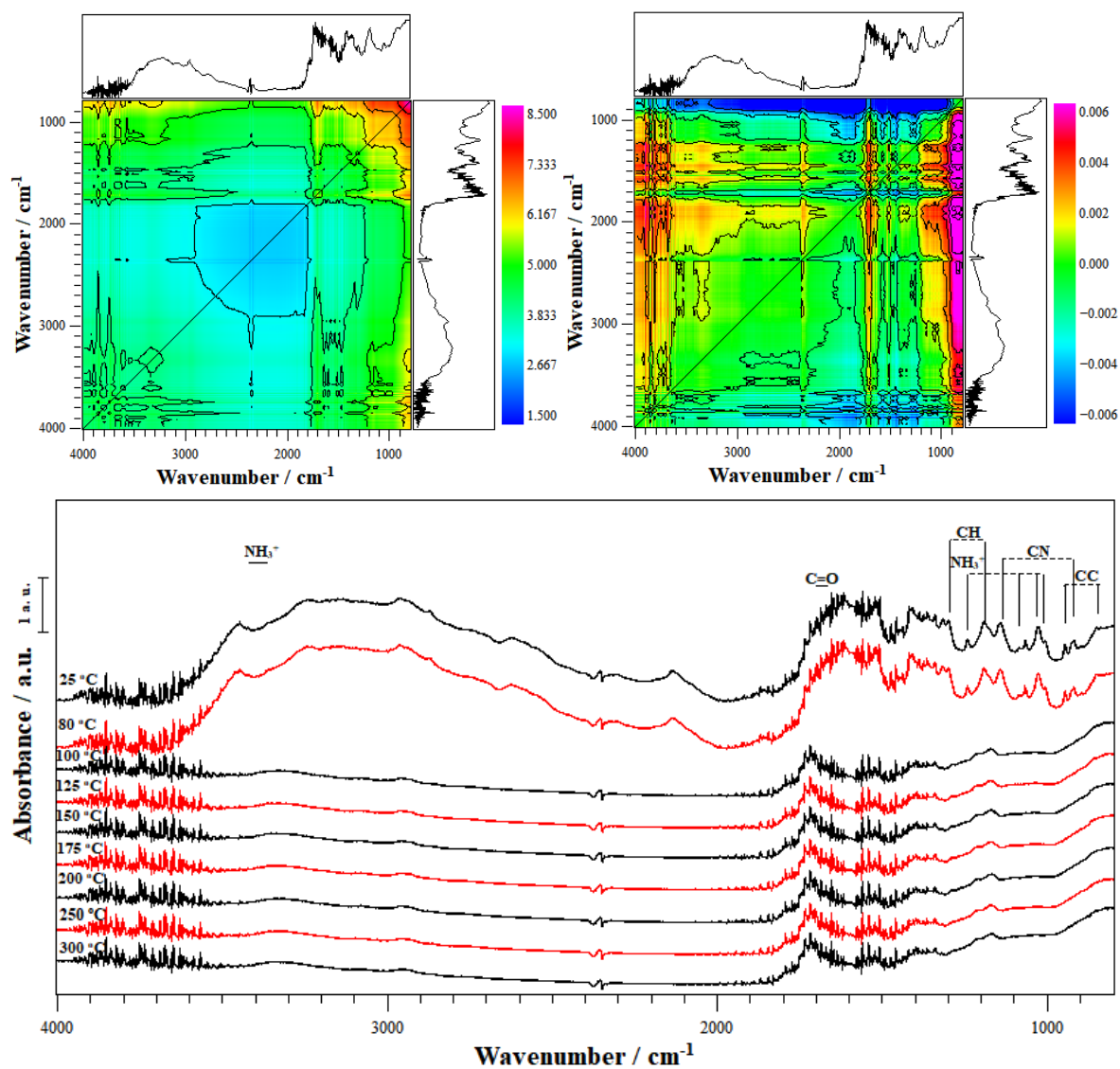


Figure A17. Leucine/Ag/Al₂O₃ synchronous 2D-COS spectra (top-left), asynchronous 2D-COS spectra (top-right) and FTIR spectra at different temperatures (bottom)

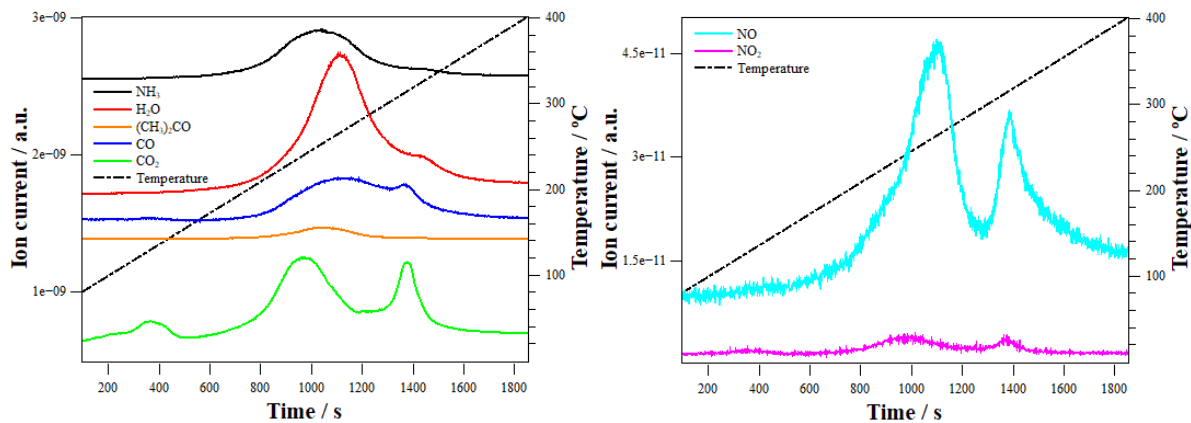


Figure A18. Leucine/Ag/Al₂O₃ oxidation products mass spectra: NH₃, H₂O, CO, (CH₃)₂CO, CO₂ (left); NO, NO₂ (right)¹¹⁻¹⁷ Uncalibrated MS traces were displaced vertically to facilitate reading.

7. Example for How to Analyze 2D-COS Spectra

As an example, here we look at the synchronous and asynchronous plots of glycine/ α - Al_2O_3 analyzed for the DRIFTS collected during a temperature programmed oxidation (TPO) experiment which is discussed in **Chapter 4**.

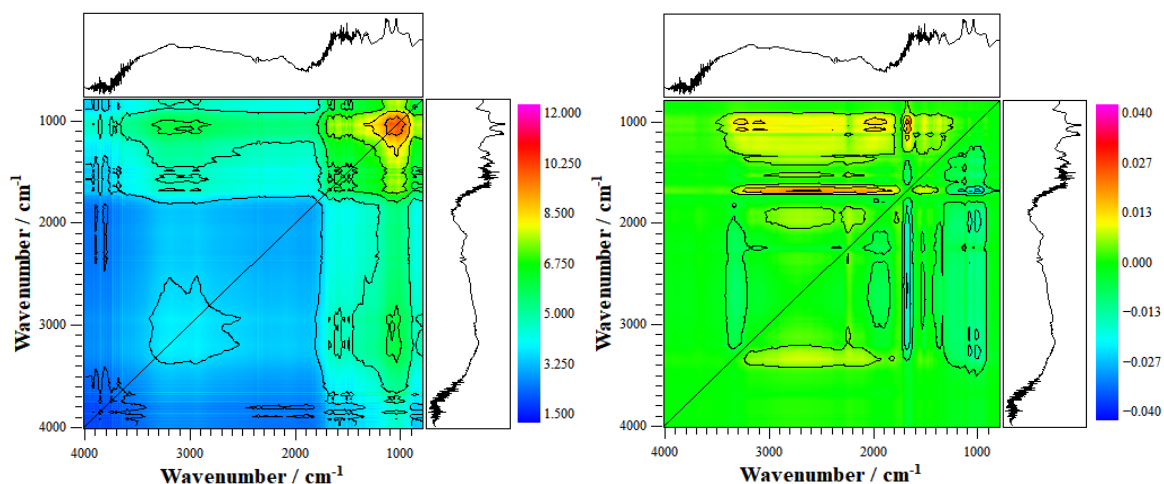


Figure A19. Glycine/ α - Al_2O_3 synchronous (left) and asynchronous (right) 2D-COS spectra

As discussed in **Chapter 1**, the synchronous plot gives us information about changes that take place at the same time (in-sync). From **Figure A19**, the first thing we observe is that the intensity of the spectra (color bars on the right side of the async plot) is positive across the entirety of the plot. This means that the changes taking place during the collection of data are in the same direction, implying that the correlated functional groups (corresponding to the wavenumbers which are the x and y coordinates of a feature on the plot) are both either increasing or decreasing together. This makes sense because we know that only glycine is being decomposed during this time, leading to a constantly decreasing signal for the functional groups disappearing (as can be seen from the infrared spectra shown in **Chapter 4**). Consider, say, the point ($x = 890 \text{ cm}^{-1}$; $y = 1030 \text{ cm}^{-1}$) in the synchronous plot. From the peak assignments for glycine, we know that these are assigned to the CC and CN group contributions in glycine, respectively. The positive feature at ($890, 1030 \text{ cm}^{-1}$) implies that CC and CN are changing at the

same time (both are decreasing as we know decomposition is taking place).

Now, coming to the asynchronous plot; the asynchronous plot gives information on the changes taking place with a time lag. Therefore, we can interpret which functional group is changing (in our case, decreasing) ahead of another functional group, that is, “lagging”. This allows us the order in which a feature such as that assigned to functional groups disappear. From this, it may be possible (among other things as in the present case) to predict which products may form first as a result of the functional group reactivity. Looking at the asynchronous plot presented in **Figure A19**, and considering a wavenumber pair at ($x = 1590 \text{ cm}^{-1}$; $y = 3160 \text{ cm}^{-1}$) we see a negative value of correlation; this implies that the functional group that corresponds to the x coordinate wavenumber (i.e., 1590 cm^{-1}) lags the functional group represented by the y coordinate wavenumber (3160 cm^{-1}). Thus, this would mean that the change in CO lags the change in NH_2 . Therefore, we can say that the NH_2 functional group reacts before the CO group, which, as a result, substantiates the prediction that NH_3 (from the ammine group) would evolve before CO_2 (from the carbonyl group). To get a clearer picture of the correlation values (i.e., color coding) in the asynchronous spectra and its interpretation, **Figure A20** shows the corresponding values of the correlation for $y = 3160 \text{ cm}^{-1}$.

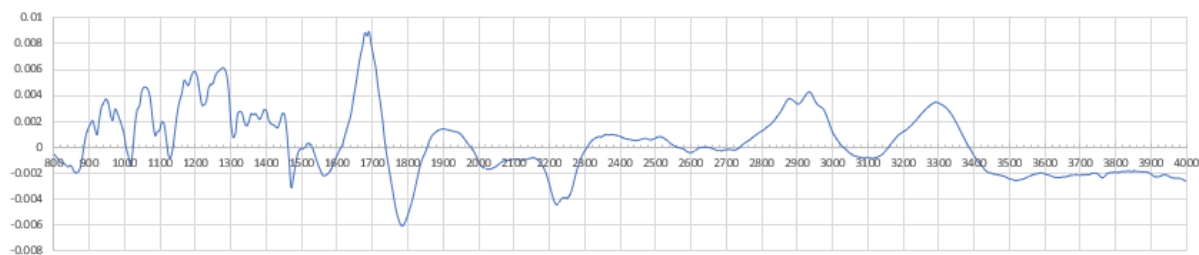


Figure A20. Correlation values of the asynchronous spectra for the wavenumber 3160 cm^{-1}

This figure is a representation of the third dimension (the correlation intensity) in the asynchronous plot focused on the wavenumber 3160 cm^{-1} and which is shown visually as a

color-coded contour plot. From **Figure A20**, we see that the curve is below zero (negative intensity) at 1590 cm^{-1} , confirming that CO lags NH_2 .

8. References

1. Chowdhry, B. Z.; Dines, T. J.; Jabeen, S.; Withnall, R., Vibrational Spectra of α -Amino Acids in the Zwitterionic State in Aqueous Solution and the Solid State: DFT Calculations and the Influence of Hydrogen Bonding. *The Journal of Physical Chemistry A* **2008**, *112* (41), 10333-10347.
2. Morterra, C.; Ghiotti, G.; Garrone, E.; Boccuzzi, F., Infrared spectroscopic characterization of the α -alumina surface. *Journal of the Chemical Society, Faraday Transactions 1: Physical Chemistry in Condensed Phases* **1976**, *72*, 2722-2734.
3. Stepanian, S. G.; Reva, I. D.; Radchenko, E. D.; Adamowicz, L., Combined Matrix-Isolation Infrared and Theoretical DFT and ab Initio Study of the Nonionized Valine Conformers. *The Journal of Physical Chemistry A* **1999**, *103* (22), 4404-4412.
4. Groșan, C. B.; ALMĂȘAN, V., Structure and vibrational spectrum of l-leucine: A dft-pcm investigation. *Chemia* **2011**, 199.
5. Schaberg, A.; Wroblowski, R.; Goertz, R. In *Comparative study of the thermal decomposition behaviour of different amino acids and peptides*, Journal of Physics: Conference Series, IOP Publishing: 2018; p 032013.
6. Yablokov, V. Y.; Smel'tsova, I.; Zelyaev, I.; Mitrofanova, S., Studies of the rates of thermal decomposition of glycine, alanine, and serine. *Russian Journal of General Chemistry* **2009**, *79* (8), 1704-1706.

7. Weiss, I. M.; Muth, C.; Drumm, R.; Kirchner, H. O. K., Thermal decomposition of the amino acids glycine, cysteine, aspartic acid, asparagine, glutamic acid, glutamine, arginine and histidine. *Bmc Biophysics* **2018**, *11*.
8. Lien, Y.; Nawar, W., Thermal decomposition of some amino acids. Alanine and β -Alanine. *Journal of Food Science* **1974**, *39* (5), 914-916.
9. SAMANMULYA, T.; INOUE, S.; INOUE, T.; KAWAI, Y.; KUBOTA, H.; MUNETSUNA, H.; NOGUCHI, T.; MATSUMURA, Y., Gasification characteristics of amino acids in supercritical water. *Journal of the Japan Institute of Energy* **2014**, *93* (9), 936-943.
10. Lien, Y.; Nawar, W., Thermal decomposition of some amino acids. Valine, leucine and Isoleucine. *Journal of Food Science* **1974**, *39* (5), 911-913.
11. NH₃ mass spectrometry.
<https://webbook.nist.gov/cgi/cbook.cgi?ID=C7664417&Units=SI&Mask=200#Mass-Spec>
(accessed July 25, 2022).
12. H₂O mass spectrometry.
<https://webbook.nist.gov/cgi/cbook.cgi?ID=C7732185&Units=SI&Mask=200#Mass-Spec>
(accessed July 25, 2022).
13. CO₂ mass spectrometry.
<https://webbook.nist.gov/cgi/cbook.cgi?ID=C124389&Units=SI&Mask=200#Mass-Spec>
(accessed July 25, 2022).
14. NO mass spectrometry.
<https://webbook.nist.gov/cgi/cbook.cgi?ID=C10102439&Units=SI&Mask=200#Mass-Spec>
(accessed July 27, 2022).

15. NO₂ mass spectrometry.

<https://webbook.nist.gov/cgi/cbook.cgi?ID=C10102440&Units=SI&Mask=200#Mass-Spec>

(accessed July 27, 2022).

16. C₃H₆O mass spectrometry.

<https://webbook.nist.gov/cgi/cbook.cgi?ID=C67641&Units=SI&Mask=200#Mass-Spec>

(accessed July 27, 2022).

17. CO mass spectrometry.

<https://webbook.nist.gov/cgi/cbook.cgi?ID=C630080&Units=SI&Mask=200#Mass-Spec>

(accessed July 27, 2022).